MECHANICAL BEHAVIORS OF BIOMATERIALS OVER A WIDE RANGE OF LOADING RATES

by

Xuedong Zhai

A Dissertation

Submitted to the Faculty of Purdue University

In Partial Fulfillment of the Requirements for the degree of

Doctor of Philosophy

School of Aeronautics & Astronautics

West Lafayette, Indiana

December 2019

THE PURDUE UNIVERSITY GRADUATE SCHOOL
STATEMENT OF COMMITTEE APPROVAL

Dr. Weinong W. Chen
School of Aeronautics and Astronautics
Dr. Eric A. Nauman
School of Mechanical Engineering
Dr. James F. Doyle
School of Aeronautics and Astronautics
Dr. Vikas Tomar
School of Aeronautics and Astronautics

Approved by:

Dr. Gregory Blaisdell
Head of the Graduate Program

For my dear mother.

ACKNOWLEDGMENTS

I would like to express my deep gratitude to Professor Weinong W. Chen, my advisor, for bringing me into the subject of this dissertation and supporting me throughout my PhD studies at Purdue University. His patient guidance, useful critiques and meticulous strict attitude towards research always direct me to the right path to be a qualified graduate student. Every time I lost my heart, his enthusiastic inspiration would help me to regain confidence. I am so honored and lucky to have this chance to be his student and learn from such a great researcher. I would also like to express my very great appreciation to Professor Eric A. Nauman for his assistance and advice on specimen preparation, experiments performance and results analysis. Whenever I need help, he will squeeze some time from his fully occupied schedule to offer me the help with best he can. He is a professor so capable and so willing to pay attention to students. My grateful thanks are also extended to Professor James F. Doyle and Vikas Tomar for taking part in my committee and spending their valuable time in offering me helpful advice on my research works.

I would also like to thank Dr. Waterloo Tsutsui, all my laboratory colleagues and fellow graduate students for their great advices and professional helps in running the experiments and solving various research problems. I also wish to express my appreciations to those great people whoever helped me, no matter slightly or greatly, it is important to me and thank you so much.

Finally, I wish to thank my parents for their supports and encouragements throughout my entire academic life as a graduate student.

TABLE OF CONTENTS

LIST OF TABLES

LIST OF FIGURES

ABSTRACT

Author: Zhai, Xuedong. PhD
Institution: Purdue University
Degree Received: December 2019
Title: Mechanical Behaviors of Biomaterials over a Wide Range of Strain Rates
Committee Chair: Weinong Chen

The mechanical behaviors of different kinds of biological tissues, including muscle tissues, cortical bones, cancellous bones and skulls, were studied under various loading conditions to investigate their strain-rate sensitivities and loading-direction dependencies. Specifically, the compressive mechanical behaviors of porcine muscle were studied at quasi-static (<1/s) and intermediate (1/s─10^2/s) strain rates. Both the compressive and tensile mechanical behaviors of human muscle were investigated at quasi-static and intermediate strain rates. The effect of strain-rate and loading-direction on the compressive mechanical behaviors of human frontal skulls, with its entire sandwich structure intact, were also studied at quasi-static, intermediate and high (10^2/s─10^3/s) strain rates. The fracture behaviors of porcine cortical bone and cancellous bone were investigated at both quasi-static (0.01mm/s) and dynamic (~6.1 m/s) loading rates, with the entire failure process visualized, in real-time, using the phase contrast imaging technique. Research effort was also focused on studying the dynamic fracture behaviors, in terms of fracture initiation toughness and crack-growth resistance curve (*R*-curve), of porcine cortical bone in three loading directions: in-plane transverse, out-of-plane transverse and in-plane longitudinal. A hydraulic material testing system (MTS) was used to load all the biological tissues at quasi-static and intermediate loading rates. Experiments at high loading rates were performed on regular or modified Kolsky bars. Tomography of bone specimens was also performed to help understand their microstructures and obtain the basic material properties before mechanical characterizations. Experimental results found that both porcine muscle and human muscle exhibited non-linear and strain-rate dependent mechanical behaviors in the range from quasi-static (10^{-2}/s─1/s) to intermediate (1/s─10^2/s) loading rates. The porcine muscle showed no significant difference in the stress-strain curve between the along-fiber and transverse-to-fiber orientation, while it was found the human muscle was stiffer and stronger along fiber direction in tension than transverse-to fiber direction in compression. The human frontal skulls exhibited a highly loading-direction dependent

mechanical behavior: higher ultimate strength, with an increasing ratio of 2, and higher elastic modulus, with an increasing ratio of 3, were found in tangential loading direction when compared with those in the radial direction. A transition from quasi-ductile to brittle compressive mechanical behaviors of human frontal skulls was also observed as loading rate increased from quasi-static to dynamic, as the elastic modulus was increased by factors of 4 and 2.5 in the radial and tangential loading directions, respectively. Experimental results also suggested that the strength in the radial direction was mainly depended on the diploë porosity while the diploë layer ratio played the predominant role in the tangential direction. For the fracture behaviors of bones, straight-through crack paths were observed in both the in-plane longitudinal cortical bone specimens and cancellous bone specimens, while the cracks were highly tortuous in the in-plane transverse cortical bone specimens. Although the extent of toughening mechanisms at dynamic loading rate was comparatively diminished, crack deflections and twists at osteon cement lines were still observed in the transversely oriented cortical bone specimens at not only quasi-static loading rate but also dynamic loading rate. The locations of fracture initiations were found statistical independent on the bone type, while the propagation direction of incipient crack was significantly dependent on the loading direction in cortical bone and largely varied among different types of bones (cortical bone and cancellous bone). In addition, the crack propagation velocities were dependent on crack extension over the entire crack path for all the three loading directions while the initial velocity for in-plane direction was lower than the other two directions. Both the cortical bone and cancellous bone exhibited higher fracture initiation toughness and steeper *R*-curves at the quasi-static loading rate than the dynamic loading rate. For cortical bone at a dynamic loading rate (5.4 m/s), the *R*-curves were steepest, and the crack surfaces were most tortuous in the in-plane transverse direction while highly smooth crack paths and slowly growing *R*-curves were found in the in-plane longitudinal direction, suggesting an overall transition from brittle to ductile-like fracture behaviors as the osteon orientation varies from in-plane longitudinal to out-of-plane transverse, and to in-plane transverse eventually.

CHAPTER 1. INTRODUCTION

1.1 Biological tissues

In biological systems, same type of tissues groups together to form into structural units ─ organs to serve a common function. There are mainly four basic biological tissues in animals: connective tissue, muscular tissue, nervous tissue and epithelial tissue. The manifestation and composition of these tissues mainly depend on their functions and hence can differ significantly from each other. For example, due to their largely varied biological functions, the main compositions of human skeletal muscle are approximately 75% of water, 15% of protein and 3% of lipids. While bone, a typical type of connective tissues, mainly consists of organic collagen component (30%) and inorganic mineralized component in the form of aligned rod-shaped crystals (70%). With these different compositions, the mechanical properties of muscle tissue and bone tissue could be strongly different from each other: the muscle is soft and highly ductile while the bone is a rigid and more brittle tissue.

1.1.1 Muscle

The muscle, as a soft and active contractile tissue, is mainly formed by muscle cells. It makes up about 40 percent of human body weight and thus plays a significant role in dissipating impact energy when the body is subjected to high-rate loading. The muscular tissue is further categorized into three types: skeletal, cardiac and smooth muscles. Skeletal muscle, as the largest muscle group in most mammals, is attached to bone by tendon and primarily responsible for skeletal movements, such as changing posture as well as locomotion, and therefore is expected to take additional high-rate loadings during dynamic events. As stated above, approximately 75% weight of human skeletal muscle is water, suggesting that the human muscle is likely viscoelastic, i.e., its mechanical properties are dependent on the loading rate significantly. In addition, bundles of aligned protein filaments of actin and myosin joined together into myofibril, which in turn forms the directional orientated muscle fibers as shown in Fig. 1.1. Therefore, it is also expected that the mechanical behaviors of muscle tissue are highly loading-direction sensitive.

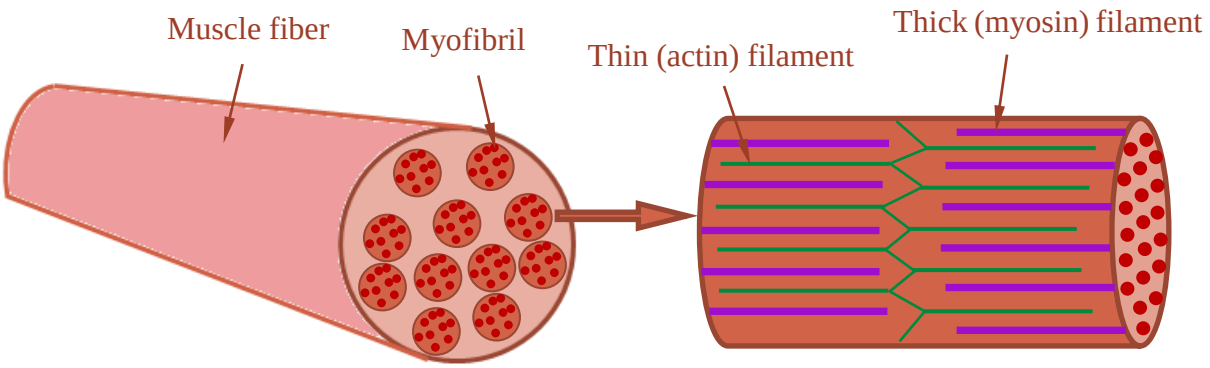

Figure 1.1 A schematic for the microstructures of skeletal muscle fiber

1.1.2 Bone

Connective tissues are mainly fibrous tissues and primarily made up of cells separated by non-living materials called extracellular matrix (ECM). Bone, as a typical connective tissue, is a highly rigid yet lightweight organ and responsible for producing blood cells, supporting the entire body and enabling mobility together with protecting the inner soft tissues from exotic insults. Bone tissue further occurs into two types: as a dense solid tissue that forms the outer layer called cortical bone and an open-cell porous internal structure called cancellous bone, as illustrated in Fig. 1.2. The cortical bone is a highly complex architecture that builds hierarchically into multiple scales, ranging from nanoscopic to macroscopic levels [1-4]. The basic molecular building elements of cortical bone exist at the nanoscale level: plate-shaped mineral carbonated hydroxyapatite nanoparticles and collagenous protein molecules [1, 2], which together constitute the mineralized collagen fibrils, with the collagenous protein molecules, on its own, developing an organic matrix for the mineral crystals at the scales of hundreds of nanometers [1]. Collagen fibrils in turn are bundled together to form larger fibers typically a micrometer in diameter. Sheets of aligned fibers form into micrometers wide lamellar structures, and three to eight layers of lamellae join together into a cylindrical structure that is several hundred micrometers in size, known as osteon or Haversian system, which is regarded as the basic unit in cortical bone [3]. Volkmann's canals vertical to the osteons connect the Haversian canals together. The osteons are aligned parallel to each other and longitudinal to the axis of long bones, forming a typical anisotropic architecture in bone [2]. This anisotropy built inherently in its microstructural configuration results in the loading-direction dependency found in almost all of its fundamental mechanical properties [4].

Cancellous bone, or trabecular bone, is a less dense tissue located inside of bones and at the ends of long bones. It develops a lattice-like network structure and hence possesses a higher surface-area-to-volume ratio than cortical bone. It is reported the trabecular bone accounts for 20% of total bone mass yet possesses nearly ten times the surface area of cortical bone [5]. A recent study showed that the trabeculae were aligned towards the mechanical load distribution that the bone experienced during its growth and this alignment in vertebral was well studied previously [6]. Cancellous bone is also highly vascular and mostly contains red bone marrow. This porous structure together with its high volume of liquids grand the trabecular bone superiority in flexibility and impact absorption. Consequently, it is expected that the mechanical behaviors of both cortical and trabecular bone tissues strongly depend on both the loading direction and loading rate.

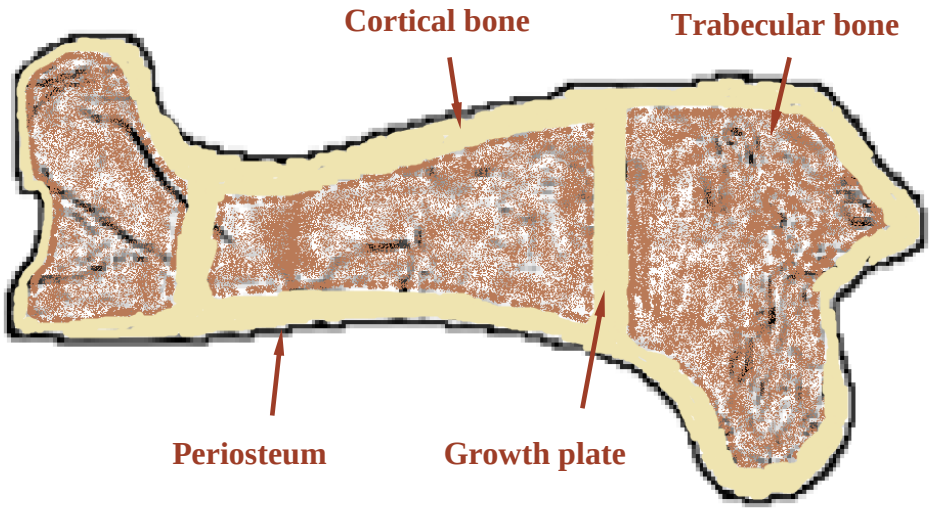

Figure 1.2 The distribution of cortical bone and trabecular bone in long bones

1.2 Mechanical behaviors of biological tissues

Biological tissues potentially undergo various loading conditions over a wide range of strain rates: quasi-static, intermediate and high strain rates. For example, studies on the *in-vivo* loading conditions in bone suggested that the loading rate was approximate ~0.007-0.02/s during walking or running [7-9], while it could be as high as ~25/s (impact speed: 7m/s) for impact events [10]. Therefore, it is with great importance to investigate the mechanical behaviors of biological tissues under both quasi-static and dynamic loading conditions. The mechanical behaviors of biological

tissues are vastly studied previously ang they are believed to be dependent on their biological functions, which in turn determined by its microstructures significantly. The reported properties of both muscle and bone tissues are introduced separately below.

1.2.1 Muscle

The pioneering studies on quasi-static mechanical behaviors of soft biological tissues started as early as decades ago [11, 12]. Later, the compressive mechanical behaviors of passive rat skeletal muscle were studied at a quasi-static strain rate and it was found the stress-strain curves were non-linear and viscoelastic [13]. More interestingly, cyclic tensile experiments on passive rabbit muscle at various rates at engineering strain up to 40% showed that the energy dissipated by the muscle was independent of strain rates [14]. Experiments on rat tibia anterior muscle found that the tendon compliance did not alter the active force generated by muscle over a normal joint range of motion but exerted a significant influence at the extremes of joint motion [15]. Fresh and aged bovine muscle, porcine muscle and ovine muscle were studied at different muscle fiber orientations and loading rates in uniaxial compression [16-18]. Results showed that the passive mechanical behaviors of all those muscle tissues were dependent on strain rate as well as fiber orientation [16-18]. It was also found that the difference between fresh and aged muscle was significant and the effect of postmortem time in the aged passive muscle was only significant within a specific range of time [16-18]. In addition to experimental studies, numerical methods incorporating the active and passive response of muscle tissues were also developed and it was concluded that the quasi-static mechanical responses of skeletal muscle were non-linear and the difference between the active and passive muscle was significant, which agreed well with those experimental results [19, 20].

Research effort was also invested to experimentally characterize the muscle's mechanical properties in both compression and tension at a high strain rate [21]. Song *et al*. studied the fresh porcine muscle in compression and found that both the strain-rate and loading direction dependencies were apparent at high strain-rate within the scope of Kolsky bar [21]. It was found that the effect of strain-rate was more significant in the loading direction perpendicular to fiber direction than parallel to fiber direction [21]. High strain-rate tensile loading was also applied using Kolsky tension bars on fresh porcine muscle [22]. Similar to that in compression, the tensile stress-strain curves of fresh porcine muscle were also non-linear and strain-rate sensitive [22].

Comparing with that in compression, porcine muscle exhibited less significant loading direction dependency in rate sensitivity under tension loadings, i.e., the difference in the effect of strain rate for the two loading direction cases was less significant in tension than in compression [22]. In addition, Myers studied the effect of strain-rate in the range of 1/s to 25/s on the passive and stimulated compressive mechanical response of rabbit tibialis anterior muscle and concluded that the stimulated muscle was less strain-rate sensitive than the passive muscle [23]. However, the loading-direction dependency in the tensile mechanical behaviors of muscle tissues was quite controversial in the literature, with a stiffer behaviors in transverse-to-fiber direction at small strains were reported for porcine muscle and rabbit muscle [24, 25], while a stiffer response was observed for rabbit muscle along the longitudinal-to-fiber direction [26].

As well studied, skeletal muscle is a composite tissue of major active contractile muscle fibers and other minor tissues, such as blood vessels, nerves and connective tissues (ECM) [19]. Although the ECM is account for a small volume of the entire muscle tissue, it may presumably affect the muscle's biological functions and mechanical properties significantly [19]. For example, ECM in muscle, including the endomysium, perimysium, and epimysium were reported acting as the major loading bearing structures in passive muscle [27, 28]. Studies were conducted to compare the tensile mechanical properties of two groups of muscle tissue: one group with ECM intact and the other one with ECM removed. Experimental results showed that the muscle with ECM removed was less nonlinear elastic and stiffer than the group with ECM intact, indicating that ECM could be highly nonlinearly elastic and its modulus was largely stiffer than muscle fibers [27]. Later, experiments were performed to directly measure the mechanical properties of ECM by removing the muscle fiber while keeping ECM intact from the entire muscle and the results agreed with the properties of ECM estimated indirectly [28].

1.2.2 Cortical bone and trabecular bone

Bone is also a typical composite tissue consisting of collagen and hydroxyapatite. Its mechanical properties are primarily construed by its complex hierarchy architecture [1, 2]. There has been a large body of studies on the mechanical behaviors of bone tissues in literature [29-63], with some focused on the uniaxial tensile, compressive and torsional mechanical properties [29-39] and others concentered on its fracture toughness [40-63].

Studies to characterize the strength and modulus of cortical bone showed that the cortical bone was stronger under shear loading than under tensile loading and no difference in toughness was found between men and women [29]. A gradually decrease in elastic modulus, strength, work to failure and fracture toughness was observed as age increased [40]. This decrease in toughness due to aging was mainly attributed to the alternation that occurred in the microstructure: increased non-enzymatic collagen cross-linking, which suppressed plasticity at the nanoscale dimension, and also an increased osteonal density, which limited the potency of crack-bridging mechanisms at micrometer scales [41]. It was suggested that the increased non-enzymatic collagen resulting in the increased stiffness of the cross-linked collagen required energy to be absorbed by plastic deformation at higher structural levels, such as the process of microcracking, which, as a result, presumably decreased the bone's toughness [41].

As the basic functional unit in bone, osteon plays a vital role in resisting the cracks in bone. The osteons, consisting of highly mineralized collagens, are glued together with organic matrix and the entire structure is hence reinforced. As the crack impinges upon the interface between osteon and matrix (interstitial lamellae), also known as the osteonal cement line, it is likely to be significantly deflected, which increases the driven force for further crack propagation and hence increases the fracture toughness [42]. A recent study on the role of collagen in determining the bone's mechanical properties found that the collagen network also played an important role in the toughness of bone, but had little effect on the stiffness of bone [43]. The effect of microstructural material properties on the mechanical properties of bone at macroscopic levels was also vastly studied in the literature [37, 44, 45]. It was found that the hardness of interstitial lamellae was a function of age significantly and the longitudinal fracture toughness decreased more rapidly than transverse fracture toughness as age increased [44]. The influences of porosity, osteon-density, osteonal area, osteonal lamellar area, osteon size and Haversian canal size on the toughness of cortical bone were also investigated under tension and shear loadings [37]. The results suggested that porosity and osteon density were the primary morphological parameters in influencing the toughness of bone. The cement line fracture toughness, significantly decreased with increasing age, was less effective in energy absorption and hence had a significant effect on the toughness [45].

Cancellous bone, also called trabecular bone or spongy bone, is mostly seen in the internal region of all kinds of bones and at ends of long bones. It is also largely distributed in irregular vertebra and skull bones. The porosity of trabecular bone is largely higher than the cortical bone

and exhibits entirely different mechanical behaviors than cortical bone. As that for cortical bone, there are also abundant studies on the trabecular bone under various loading conditions in literature [46-48]. The tensile and compressive elastic modulus of trabecular bone was measured by either loading the specimen to failure [46] or by non-destructive testing [47], and an elastic modulus of ~871 MPa was reported [46]. No difference between the elastic modulus in tension and compression was observed while the strength, ultimate strain, and work to failure was extremely higher in tension [47]. A study on the material properties of trabecular bone also showed that its strength and modulus were approximately proportional to the cube of the apparent density [48].

As stated above, bone is a composite material and contains some extent of fluids, such as blood. Therefore, it is expected that bone exhibits viscoelastic mechanical behaviors. The effect of loading rate on bone's behaviors was extensively documented in the literature [31-33, 48-59]. In general, a transition from ductility to brittleness was observed in both cortical bone and trabecular bone as the loading rate increased from quasi-static to dynamic [31, 32, 48, 51, 52]. More specifically, the strength, stiffness, elastic modulus increased significantly while fracture toughness and strain at failure decreased as loading rate increased from quasi-static (1×10^{-3}/s) to dynamic (as high as 1×10^{3}/s) [31, 32, 48, 51, 52]. The fracture surfaces in bone under bending loading also tended to become less rough and more cleavage-like at higher rates, showing a typical brittle mechanical behavior [51]. Such reduced toughness was suggested to be due to the differences in the toughening mechanisms between quasi-static and dynamic loading rates [58]. A critical strain-rate range was reported between 1×10^{-4}/s and 1/s, where the ultimate strain and energy absorption increased first while further increase in strain-rate resulted in decreases in those mechanical properties [52, 59]. The strain-rate effect on trabecular bone was also apparent and similar trend that it became more brittle as the loading rate increased was also observed [48, 53-57]. For example, the strength increased by a factor of approximately 2-3 when the strain rate increased from 10^{-5}/s to 500/s [53]. Other properties, including the stiffness, ultimate strain and modulus were also strongly affected by the strain rate [48, 54-57]. Besides, other factors, such as a large dose of radiation could also exert a significant effect on the mechanical properties of bone [60-63]. It was studied that a high volume of radiation definitely applied a deleterious effect on bone's mechanical behaviors, resulting in a decrease in its fracture toughness. However, the effect of a lower dose of radiation is still controversy, with an apparent decrease in toughness reported in [60-62] while no significant effect observed in [63].

1.2.3 Skull bone

Skull bones composed of two parts: the facial skeleton and the cranium. A common bone fracture during impact events, such as motorcycle accidents and physical confrontations in sports, is facial bone fracture [64]. However, only spotty studies can be found and the results are largely varied among different studies on the same facial bones [64-68]. For example, it was reported the critical forces to fracture of human nasal bone was 450 to 850 N in [65] while its stiffness was 261 (SD, 217) N/mm in [64]. Such large variations of critical forces and fracture of human nasal bone was also observed in human mandible bone, with a value of 2500 to 3000 N reported in [67] while a value of 5270 (± 930) N reported in [68].

Traumatic skull injury also occurs commonly during blast and impact events, which hence could potentially induce fatal brain injuries. Therefore, it is with great importance to study the mechanical behaviors of cranial bones, and thus to help improve the protective gears and rational therapies [69]. Cranial bone is a complex bony structure that possesses a typical sandwich architecture: with the inner and outer layers (tables) are made of cortical bone while porous trabecular bone, also known as diploë, is distributed in between. With this sandwich configuration, its mechanical behaviors are believed to be both highly loading-direction and loading-rate dependent. The loading-direction dependency of the cranial bones was studied abundantly in the literature, although most of them concentrated at quasi-static loading rates [69-72]. It was shown the cranial bone was a brittle material and its strength and elastic modulus were loading-direction dependent (radial and tangential) in both compression and tension [69-72]. A conclusion was also drawn that human cranium was viscoelastic based on the observation that there was a large amount of recoverable strain in the failed specimen [70]. However, the reported mechanical properties were largely varied in the literature and such variations could be owing to the largely varied porosity and internal arrangement of the diploë [69].

1.3 Research gaps in the literature and the objective of the present dissertation

As can be seen, most of the studies on biological tissues in literature are focused on quasi-static loading rates [11, 12, 37-45, 69-84], where it is comparatively straight forward to load the specimen and collect the data. The main reason can be that most of the testing apparatus used in their study are built solely for experiments at strain rates below 1/s and can hardly be used to load

the specimen at higher rates. Although Kolsky bars are designed for high-rate loading, they are not standard apparatuses, and it acquires a large amount of effort to properly control the testing condition and hence ensure a valid experiment. However, in reality, many loading conditions that result in fatal damages to biological tissues are those involved in dynamic and impact events: such as car collisions and sports accidents. In those situations, soft tissues, such as muscles, and hard tissues, like bones, are potentially subjected to loadings with the strain rate falls in the range of intermediate and high rates [85-88]. For example, a study on the *in vivo* loading conditions in skull bone reported that the loading rate in impact events was 14/s or higher [87]. Even some studies were conducted on muscles at dynamic loading rates, no data fall in the range of intermediate strain rates were available in the literature. Furthermore, investigations on the fracture toughness of bone were mainly restricted to either the transverse loading directions or quasi-static strain rates [38, 39, 42, 45, 73-84], and no real-time observation of the entire fracture process in details, including crack initiation and subsequent propagation [58, 89], was provided. Dynamic experiments on skull bones were either performed solely on the cortical layers of the skulls [90] or on the infant skull bones [91], where the structure was entirely different from the adult human cranial bones.

Therefore, it is important to quantitatively understand the mechanical responses of biological tissues, such as muscle tissues, cortical bones, trabecular bones and the cranial bones (with the whole sandwich structure intact) at intermediate and high strain rates. In this dissertation, we experimentally investigated the uniaxial compressive mechanical properties of fresh porcine muscle at quasi-static and intermediate strain rates in parallel and perpendicular to the fiber direction. The passive human muscle's mechanical behaviors along fiber direction in compression and transverse to fiber direction in tension were also studied at quasi-static and intermediate strain rates. Fracture toughness of both cortical bone and trabecular bone was investigated at a quasi-static and dynamic loading rate. The effect of loading direction on the fracture behaviors of cortical bone in terms of crack-growth resistance curves (R-curves) was also studied at a dynamic loading rate. The entire fracture processes in the bones were also visualized, in real-time, using the high-speed synchrotron X-ray phase contrasting imaging technique. The strain-rate dependencies and loading-direction sensitivities in the mechanical behaviors of human frontal skull bones were quantitatively studied at quasi-static, intermediate and high strain rates. The entire *in-situ* failure processes in the skull bone specimens in the radial and tangential loading directions were also visualized and the failure types in the two loading-direction cases were hence identified.

CHAPTER 2. QUASI-STATIC AND DYNAMIC COMPRESSIVE MECHANICAL RESPONSE OF PORCINE MUSCLE

Adapted from:
X. Zhai, W.W. Chen. Compressive mechanical response of porcine muscle at intermediate (10^0/s-10^2/s) strain rates, Experimental Mechanics. Doi: 10.1007/s11340-018-00456-1. (with permission from Springer)

2.1 Abstract

Compressive stress-strain response of porcine muscle was experimentally determined at intermediate strain rates (10^0/s-10^2/s) in this study. A hydraulically driven materials testing system with a dynamic testing mode was used to perform the compressive experiments on porcine muscle tissue with loading directions parallel and perpendicular to muscle fiber direction. Experiments at quasi-static strain rates were also conducted to investigate the strain-rate effects over a wider range. The experimental results show that, at intermediate strain rates, the porcine muscle's compressive stress-strain responses are non-linear and strain-rate sensitive. The porcine muscle's compressive mechanical response exhibits no significant difference between the two fiber orientation cases at quasi-static and intermediate strain rates. An Ogden model with two material constants was adopted to describe the rate-dependent compressive behavior of the porcine muscle.

2.2 Introduction

Analytical constitutive models and numerical methods are increasingly used for various applications in tissue engineering and biomedical engineering in recent years, such as simulations of the mechanical response of biological tissues and predictions of bio-tissue impairment under different loading conditions. A quantitative understanding of the mechanical behaviors of those biological tissues over a wide range of strain rates is the basis of those models and methods. Comprehensive studies on quasi-static mechanical behavior of biological tissues started decades ago [11, 12]. Unconfined uniaxial in vivo compressive experiments on passive rat skeletal muscle were conducted in order to reveal its nonlinear viscoelastic behavior and the Ogden model was used to fit the experimental data [13]. Cyclic tensile loading and unloading experiments on rabbit muscle at various rates and temperatures with the engineering strain up to 40% were also

performed to show that the energy dissipated by the muscle specimens is independent of strain rates and temperatures [14]. Hawkins and Bey [15] experimentally investigated the effect of tendon compliance on rat tibialis anterior muscle's force-length behavior at quasi-static strain rates and suggested that tendon's compliance does not alter the active force generated by muscle over a normal joint range of motion but has an effect at the extremes of joint motion. van Loocke et al. [16-18] conducted uniaxial compressive experiments on fresh and aged bovine muscle, porcine muscle and ovine muscle tissues for various muscle fiber orientation cases at different compression rates and concluded that those muscles' mechanical behaviors are dependent on strain-rate, fiber orientation and time of test after death. There have been some studies focused on the anisotropic mechanical behaviors of passive skeletal muscle in the literature [24, 26], although different experimental results were reported in those works. Quasi-static (5×10-4/s) tensile experiments were performed on porcine muscle to an engineering strain of 130% or to failure with the fiber direction orientated 0°, 30°, 45°, 60°, 90° to the loading direction. Experimental results suggested that the transverse direction was generally linear and was the stiffest whereas the longitudinal direction was nonlinear and much less stiff [24]. However, similar tensile experiments on rabbit muscle at quasi-static strain rates (5×10-4/s) indicated that its stiffness was significantly higher in the longitudinal direction compared with the transverse direction [26]. Noninvasive testing methods, such as ultrasound-based technique was used to investigate the anisotropic in vivo mechanical properties of muscle tissue [92], despite the inherent disadvantage of those methods that could hardly deform the tissue to large strains with sufficient magnifications. Works performed to understand the morphological characteristics of the architectures in skeletal muscle [19, 93] and their contributions to the mechanical properties of whole muscle tissue [20, 27, 94] are much sparser in the literature. It was found that the titin filaments in muscle fiber played only a minor role in passive stretching load-bearing, while that the connective tissue, or extracellular matrix (ECM), was tremendously stiff and acted as the major load bearing structure [19, 27]. Furthermore, numerical methods incorporated with active and passive response of muscle tissue were also developed to simulate the quasi-static mechanical responses of skeletal muscle and showed a good agreement with the experimental results [19, 20].

Research efforts have also been invested to experimentally study the mechanical response of biological tissues at high strain rates (102/s-5.7×103/s). Characterization of compressive stress-strain responses of various biological tissues, such as porcine muscle [21] and bovine muscle [95]

was achieved at high strain rates using modified Kolsky compression bars. All those muscle tissues exhibit non-linear and strain-rate sensitive compressive mechanical behaviors. More specifically, the strain-rate dependency of porcine muscle is also sensitive to the loading direction and more significant in the direction perpendicular to fiber direction than that parallel to fiber direction [21]. However, experimental evidence of bovine muscle under similar testing conditions showed that, at both quasi-static and high strain rates, there was no statistical difference in its compressive stress-strain behaviors between the parallel and perpendicular fiber orientation cases [95]. Kolsky tension bars were also used by researchers to investigate the tensile and shear responses of various biological soft tissues. The stress-strain response of porcine muscle under dynamic tensile loadings is also non-linear and strain-rate sensitive. The dependency of loading direction on the rate sensitivity of porcine muscle's tensile behavior is less significant than that in its compressive behavior [22].

Many loading conditions on bio-tissues involved in various dynamic situations, such as vehicle collision or sports accidents, fall in the range of intermediate strain rates [85, 86]. Therefore, it is important to quantitatively understand the mechanical response of biological tissues at those strain rates. However, experimental data are very scarce on soft materials [85, 96-98], especially on biological tissues [23, 99] in literature in the range of intermediate strain rates. Myers et al. [23] performed experiments to study the effect of strain rate in the range of 1/s to 25/s on both passive and stimulated compressive mechanical response of rabbit tibialis anterior muscle and found that the stimulated responses were less sensitive to strain rates than the passive responses. Despite these spotty publications on intermediate rate behavior of muscle tissues, research activities in this rate range remain limited. The reason for this data scarcity is that there are still no well-established techniques for the mechanical characterization of soft tissues at intermediate strain rates. Most traditional material testing frames are built to perform experiments at strain rates below 1/s, whereas typical Kolsky bars are designed to conduct dynamic experiments at strain rates above 10^2/s. Although drop-weight towers load specimens at intermediate strain rates, complete stress-strain responses at a constant strain-rate are not obtained directly. In this study, we experimentally investigate the compressive stress-strain response of porcine muscle tissue at intermediate strain rates using a hydraulically driven high-speed material test system.

2.3 Experiments

2.3.1 Specimen preparation

Porcine Biceps femoris muscle was first cut from a ham of an 8-month-old female swine raised by Department of Animal Sciences, Purdue University right after it was slaughtered. To keep the muscle tissue activity as long as possible, the porcine muscle was kept in a modified Kreb solution (136 mM NaCl, 4 mM KCl, 2.35 mM CaCl2, 1 mM NaH2PO4, 0.85 mM MgCl2, 12 mM NaHCO3, 5 mM glucose, and pH=7.4) bubbled with 95% O2 and 5% CO2 at the swine body temperature of 39.2 °C [100], which is a simulation of the in vivo circumstance of swine. Then approximately 4-mm thick muscle tissue was sliced with its surface parallel and perpendicular to fiber directions by using an electric meat slicer. Solid-disk shape specimens with a diameter of 9.5 mm (3/8”) and a thickness of 4 mm were then prepared from the 4-mm thick porcine muscle tissue by a sharp trephine right before the experiments. The thickness of each sample was measured by a caliper. A light source was put behind the sample as a guide such that no light passing through and there was no gap between the caliper’s jaws and the sample. All the prepared samples were kept in the same modified Kreb solution. Figure 2.1 is a photograph of an actual specimen with the direction of surface perpendicular to the fiber direction.

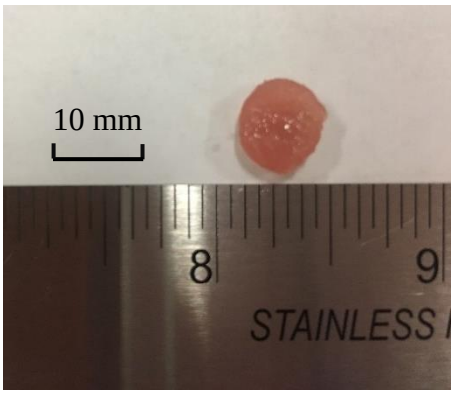

Figure 2.1 Photograph of a typical solid disk-shape porcine muscle specimen

2.3.2 Experimental setup

Unconstrained uniaxial compression experiment was performed to characterize the specimens’ compressive stress-strain response parallel and perpendicular to fiber direction at quasi-static (0.01/s and 0.1/s) and intermediate strain rates (10/s and 85/s) under 1-D stress loading. All

experiments were conducted using a hydraulically driven material testing system (MTS 810) with a nominally open-loop dynamic testing mode. The experiments conducted were within the US animal welfare regulations and guidelines. The testing system has a hydraulic power unit (HPU) charged accumulator, which is capable of supplying high volumes of hydraulic fluid quickly and therefore capable of reaching intermediate strain rates. A pair of grips made of aluminum alloy were connected to the actuator and load cell to apply unconstrained uniaxial compressive loads on the samples. Vegetable oil was used to minimize the frictions between the grips and the samples during the experiments. The displacement of the actuator was measured by an LVDT attached to the hydraulically driven frame and recorded by a digital oscilloscope. The recorded displacement data was directly used to calculate the strains in specimens as the maximum load needed to compress the specimens was too small (less than 40 N) to generate noticeable machine compliance errors (250 N for 0.1 mm). The forces on the specimens for intermediate strain-rate experiments were measured by a quartz piezoelectric load cell with a high-frequency response, while the forces for quasi-static experiments were measured by a strain-gage load cell. For the experiments at quasi-static strain rates, the sample was kept hydrated by irrigation of the modified Kreb solution. While, for experiments at intermediate strain rates, the sample was still in a hydrated state thanks to the residual solution on it since the whole deformation process lasted less than a few seconds. A schematic of the experimental setup is shown in Fig. 2.2.

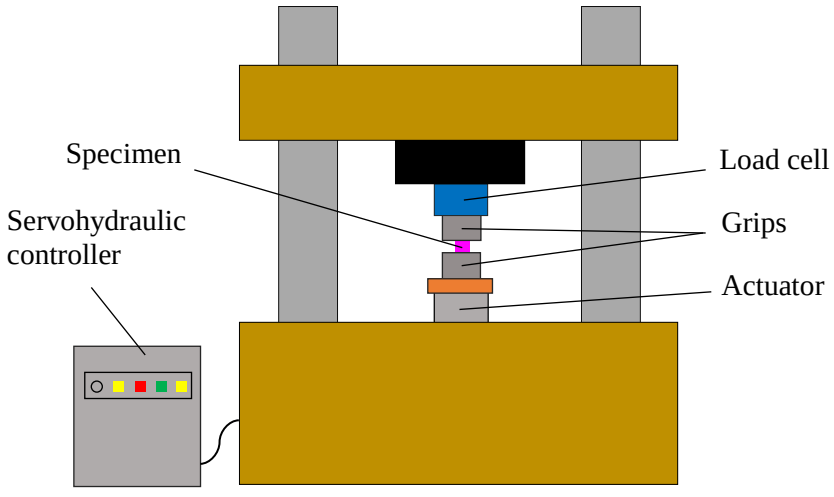

Figure 2.2 A schematic of the hydraulically driven material testing system

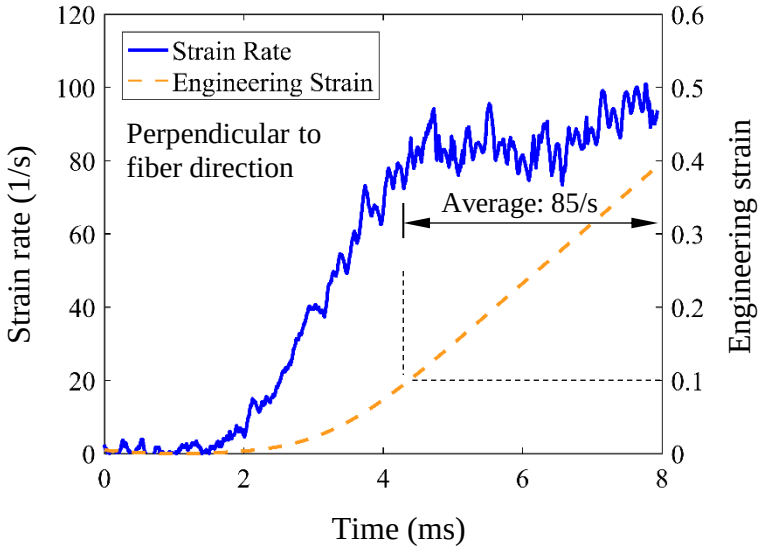

Figure 2.3 Typical strain-rate and engineering strain histories in a representative porcine muscle specimen

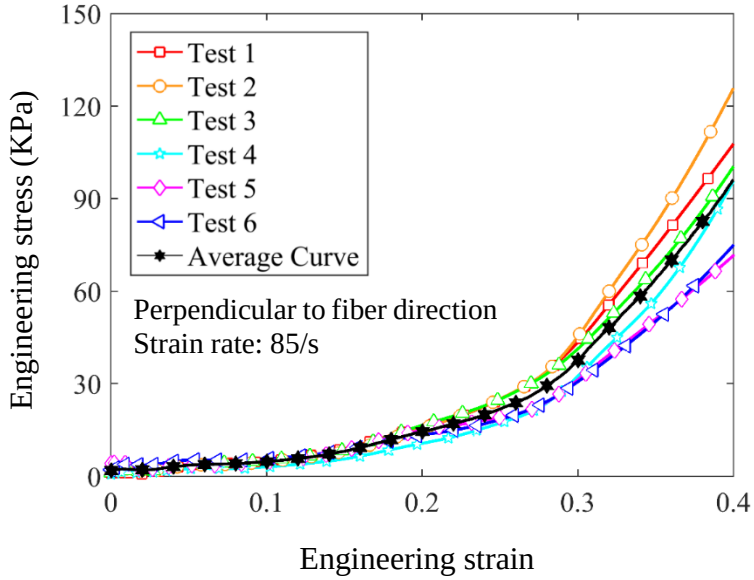

Figure 2.4 Compressive stress-strain curves of 6 porcine muscle specimens perpendicular to fiber direction at strain rate of 85/s and their average

A typical set of strain rate and strain histories of a specimen are shown in Fig. 2.3, from which it was observed that the specimen deformed with a low initial strain acceleration and then at a nearly constant strain rate (average strain rate is 85/s in the strain range of 0.1 to 0.4). The strain rate in Fig. 2.3 is calculated by taking derivative of strain with respect to time. The low initial

acceleration is required for avoiding inertial effects on the measured mechanical responses. For each strain rate and fiber direction, at least six specimens were measured under identical experimental conditions to ensure data repeatability. The stress-strain curves of the six specimens perpendicular to fiber direction together with their average curve at the strain rate of 85/s are shown in Fig. 2.4. The maximum extra stress due to radial inertia at strain rate of 85/s for the solid-disk shape specimen used in this work was calculated by the loading acceleration to be 0.9 kPa by using the equation (2.7) in [101], which is less than 1% of the strength of specimen and hence could be ignored.

2.4 Results & Discussions

The resultant compressive stress-strain curves of specimens with loading directions parallel and perpendicular to fiber direction are presented in Fig. 2.5a and b, respectively. Each curve in the two figures represents the average value of at least six repeated experiments performed under identical experimental conditions. Standard deviations for each strain rate and fiber orientation case are also plotted on the average stress-strain curves to show data scatter. The compressive stress-strain data at quasi-static strain rate and high strain rate from Song's work on porcine muscle are also shown in Fig. 2.5a and b for comparison [21]. The results show that the compressive stress-strain responses of porcine muscle at intermediate strain rates obtained in the present work are non-linear and strain-rate dependent. The stress-strain curves consist of three regions: a toe region, a non-linear transitional region, followed by a stiffening region, which is consistent with those experimental results of porcine muscle obtained previously at quasi-static and high strain rates [21]. The results in Fig. 2.5a and b show that the quasi-static stress-strain curves (0.1/s) obtained in this study agree well with that obtained previously (0.07/s and 0.06/s) for both parallel and perpendicular to fiber direction [21]. The results also show that the stress-strain data obtained in this study generally falls in the gap between quasi-static and dynamic rates reported previously on porcine muscle [94] except that the stresses at 85/s strain-rate perpendicular to fiber direction are slightly higher than that of 540/s from [21]. One of the possible reasons is the annular-shape specimens were utilized previously to minimize inertia effects during Kolsky bar compression in [21].

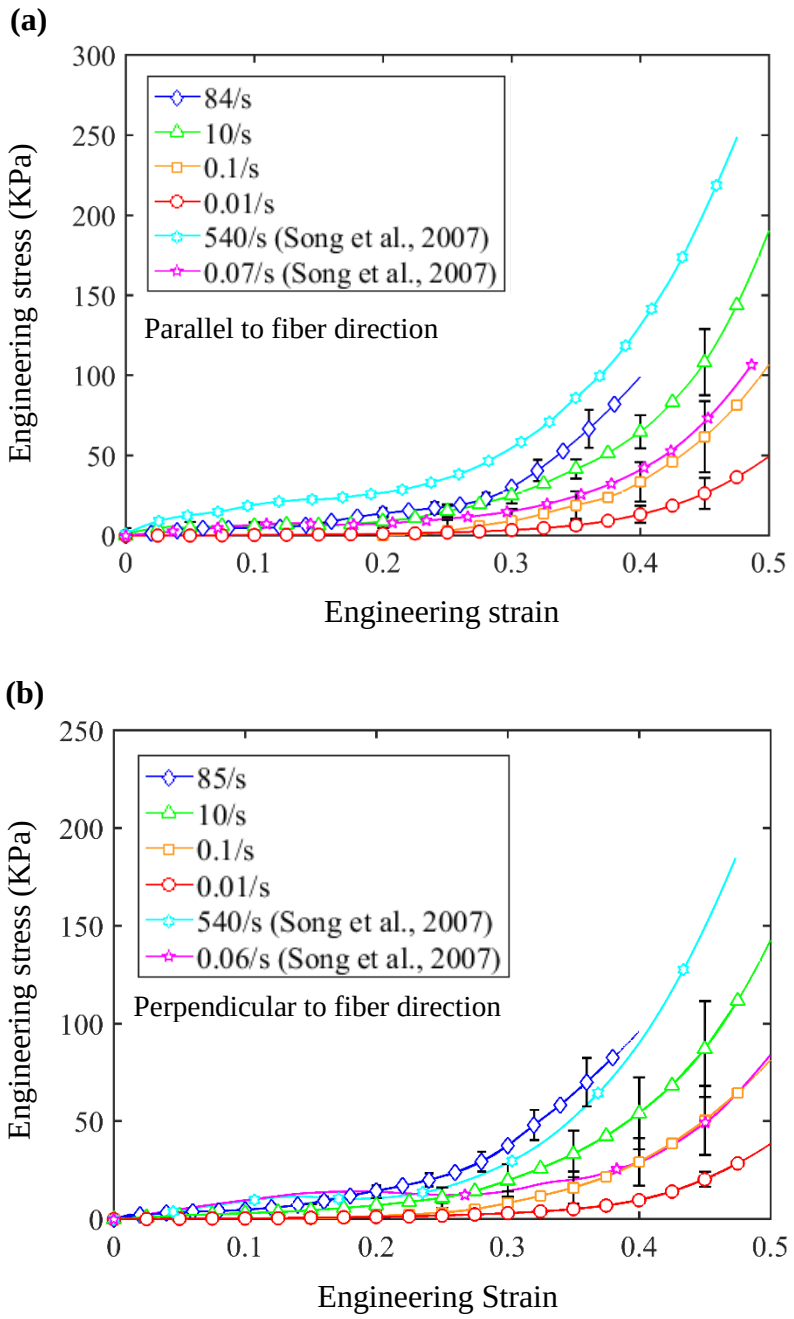

Figure 2.5 Compressive stress-strain curves of porcine muscle at various strain rates, showing the data for (a) loading direction parallel to fiber direction, (b) loading direction perpendicular to fiber direction

Figure 2.6 provides a quantitative comparison of stresses between the two fiber orientation cases at 40% engineering strain. The difference ratios are 26.7 %, 12.8 %, 16.6 % and 3.1 % for strain rate of 0.01/s, 0.1/s, 10/s and 84/s, respectively. To rigorously evaluate the effect of fiber

orientation on the stress-strain response of porcine muscle at various strain rates, statistical hypothesis tests (t-tests) were performed. The Kolmogorov-Smirnov normality tests (K-S tests) were first conducted to examine the normality of the experimental results in order to further perform the t-tests. As shown in Table 2.1, at the 0.05 level, it was concluded that all the experimental results were significantly drawn from a normally distributed population. That is to say if the p-value is greater than 0.05, the result was normally distributed. *t*-Test was then performed for stresses for the two fiber orientation cases at strain rates of 0.01/s, 0.1/s, 10/s and 84/s. At the 0.05 level, it was concluded that the compressive stresses of porcine muscle at 40% engineering strain at all the studied strain rates resulted in no significant difference between parallel and perpendicular to fiber direction cases. It is well known that muscle is composed of multiple bundles of muscle fibers called fascicles. Muscle fibers, in turn, are composed of myofibrils, which are built from repeated sarcomeres. The layers of connective tissue (ECM), enclosing each fascicle and separating each muscle fiber are called perimysium and endomysium, respectively [19, 93]. Because that muscle fibers could hardly bear compressive loads in the longitudinal direction or that the muscle fiber is a significantly less stiff structure comparing with ECM [19, 27], ECM such as perimysium and endomysium act as the main passive load bearing structures for compressive loadings both parallel and perpendicular to fiber directions. Thus, the independence of porcine muscle's compressive stress-strain response on fiber direction observed in this study could presumably be due to the similar strain resistance of the approximately isotropic ECM [20] to compressive loadings. Figure 2.7a and b show the variations of stresses as a function of strain rate at the engineering strain of 10 %, 25 %, and 40 % for both specimen orientation cases. The data for porcine muscle obtained previously [21] are also shown in both figures for comparison. It should be noted that each data point obtained in the current research stands for the average value of at least six repeated experiments. Strain-rate effect even within the intermediate strain rate range is evident in the stress-strain behavior of porcine muscle tissue for both the parallel and perpendicular to fiber direction cases as shown in Fig. 2.7a and b. It should be noted that we here measured the stress-strain behaviors of fresh passive muscle. In reality, the muscle tissue subjected to intermediate strain-rate loadings involved in dynamic events are active muscle and its mechanical properties could be different from that of passive muscle.

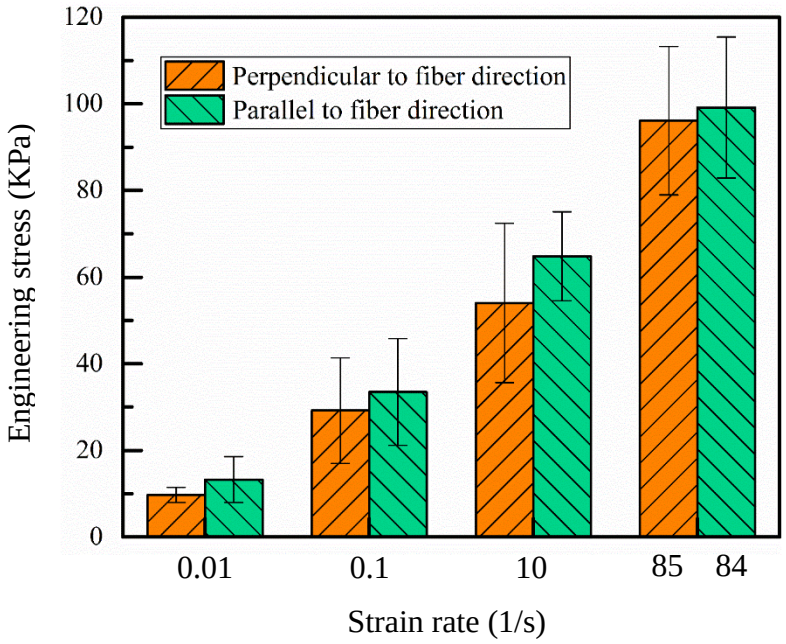

Figure 2.6 Stresses at various strain rates at 40% engineering strain perpendicular and parallel to fiber direction (mean values with standard deviations)

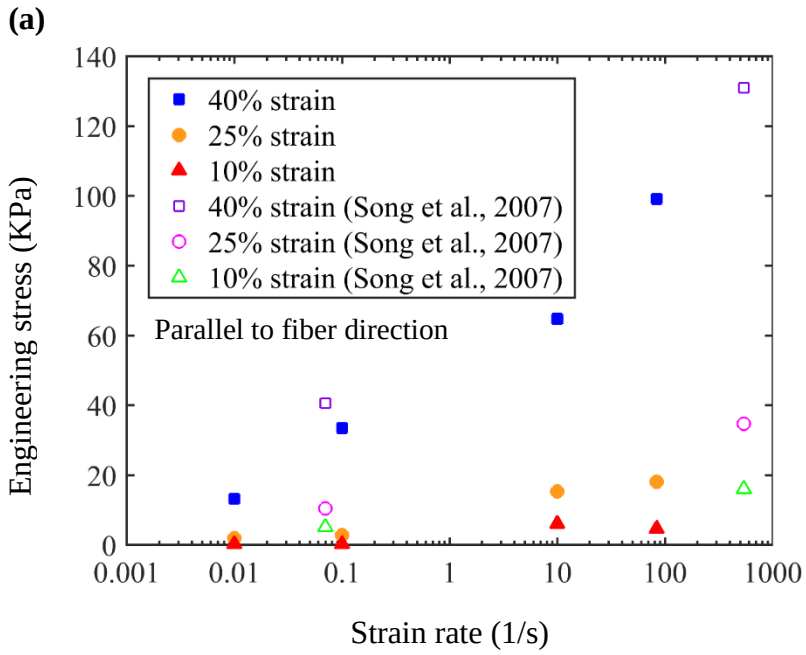

Figure 2.7 Strain rate effect of porcine muscle, showing the data for a) loading direction parallel to fiber direction, b) loading direction perpendicular to fiber direction

Figure 2.7 continued

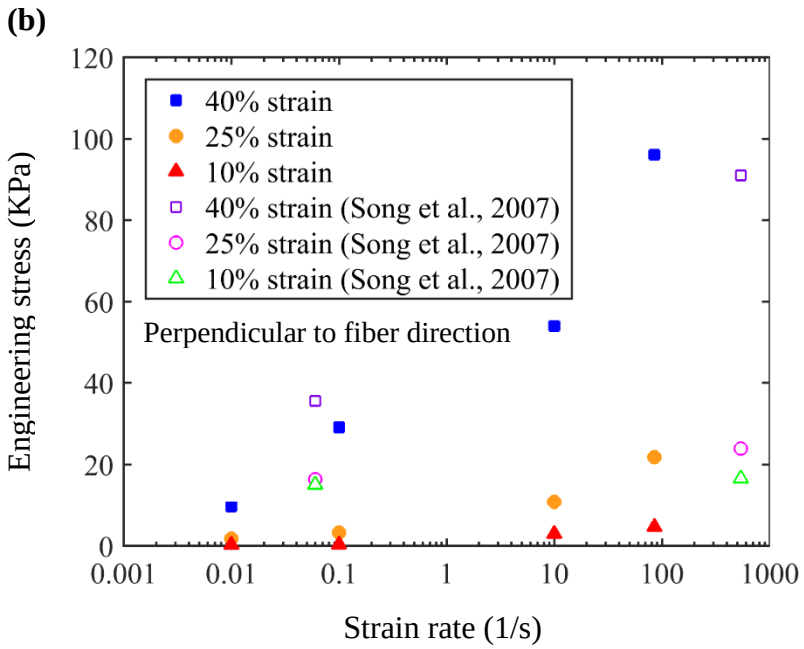

Table 2.1 P values from Kolmogorov-Smirnov normality test

Strain rate(/s)	Stress at 40% engineering strain	
	Parallel	Perpendicular
0.01	0.56	1
0.1	1	0.90
10	1	1
84/85	0.80	1

2.5 Constitutive model

Due to the high liquid content in muscle tissue and relative high stiffness of the connect tissue combined with the low stiffness of muscle fibers, the skeletal muscle exhibits an overall incompressibility in its response to mechanical loadings [102]. As a consequence, we used the Ogden model [103] for incompressible, isotropic, hyperelastic materials here for the descriptions of the non-linear compressive stress-strain response of porcine muscle tissue. The Ogden model was first developed by Ogden and has been widely applied to determine the wide range of strain

hardening characteristics of hyperelastic materials, such as rubbers, polymers and biological tissues [22]. The one-term Ogden model has the form of

$$W(\lambda_1,\lambda_2,\lambda_3)=\frac{2\mu}{\alpha^2}(\lambda_1^{\alpha}+\lambda_2^{\alpha}+\lambda_3^{\alpha}-3) \tag{2.1}$$

where W is the strain energy density per undeformed unit volume, λ_i $(i=1,2,3)$ is the principal stretch ratio (in a Cartesian reference coordinate), μ is the shear modulus under infinitesimal strain and has the interpretation of strain hardening exponent. In a uniaxial compressive experiment with the 1-axis aligned with the loading direction ($\sigma_2=0, \sigma_3=0$), the porcine muscle specimen is considered to be incompressible. Therefore, the specimen's principal stretch ratios satisfy the constraint as shown in Equation (2.2).

$$\frac{1}{\sqrt{\lambda_1}}=\lambda_2=\lambda_3 \tag{2.2}$$

The strain energy function now can be expressed as a function of one stretch ratio by Eqs. (2.1) and (2.2):

$$W(\lambda_1)=\frac{2\mu}{\alpha^2}(\lambda_1^{\alpha}+2\lambda_1^{-\frac{\alpha}{2}}-3) \tag{2.3}$$

The nominal stress σ_1 in the uniaxial compressive experiments is given by:

$$\sigma_1=\frac{\partial W}{\partial \lambda_1} \tag{2.4}$$

and for uniaxial compressive experiments, Eq (2.4) could be further reduced to

$$\sigma_1=\frac{2\mu}{\alpha}\left[\lambda_1^{\alpha-1}-\lambda_1^{-1-(\alpha/2)}\right] \tag{2.5}$$

The two constants α and μ used in the Ogden model for the porcine muscle can be determined by the experimental data obtained in this research.

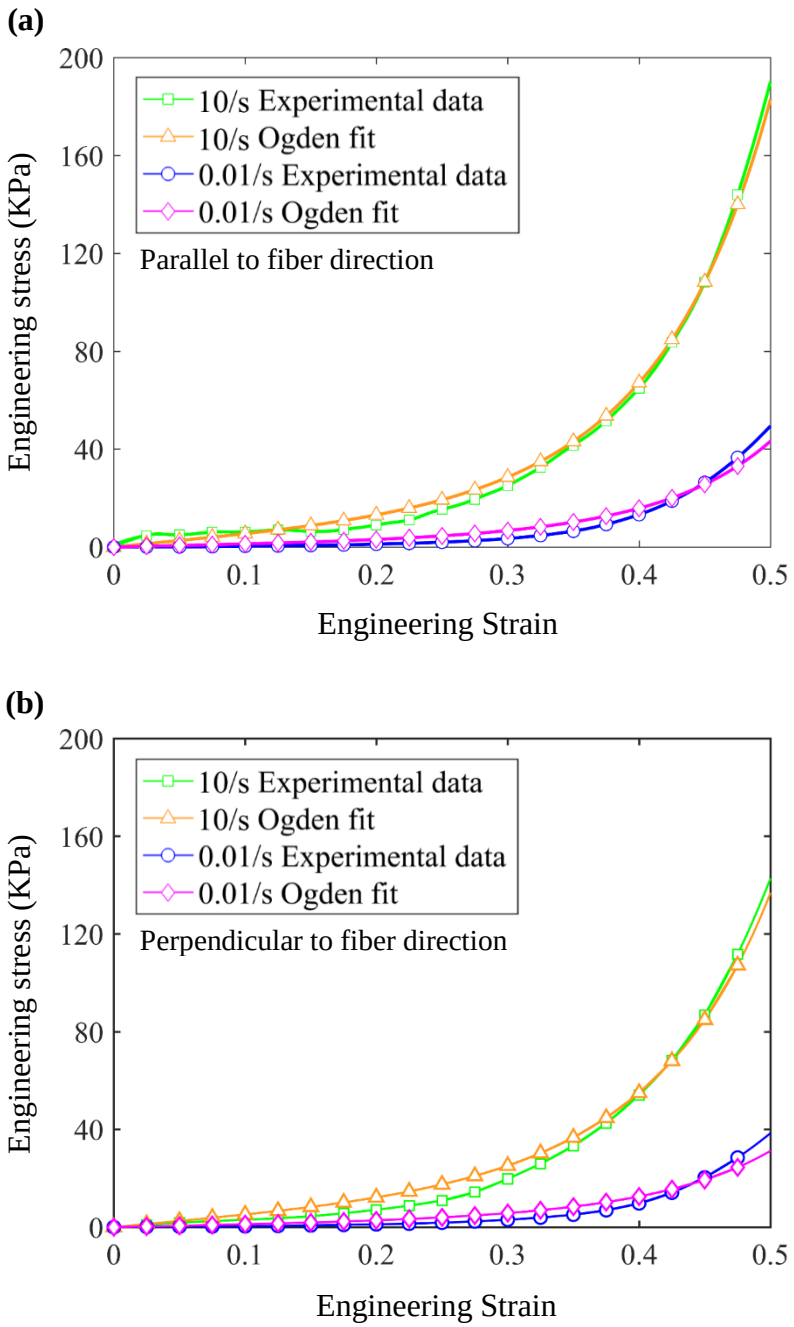

Figure 2.8 Ogden fit of the measured compressive stress-strain response of porcine muscle, showing the data for (a) loading direction parallel to fiber direction, (b) loading direction perpendicular to fiber direction

Figure 2.8a and b show the Ogden fits for the measured stress-strain responses of porcine muscle in compressive experiments at quasi-static and intermediate strain rates for the two specimen orientation cases. The Ogden constants evaluated experimentally are summarized in

Table 2.2. The results in the two figures show that the Ogden model provides a good curve fit for the porcine muscle at all strain rates considered in this work.

Table 2.2 Ogden constants (μ and α) evaluated at different strain rates for porcine muscle

Strain rate (/s)	Shear modulus, μ (kPa)		Strain hardening exponent, α	
	Parallel	Perpendicular	Parallel	Perpendicular
0.01	4.3	3.9	9	8
0.1	10.0	9.5	9	8
10	18.2	17.1	9	8
84/85	23.9	27.9	9	8

2.6 Conclusions

The stress-strain response of passive porcine muscle was experimentally studied under unconstrained uniaxial compressive loading conditions at both quasi-static and intermediate strain rates. A hydraulically driven material testing system with a nominally open-loop testing mode for intermediate strain rates was utilized to perform all the experiments on the porcine muscle along directions parallel and perpendicular to the muscle fiber direction. A quartz piezoelectric load cell and a strain gage load cell were used to measure the forces in the experiments at intermediate strain rates and quasi-static strain rates, respectively. The strain rates were controlled to be constant during the experiments after initial rises. Strain-rate effects on the non-linear stress-strain response of porcine muscle were found to be evident from the experimental results for both specimen orientations. The compressive stress-strain response of porcine muscle at quasi-static and intermediate strain rates was found to be insensitive to the two fiber orientations studied in this work (parallel and perpendicular to fiber direction). A one-term Ogden model is used to describe the compressive stress-strain response of porcine muscle at each strain rate. Two material constants are shown to be sufficient for a good description of the experimental data over a wide range of strain rates achieved in this study.

CHAPTER 3. QUASI-STATIC AND DYNAMIC MECHANICAL RESPONSE OF HUMAN MUSCLE

Adapted from:
X. Zhai, E.A. Nauman, Y. Nie, H. Liao, R.J. Lycke, W.W. Chen. Mechanical Response of Human Muscle at Intermediate Strain Rates, Journal of Biomechanical Engineering. 141 (2019), 044506. (with permission from ASME)

3.1 Abstract

We experimentally determined the tensile stress-strain response of human muscle along fiber direction and compressive stress-strain response transverse to fiber direction at intermediate strain rates (10^0-10^2/s). A hydraulically driven materials testing system with a dynamic testing mode was used to perform the tensile and compressive experiments on human muscle tissue. Experiments at quasi-static strain rates (below 100/s) were also conducted to investigate the strain-rate effects over a wider range. The experimental results show that, at intermediate strain rates, both the human muscle's tensile and compressive stress-strain responses are non-linear and strain-rate sensitive. Human muscle also exhibits a stiffer and stronger tensile mechanical behavior along fiber direction than its compressive mechanical behavior along the direction transverse to fiber direction. An Ogden model with two material constants was adopted to describe the nonlinear tensile and compressive behaviors of human muscle.

3.2 Introduction

Human muscle, a soft tissue, makes up about 40 percent of human body weight and thus plays a significant role in dissipating impact energy when the body is subjected to high strain-rate loading. Skeletal muscle attaches to bone through tendon and is primarily responsible for skeletal movements, such as changing posture and locomotion, and therefore is expected to experience additional high strain-rate loading during dynamic events. This study is focused on the dynamic behavior of skeletal muscle.

The mechanical properties of animal muscle tissues have been reported to be nonlinear and strain rate sensitive [13, 16, 21, 22, 24-26, 104]. Uniaxial compressive experiments on passive bovine muscle, porcine muscle and ovine muscle provide evidence that they are both strain-rate

sensitive and dependent on fiber orientation [16, 104]. Tensile experiments at quasi-static strain rates on passive porcine muscle [24] and rabbit muscle [25, 26] were conducted to investigate the effect of loading directions on their mechanical properties. While stiffer transverse tensile stress-strain behaviors at small strains were observed for porcine muscle [24] and rabbit muscle [25], a stiffer longitudinal tensile stress-strain response was reported for rabbit muscle by Morrow et al. [26]. Within the range of high strain-rate, the dependency of porcine muscle on strain rate is more significant in its transverse fiber direction than along the fiber direction [21]. In comparison, the strain rate sensitivity of porcine muscle in tension exhibits less significant dependency on fiber orientation to loading direction [22]. The energy dissipated by rabbit muscle was reported to be strain-rate independent under cyclic tensile loadings [14]. Recent studies on load bearing mechanisms in muscle tissue suggested that extracellular matrix (ECM), including muscle endomysium, perimysium and epimysium, act as the major loading bearing structures in passive muscle [19, 27, 28]. By directly or indirectly measuring the tensile mechanical properties of ECM, researchers found that ECM was highly nonlinearly elastic and its modulus was inherently stiffer than muscle fibers under tensile loadings [27, 28].

In many of the dynamic cases when soft tissue damage occurs, such as vehicle collisions or sports accidents, soft tissues are subjected to intermediate strain-rate (10^0/s-10^2/s) loadings [85] [86]. In order to obtain accurate bioengineering models for those loading conditions, there is a need to evaluate the mechanical response of human skeletal muscle at intermediate strain-rate and to build appropriate constitutive models. However, experimental data of passive human muscle is very limited in this range of strain rates. Two important challenges are the lack of well-established experimental techniques for the mechanical characterization of soft tissues at intermediate strain-rates and the difficulty obtaining human tissue specimens in sufficient quantities. Furthermore, at intermediate strain rates, inertia effects which could begin to interfere with the stress equilibrium state are no longer negligible [105]. Such inertia effect has been minimized in the measurements of steels at intermediate strain-rate experiments by numerically using a cubic spline approximation [106] or experimentally using a passive damping structure [107]. In this work, we experimentally investigated the tensile and compressive stress-strain response of human muscle tissue at quasi-static and intermediate strain rates.

3.3 Material & Methods

3.3.1 Specimen preparation

Human muscle tissue was obtained from the right leg of a 59 years old white male donor. The donor's primary cause of death was atherosclerotic cardiovascular disease, which presumably did not affect the muscle tissue studied in this work. The human leg was shipped and received in a frozen state and stored immediately in a freezer at a temperature of -20 °C. Before experiments, the leg was thawed at room temperature for about 12 hours. Several cutting molds were made with two parallel slides with fixed distances, where razor blades were inserted to cut specimens into various dimensions. After removing the skin, human muscle tissue was carefully extracted from the Biceps femoris, Vastus lateralis and Vastus medialis muscle of the leg and then cut into strip-shape specimens for tensile experiments and solid-disk shape specimens for compressive experiments by the cutting molds and sharp trephines. The strip-shape specimens were approximately 70 mm in length, 10 mm in width and 5 mm in thickness, while the solid-disk shape specimens were 9.5 mm in diameter and 4 mm in thickness (Fig. 3.1). Images for each strip-shape specimens were taken before the experiments to measure the dimensions of the specimens precisely. All the prepared human muscle specimens were stored at 5 °C in 0.9 % Sodium Chloride irrigation solution until the experiments were performed within 24 hours of specimen preparation to ensure the specimens' uniformity as much as possible.

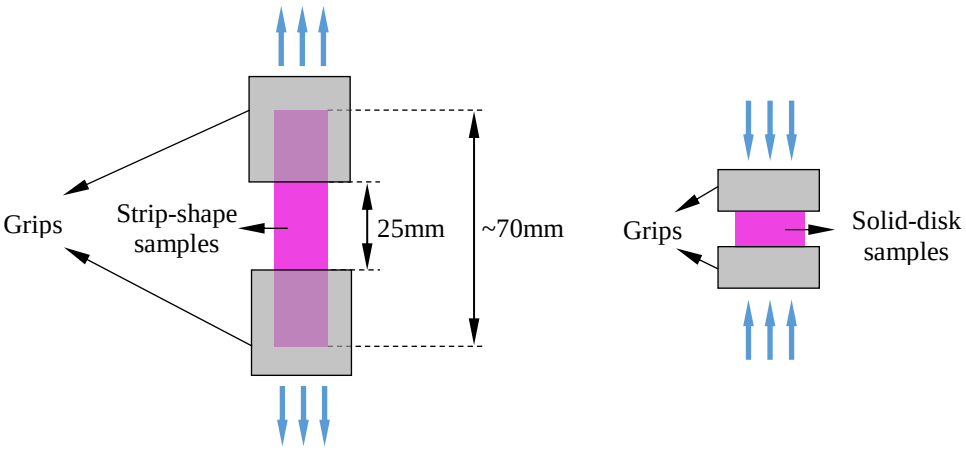

Figure 3.1 Schematic of the human muscle samples

3.3.2 Experimental setup

Due to the prevailing loading conditions on human muscle tissues and limited availability of specimen, unconstrained uniaxial tensile experiments along fiber direction and compressive experiments transverse to fiber direction were performed to characterize the specimen's tensile stress-strain response at quasi-static (0.01/s) and intermediate strain rates (10/s, 90/s and 100/s) under 1-D stress loading (Fig. 3.1). All experiments were conducted using a hydraulically driven materials testing system (MTS 810). The displacement of the actuator was measured by a linear variable differential transducer (LVDT) installed in the hydraulically driven frame and recorded by a digital oscilloscope. The strains within each specimen were calculated by using the recorded displacement data. The forces on both the bottom and top ends of the for intermediate strain-rate experiments were measured by a pair of quartz piezoelectric load cells (Type 9212; Kisler, NY, U.S.) with high-frequency responses and a capacity of ~222 N (50 lbf), while the forces for quasi-static experiments were measured by a strain-gage load cell (1500 ASk-50; Interface, AZ, U.S.) mounted on the fixed end of the load frame (Fig. 3.2). The capacity of the strain-gage load cell was also ~222 N (50 lbf). A pair of aluminum grippers with rough sand-paper surfaces on both its fixed part and movable part were used for the tensile experiments (Fig. 3.2b). The gage length for all the tensile experiments was 25 mm, while the gage lengths for the compressive experiments were the actual thicknesses measured on individual samples.

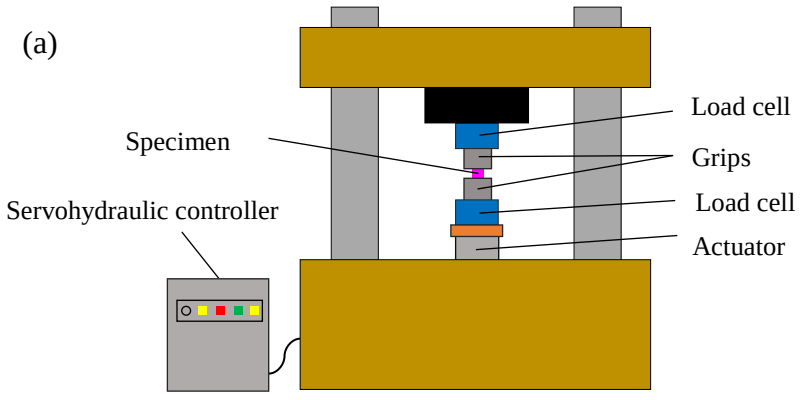

Figure 3.2 Schematic of the experimental setup (a) hydraulically driven materials testing machine (b) Grippers for tensile experiments

Figure 3.2 continued

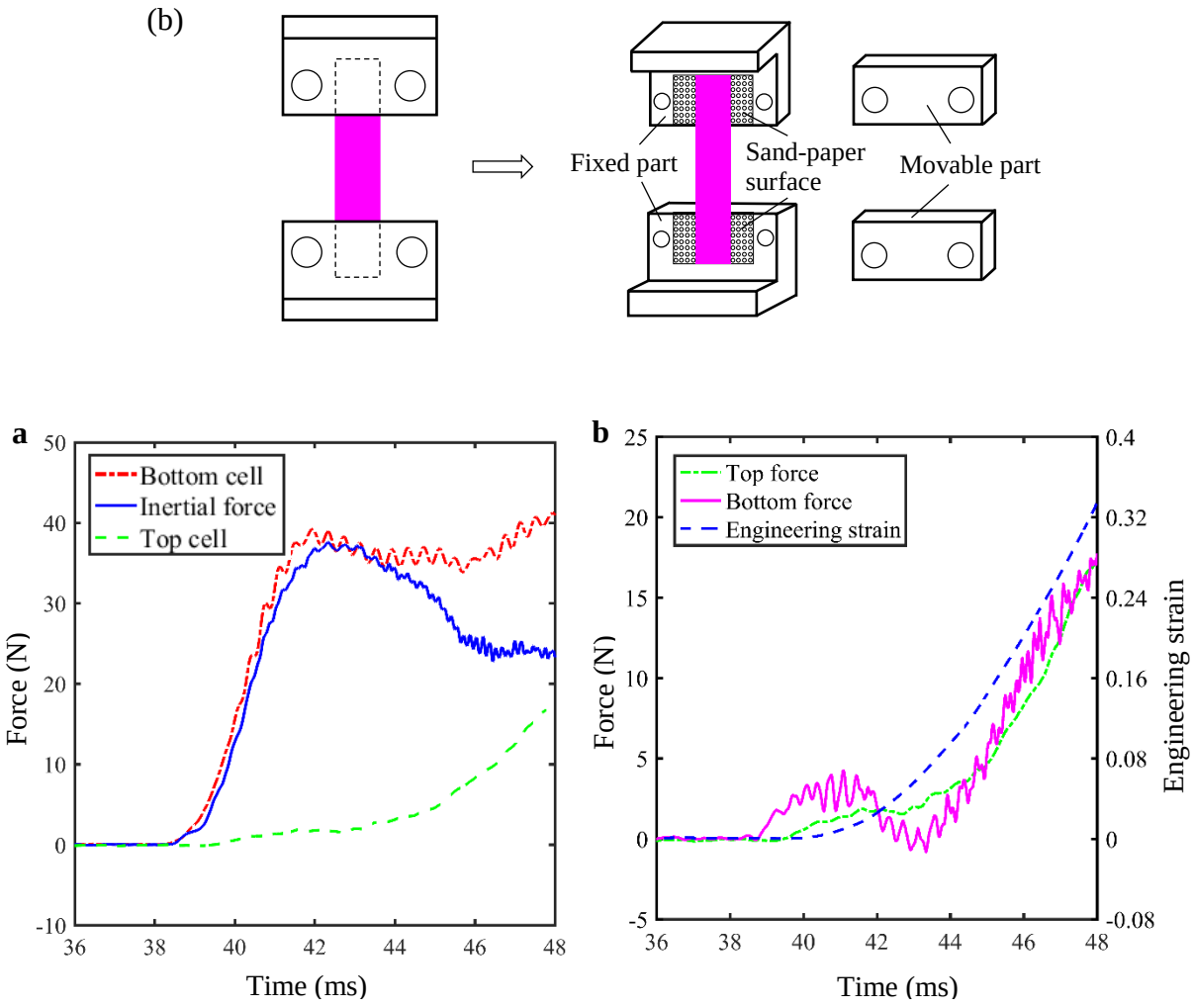

Figure 3.3 Representative data for tensile experiments at strain rate of 100/s (a) Original force-time profiles from top, bottom load cell and calibration experiment without specimen, (b) Actual force-time profiles at top and bottom ends of specimen together with the strain-time profile

Inertia forces caused by actuator and grippers in intermediate strain-rate experiments were determined by running experiments under identical conditions without specimens. Data analysis for tensile and compressive experiments are summarized in Figs. 3.3 and 3.4 using an example at a strain rate of 100 /s and 90/s, respectively, where actual forces applied on the bottom ends of specimens were calculated by subtracting the forces due to inertia from the recorded bottom forces. As shown in Figs. 3.3 and 3.4, the specimens were loaded in stress-equilibrium states in both tensile and compressive experiments. For each strain rate case for both the tensile and compressive

experiments, at least four specimens were measured under identical experimental conditions to ensure data repeatability.

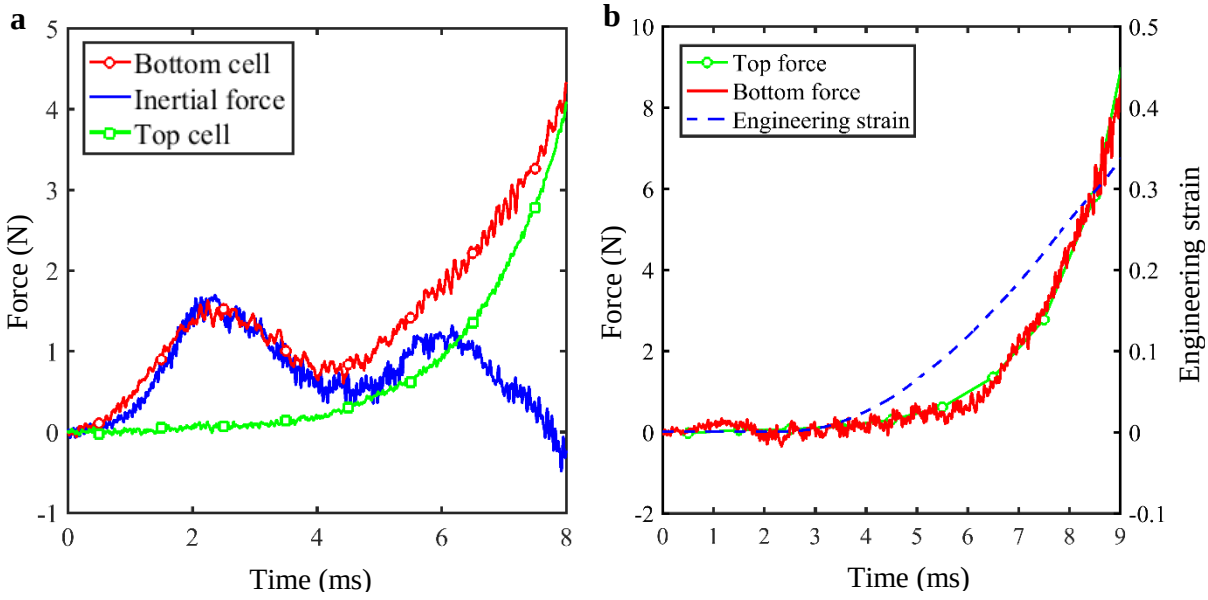

Figure 3.4 Representative data for compressive experiments at strain rate of 90/s (a) Original force-time profiles from upper, lower load cell and calibration experiment without specimen, (b) Actual force-time profiles at top and bottom ends of specimen together with the strain-time profile

3.3.3 Constitutive model

The Ogden model [103] has been widely used to describe the strain hardening characteristics of soft tissues. As the principle axes are aligned with the loading direction and by assuming the human muscle specimen is incompressible, the one-term Ogden model yields the nominal stress σ_1, as provided in [108]:

$$\sigma_1 = \frac{2\mu}{\alpha}\left[\lambda_1^{\alpha-1} - \lambda_1^{-1-(\alpha/2)}\right] \tag{3.1}$$

where λ_1 is the principal stretch ratio in the loading direction, μ and α are the infinitesimal shear modulus and strain hardening exponent, respectively, which could be determined by fitting the model into experimental stress-strain curve.

3.4 Results & Discussions

The resultant tensile stress-strain curves along fiber direction and compressive stress-strain curves transverse to fiber direction of specimens are presented in Fig. 3.5a and b, respectively. The engineering strain of human muscle's tensile stress-strain response at strain rate of 100/s starts from 5% to avoid the non-constant strain rate section (Fig. 3.5a). Each curve (in Fig. 3.5a and b) represents the average value (with standard deviation) of at least four specimens conducted under identical conditions. The specimens under tensile loading at 10/s were not deformed to breakage at the end of loading process at engineering strain of 25%. The experimental results show that both the tensile and compressive stress-strain responses of human muscle at intermediate strain rates are non-linear and strain-rate sensitive. The compressive stress-strain curves consist of three regions: toe region, non-linear transitional region and a stiffening region, which is consistent with those experimental results of porcine muscle reported previously at quasi-static and high strain rates [14]. The specimens' tensile stress-strain curves are r-shaped and divided into three regions. The first region is regarded as a rapid initial rise in stress, where the sarcomere-perimysium complex is considered to be responsible for deformation resistance [109]. As strain accumulates rapidly with a comparative minimal increase in stress in the second transitional region, sarcomeres continue to be stretched and rupture of connective tissue and sarcolemma takes place on the fiber surface. The third region is characterized by the drop of stress, in which the failure of myofibrils takes place and finally the whole fiber breaks [109].

The quasi-static compressive stress of postmortem porcine muscle perpendicular to fiber direction was reported to be ~20 KPa at engineering strain of 40% by van Loocke *et al*. [16]. While compressive stress of fresh porcine muscle were reported differently in separate studies, as they were ~29 KPa in Song *et al*. [21] and ~5 KPa in van Loocke *et al*. [16]. The transverse compressive stress of human muscle at 40% engineering strain obtained in our study was ~10 KPa. The difference may be due to variations in species, anatomic locations and postmortem time. On the other hand, quasi-static tensile stress of fresh porcine muscle [24] and fresh rabbit muscle [25] along fiber direction were measured previously to be ~100 KPa and ~50 KPa at 30% engineering strain, respectively. However, the tensile stress of postmortem frozen-thawed rabbit muscle [25] and fresh-frozen rabbit muscle [26] were investigated in separate studies under similar testing conditions, as they were reported differently to be ~100 KPa [25] and ~130 KPa [26], which agreed well with our data, as measured here to be ~134 KPa.

As shown in Fig. 3.5, at the same strain rate, human muscle specimens behave stiffer under tensile loading along fiber direction than under compressive loading transverse to fiber direction. There could be multiple reasons lead to this phenomenon. One major reason is the differences in the muscle fiber and ECM's strain resistances under along-fiber stretching and transverse-to-fiber compressing loading conditions. For the case of tensile loading along fiber direction, force could be largely attributed to the ECM based on the previous evidence that ECM was the main bearing structure in passive muscle under tensile loadings [19, 27]. Both muscle fibers and ECM may act as the main load undertaking tissues when the specimens subjected to transverse compressive loading. The stiffer tensile stress-strain responses of human muscle along fiber direction observed in our study could presumably be due to the stiffer tensile properties of ECM when compared to the compressive properties of ECM and muscle fiber. Another reason could be the long fiber lengths in the tensile muscle samples investigated in this study. It is well known that the passive force-length behaviors of muscle tissues have a region of 'slack' [19, 110-112], in which the muscle tissue is easily to be axial lengthened without generating forces. In our study, the human muscle tissue was intentionally measured starting at a free stress state in tensile experiments. However, a pretension in the sample may be generated and hence the samples were likely out of the 'slack region', behaving stiffer under along-fiber stretching loading condition. The averaged stresses for the repeated experiments as a function of strain rate at different engineering strains for both the two loading cases were plotted, where the strain-rate effect was apparent in the range of intermediate strain rates (Fig. 3.6).

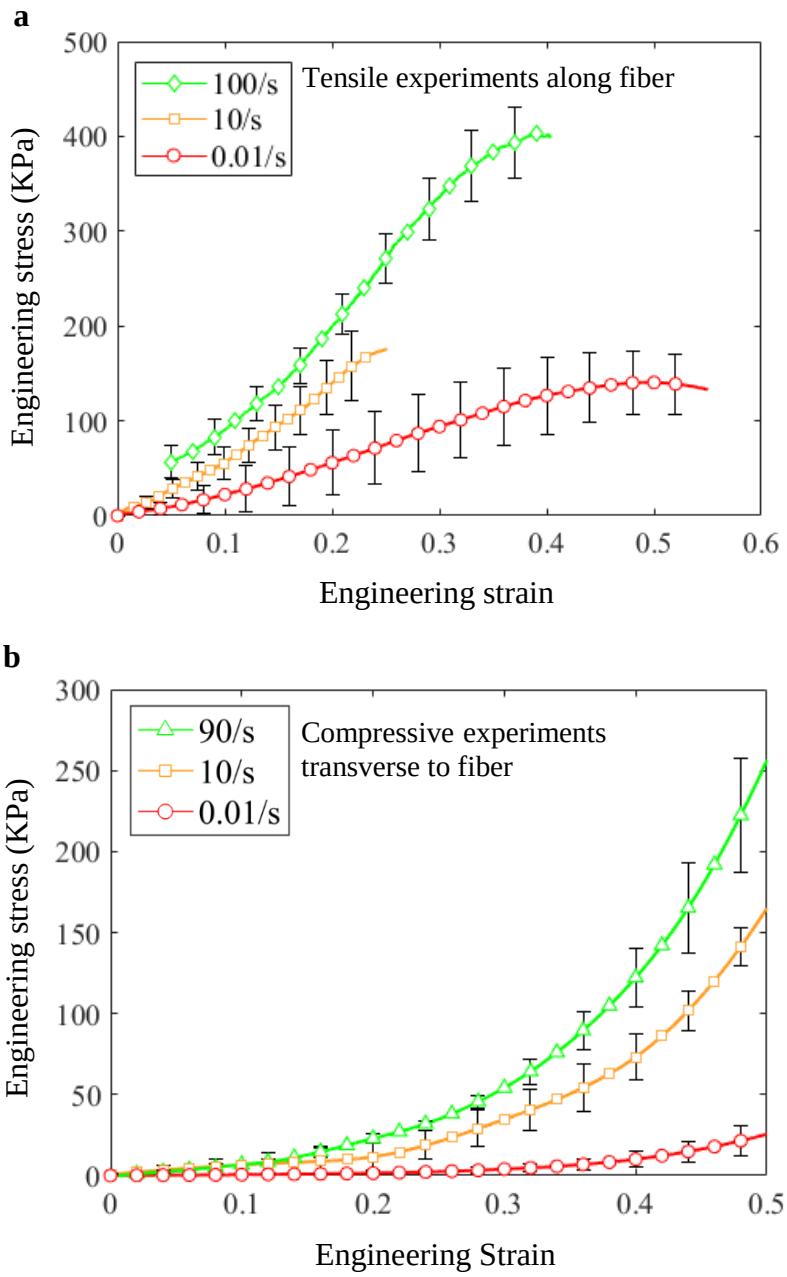

Figure 3.5 Stress-strain curves of human muscle at various strain rates (a) average tensile stress-strain curves along fiber direction with standard deviation (b) average compressive stress-strain curves transverse to fiber direction with standard deviation

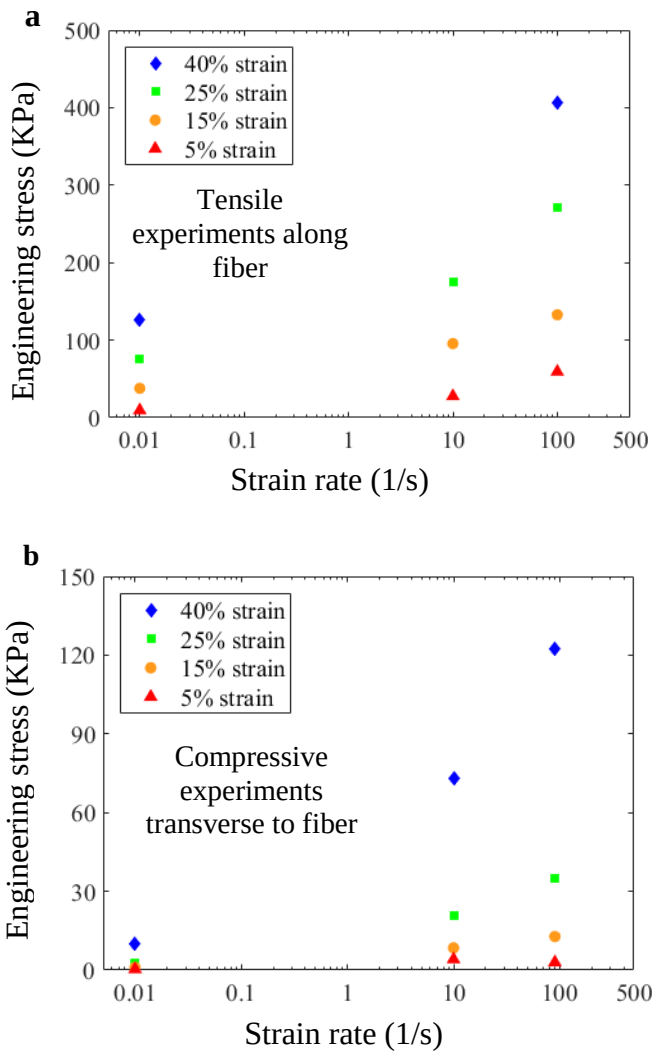

Figure 3.6 Strain rate effect of human muscle under along-fiber tensile loading and cross-fiber compressive loading (a) Strain rate effect of tensile response of human muscle along fiber direction (b) Strain rate effect of compressive response of human muscle transverse to fiber direction

The resulting Ogden fits (Fig. 3.7) achieves reasonable curve fit for the experimentally measured stress-strain curves of human muscle at quasi-static and intermediate strain rates. The two Ogden materials parameters evaluated experimentally are summarized in Table 3.1, where the adjusted R-Square were also summarized to quantify the curve fit.

Table 3.1 Ogden constants (μ and α) evaluated at different strain rates for human muscle and adjusted *R*-Square of the Ogden fits

Strain rate(/s)	μ (kPa)		α		Adjusted *R*-Square	
	TA	CT	TA	CT	TA	CT
0.01	79.2	3.2	6	8	0.91	0.99
10	201.3	22.0	6	8	0.99	0.99
100/90	298.3	35.2	6	8	0.94	0.99

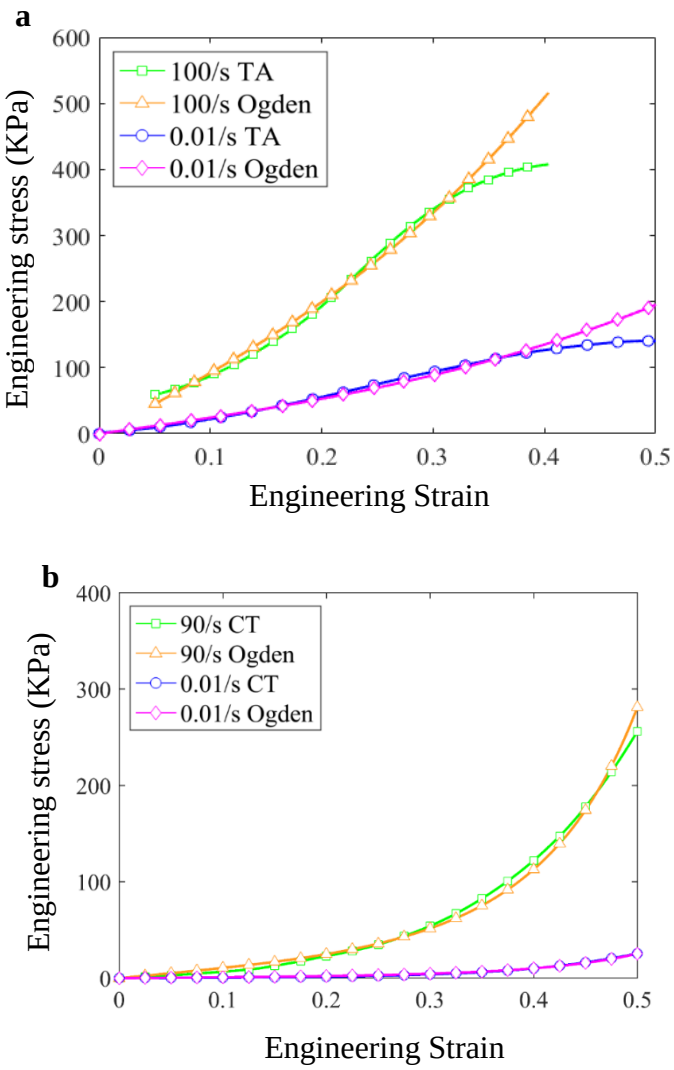

Figure 3.7 Ogden model fit of the human muscle's stress-strain response (a) Stress-strain response of human muscle parallel to fiber direction (b) Stress-strain response of human muscle perpendicular to fiber direction

3.5 Study limitations and improvements

Although this study effectively investigates the compressive and tensile stress-strain properties of human muscle at quasi-static and intermediate strain rates, there exist some unavoidable limitations and further studies are needed to build a full understanding of human muscle behavior. First, due to the limited amount of muscle samples that could be extracted from a single muscle group, samples in this study were prepared from three different thigh muscle. Additionally, since the total availability of muscle tissue was limited, only tensile experiments along fiber direction and compressive experiments transverse to fiber direction were performed, which were more common loading conditions in practice. Furthermore, the freeze-thaw process exerted on the human muscle specimens could influence their mechanical properties. However, previous studies on postmortem skeletal muscle [113] provided evidence that a freeze-thaw cycle had no effect on their passive mechanical properties. Accordingly, such specific effect, if existing in our study, was likely limited. Finally, the experimental results in this study were obtained only on the tissues from one donor. Effects such as age and gender are yet to be studied.

3.6 Conclusions

The specimens were deformed in stress equilibrium state during the tensile and compressive experiments. Strain-rate effects on the non-linear stress-strain responses of human muscle were found to be evident. It is likely that because of the stiffer tensile properties of ECM and long fiber length of the tensile sample investigated in this study, the human muscle exhibits a stiffer longitudinal tensile stress-strain behavior than transverse compressive stress-strain behavior. A one-term Ogden model with two material parameters is shown to be sufficient to describe the experimental data over a wide range of strain rates achieved in this work.

CHAPTER 4. HIGH-SPEED X-RAY VISUALIZATION OF DYNAMIC CRACK INITIATION AND PROPAGATION IN BOTH CORTICAL AND TRABECULAR BONES

Adapted from:
X. Zhai, Z. Guo, J. Gao, N. Kedir, Y. Nie, B. Claus, T. Sun, X. Xiao, K. Fezzaa, W.W. Chen. High-speed X-ray visualization of dynamic crack initiation and propagation in bone, Acta Biomaterialia. 90 (2015), 278-286.

4.1 Abstract

The initiation and propagation of physiological cracks in porcine cortical and cancellous bone under high rate loading were visualized using high-speed synchrotron X-ray phase-contrast imaging (PCI) to characterize their fracture behaviors under dynamic loading conditions. A modified Kolsky compression bar was used to apply dynamic three-point flexural loadings on notched specimens and images of the fracture processes were recorded using a synchronized high-speed synchrotron X-ray imaging set-up. Three-dimensional synchrotron X-ray tomography was conducted to examine the initial microstructure of the bone before high-rate experiments. The experimental results showed that the locations of fracture initiations were not significantly different between the two types of bone. However, the crack velocities in cortical bone were higher than in cancellous bone. Crack deflections at osteonal cement lines, a prime toughening mechanism in bone at low rates, were observed in the cortical bone under dynamic loading in this study. Fracture toughening mechanisms, such as uncracked ligament bridging and bridging in crack wake were also observed for the two types of bone. The results also revealed that the fracture toughness of cortical bone was higher than cancellous bone. The crack was deflected to some extent at osteon cement line in cortical bone instead of comparatively penetrating straight through the microstructures in cancellous bone.

4.2 Introduction

Bone is a typical composite and primarily consists of collagen and minerals [73]. It occurs in two types: as a dense solid tissue called cortical bone and a lattice-like network structure called cancellous bone. They are all responsible for protecting the inner soft tissues and thus could potentially undergo dynamic loading conditions during blast and impact events, such as car

collisions and sports accidents. For example, the in vivo loading rate in bone can reach a maximum impact velocity as high as ~7.5 m/s during a car crash [88]. Traumatic injuries in such scenarios can invariably lead to initiation and growth of cracks in the bone. Therefore, studying the fracture and toughening mechanisms of both cortical and cancellous bone under high rate loading conditions is of great importance to improve protective gear design and prevent fracture occurrence.

It is believed that the mechanical properties and fracture toughness of cortical bone are mainly construed by its complex architecture that builds hierarchically with collagen (protein) and hydroxyapatite (mineral) in multiple levels [1, 2]. Consequently, multiple crack initiation and toughening mechanisms owing to its microstructural hierarchies at different dimensional scales could be the primary contributions to its fracture resistance at low strain rates (10^{-5}/s-10^{-1}/s) [74, 75, 77]. As a large number of cracks occurring in bone are in microscopic length scales [74, 75], microstructure contributed mechanisms comparing with other toughening mechanisms act more effectively in fracture resistance in bone and thus need to be well understood. Indeed, there has been a large body of work studying the fracture behaviors at the microscopic level in mammalian cortical bone [37, 38, 42, 45, 73-82, 114], although most of them are focused on quasi-static strain rates (~10^{-5}-~10^{1}/s). Specifically, in the case where the crack-growth direction is perpendicular to the collagen fibrils, osteonal cement lines could deflect the crack 90 degrees to largely increase the driving force needed for subsequent crack propagation, leading to significant toughening. Therefore, this crack deflection was regarded as the major toughening mechanism [42, 76, 83]. However, under dynamic fractures, bone could exhibit a remarkably different behavior, showing a general transition from ductility to brittleness when compared with that under quasi-static rates [33, 52, 58, 59, 74, 89]. Studies at macroscopic length scales [30, 51, 58, 89, 115] revealed that, the fracture toughness of bone was lower and the fracture surface was less rough and more cleavage-like under dynamic loadings [30, 51, 58, 89, 115] when comparing with quasi-static loadings. Shannahan *et al*. [115] measured the mode I and mode II fracture initiation toughness separately and found a transition from mode II dominant fracture to a mixed mode (mode I and mode II) fracture as loading rate increased from quasi-static to dynamic. More interestingly, Behiri and Bonfield [30] found a critical range of loading rates in cortical bone, above which unstable fractures would occur in a sudden manner while below which fractures were stable and controllable.

Under impact and blast loading, skull or the ends of long bones, where a large fraction of cancellous bone is distributed, could be subjected to severe fracture-induced injuries. It is equally important to study the fracture behaviors in cancellous bone as in cortical bone. In literature, studies have been documented to investigate the mechanical properties and fracture behaviors of cancellous bone at either low [84] or high strain rates [53, 54, 56, 57, 116]. Under compressive loadings at large strains, most of the broken trabeculae (the microstructure element in a form of 'rod' and 'plate' in cancellous bone), in a form of splitting along axis and fracturing in the middle or end, were those orientated transversely to the loading direction [84]. At high strain rates (10/s-10^3/s), mechanical properties of cancellous bone, such as elastic modulus, yield and ultimate strength, and energy to failure were reported generally higher than at quasi-static strain rates [53, 54, 56, 57, 116]. Similarly as that for cortical bone, a transition in the strain-rate sensitivity of cancellous bone's mechanical behaviors was also found, which occurred in the range of intermediate strain rates (1/s-10/s) [56].

A complete investigation on fracture behavior in bone should cover the entire fracture process, including crack initiation and subsequent propagation until the ultimate failure of the specimen. The assessment of crack initiation has always been a difficult subject on dynamic fracture in bone. The complex stress state in the area in front of the crack tip during dynamic loadings and the intrigue microstructures in bone remarkably make it stand out from continuum fracture mechanics. Although with great significance, few investigations into dynamic fractures in either cortical bone or cancellous bone at microscopic length scales were available in the literature. Even for those studies conducted at microscopic levels at quasi-static loading rates [38, 42, 45, 73-84, 114], visualization of in-situ crack initiations was not provided and observations of fracture surfaces were only restricted to postmortem specimens. Despite some research efforts have been invested to obtain the real-time images of crack propagation in bone at macroscopic length scales [58, 89], none provides the in-situ observations of the entire fracture process in details, such as the onset of crack initiation and the paths taken by the crack for subsequent propagation. Such a research gap is primarily because of either the difficulty for visualization of microstructures in bone using the traditional optical imaging techniques or the limitations of those experimental apparatus that are not capable to load the material at constant high loading rates. To reveal the interactions between crack and bone microstructures at crack initiation and subsequent propagation, as well as

identifying the fracture toughening mechanisms, a high-speed synchrotron X-ray imaging technique was applied in this study.

4.3 Materials and methods

Pre-notched porcine cortical bone and cancellous bone specimens were prepared. X-ray tomography was performed to document the intact microstructures in the bone specimens before mechanical loading. A modified Kolsky compression bar was used to dynamically load the specimens and a high-speed synchrotron X-ray phase contrast imaging (PCI) set-up was applied to visualize the in-situ bone fracture behavior. Critical stress intensity factor was also determined to quantitatively understand the fracture initiation toughness in bone and to investigate the effect of different microstructures in crack resistance. In this section, specimen preparation and measuring methods together with each of those experimental set-ups used in this study are introduced.

4.3.1 Materials

Fresh bone used in this study was obtained from a 6-month-old Yorkshire and Duroc crossbred male swine raised by the Department of Animal Sciences, Purdue University right after it was slaughtered. Cortical bone was extracted from the cortices of humeral mid-diaphyses of the swine, while the cancellous bone was from the trabeculae bony tissue of the frontal skull. Specimens with thicknesses, B, of ~1-1.2 mm, widths, W, of ~4-4.2 mm and lengths, l, of ~18.9-21.5 mm were carefully prepared for both cortical bone and cancellous bone using a precision saw (IsoMet 1000; Buehler, IL, USA) cooled and lubricated with water at a low speed of 100 RPM. The cortical bone specimens were orientated with the length and width directions parallel and perpendicular to the long axis of the humerus, i.e., the osteonal growth direction, respectively. The cancellous bone specimens were orientated such that its length and width directions parallel to the symmetric and radial axes of the cranium, respectively. A notch with root radius r~200 μm and initial depth ρ~1.8 mm was introduced at the inner-layer edge to prepare single-edge notched bend specimens (SENB) using the same precision saw at low speed (100 RPM). More specifically, for cortical bone specimens, the notch (in the longitudinal-radial plane) was machined such that its direction was perpendicular to the long axis of osteons. For cancellous bone specimens, the notch was machined so that its direction was along the predominant trabecular direction. Specimens were not

pre-cracked as the fatigue cycles for pre-cracking would likely induce the toughening effects and bring more stress uncertainties in bone [58]. A total number of ten specimens, with five for each bone type, were prepared in this study. All the specimens were kept hydrated with 1X Phosphate Buffered Saline (PBS) throughout the entire sample preparation and transportation processes. Figure 4.1 shows the schematics of the two types of bone specimens used in this study.

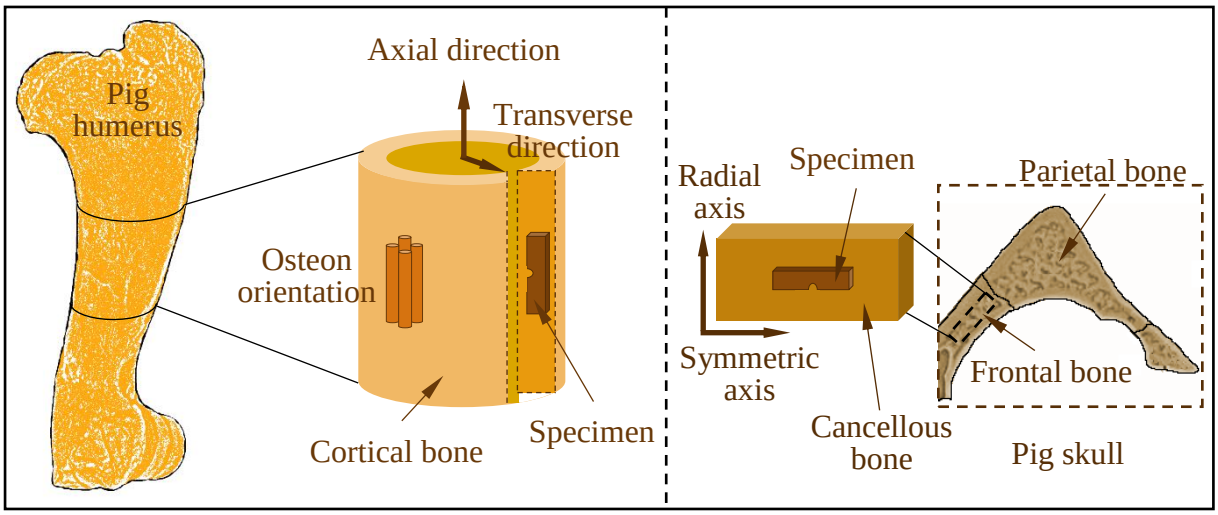

Figure 4.1 Schematics of the porcine bone specimen

4.3.2 Three-dimensional X-ray tomography

To record the initial interior microstructure of the bone specimen that is needed in the analysis of cracking and toughening mechanisms under dynamic loading, X-ray computed tomography (CT) was performed on the bone specimens prior to mechanical loading. Reconstructions of the through-the-thickness slices were then carried out using the projected X-ray images recorded at various angles. The synchrotron X-ray CT was performed on all specimens at beam line 2-BM at the Advanced Photon Source (APS), Argonne National Laboratory, Lemont, IL, USA. The specimens were mounted on a rotational stage where the monochromatic X-ray beam with energy 25 keV could propagate through and thus projected images of the specimens on a complementary metal-oxide-semiconductor (CMOS) detector (PCO; Dimax, Kelheim, Germany) of a high-speed camera after the X-ray was converted to visible light by a single-crystal scintillator [117]. 1500 projections over 180° rotation were taken on all the specimens, with a frame size of 2560 × 960 pixels, a voxel size of 1.3 μm, an exposure time of 100 ms per projection, and a frame rate of 13

s^{-1}. Figure 4.2 shows examples of reconstructed three-dimensional tomographic images of the cortical and cancellous bone specimens.

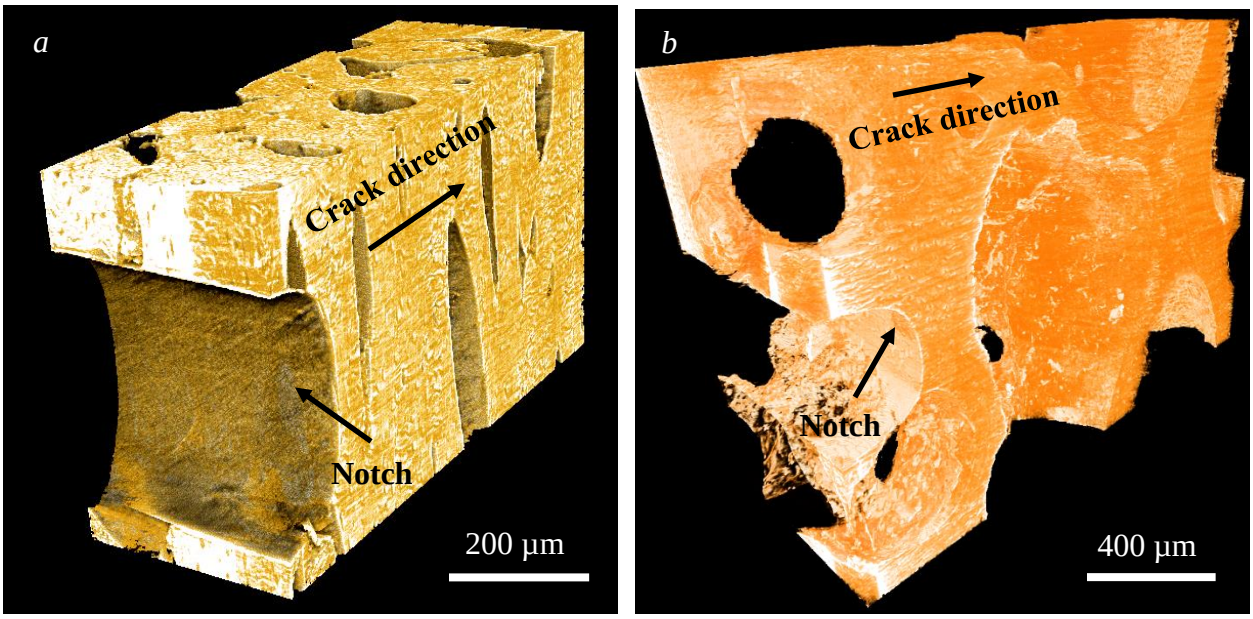

Figure 4.2 Examples of three-dimensional tomographic images for bone specimens (a) cortical bone (b) cancellous bone

4.3.3 Modified Kolsky compression bar

Kolsky bars have been widely used to characterize the mechanical properties of various materials at high strain rates (10^2/s-10^4/s) since its first introduction in 1949 [118]. A modified miniature Kolsky compression bar apparatus was used in this study to perform the three-point flexural experiments on bone specimens, as schematically shown in Fig. 4.3. Due to the limited space in the X-ray hutch at the beamline of APS 32 ID-B where the dynamic experiments were performed, the transmission bar was replaced with a fast response quartz load cell (Type 9212; Kisler, NY, USA), which was fixed on a solid backstop to ensure minimal load cell disturbance stimulated from the firing mechanism [119, 120]. The striker and incident bar are manufactured from a high-strength steel alloy (Vascomax C300 maraging steel) and they both are 12.7 mm in diameter. The lengths of the striker and incident bar are 305 mm and 1372 mm, respectively. In order to load the specimen with a three-point bending configuration, a two-point support steel fixture with a span (*S*) of 16 mm was connected to the end of the incident bar while the one point loading steel fixture was mounted on the load cell. This configuration allows the fracture process

to occur within the available X-ray window since the loading point is nearly stationary. A pair of semiconductor strain gauges mounted on the surface of the incident bar were connected in a half Wheatstone bridge configuration to measure both the incident and reflected stress waves. The output from the strain gauge/Wheatstone bridge assembly and load cell were amplified by a differential preamplifier and charger amplifier, respectively, and were recorded with an oscilloscope simultaneously. A smoothened rectangular stress pulse was created and shaped using a pulse shaper as the input pulse to achieve a constant loading speed on the specimen. In addition, a single loading device was used to remove the majority of the stress amplitude in the second and further reflected pulses from the incident bar to prevent multiple loadings on the specimens and ensure no overload occurs in the load cell.

For experiments on Kolsky bars, one-dimensional stress wave theory relates the velocity at sample end of the incident bar to the measured incident and reflected strain pulses as [101],

$$v(t) = C_B \left[\varepsilon_I(t) - \varepsilon_R(t) \right] \tag{4.1}$$

where $v(t)$ is the velocity at sample end of the incident bar, C_B is the elastic bar wave speed, $\varepsilon_I(t)$ and $\varepsilon_R(t)$ are the magnitudes of the measured incident and reflected strain pulses. The displacement $D(t)$ of incident bar end then is obtained by integration of the velocity,

$$D(t) = \int_0^t v(\tau)\, d\tau \tag{4.2}$$

4.3.4 Integration of synchrotron X-ray PCI and modified Kolsky bar

The high-speed synchrotron X-ray PCI was synchronized with the modified Kolsky bar to record the failure mechanisms in various materials under dynamic loadings [121-123]. Further details of the experimental method were described elsewhere [119, 120]. In this study, the modified Kolsky bar was used to introduce dynamic fractures and the high-speed synchrotron X-ray PCI was applied to image the fracture behaviors of bone, as schematically illustrated in Fig. 4.3.

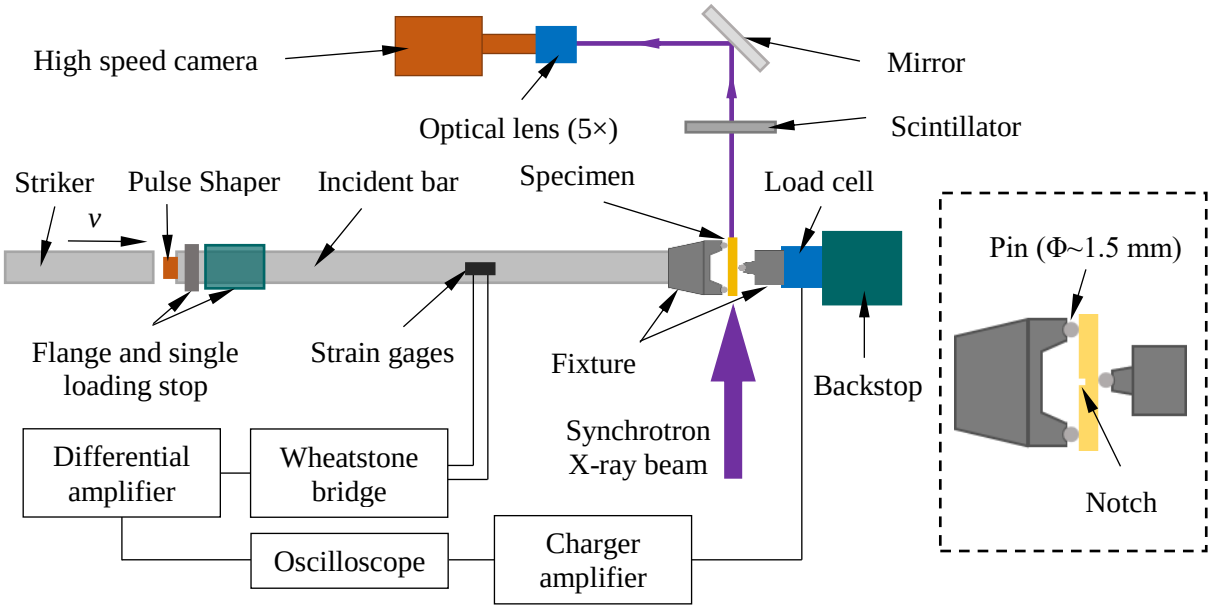

Figure 4.3 Schematic of the experimental set-up that combined a modified Kolsky bar with synchrotron X-ray PCI

X-ray PCI makes the use of the differences in the change of X-ray phases as they pass through the multiple-constituent composed sample to enhance the contrast in the resultant images. Another inherent advantage of using X-ray PCI is that the refraction and interference of highly coherent X-rays could result in variations of wave intensity so that visualization of the edges at the interfaces and cracks could be enhanced. This work principle grants the PCI technique ability to resolve structural variations and inhomogeneities in materials. In addition, X-ray PCI can effectively penetrate through low atomic number materials, thereby allowing the visualization of microstructure and microcrack propagation with high spatial resolution inside specimens rather than solely at the surface.

The high intensity, high temporal and spatial resolution X-ray PCI experiments were performed at the APS beamline 32 ID-B. The X-ray beam utilized a standard APS undulator A with a period and length of 2.4 m and 3.3 cm, respectively. The Kolsky bar was placed approximately 40 m downstream of the X-ray source and orientated 90° with respect to the beam pathline to expose the specimen to the X-ray beam. A white X-ray beam with its fundamental energy centered at 25 keV was employed in this study and its cross-section with a uniform magnification of X-ray was controlled to be 2.2 mm wide and 2 mm high. The X-ray wavelengths were converted to visible light via a single-crystal $Lu3Al5O12:Ce$ scintillator after it passed

through the specimen (Fig. 4.3). The visible light was reflected by a 45° mirror and magnified by a 5× microscope objective lens, eventually recorded by an ultra-high-speed camera. A Shimadzu Hyper Vision HPV-X2 camera was used to capture the visible light images at a frame rate of 5,000,000 frames per second (fps) for four of the cortical bone specimens and three of the cancellous bone specimens in this study, resulting in a temporal resolution of 200 ns for the images. A frame rate of 500,000 fps and 1,086,957 fps with a resultant temporal resolution of 2 μs and 0.92 μs were used for the other two cancellous bone specimens. A frame rate of 500,000 fps was used for one cortical bone specimen. The lower frame rate of 500,000 fps was used to capture the fracture events over a time period of an order of longer magnitude, whereas the 1,086,957 fps frame rate synchronizes with the X-ray pulse to produce a set of images with nearly even intensity. An output signal consisting of the timing pulses for each frame from the camera was also recorded by the oscilloscope for synchronizing the X-ray images with the measured loads and displacements. The spatial resolution of the imaging was estimated to be 6.4 μm/pixel and the frame size was 400 pixels in width and 250 pixels in height.

4.3.5 Dynamic fracture toughness measurements

The three-point bending experiments on Kolsky bar presented in this study were designed and performed such that the dynamic fracture toughness measurements on SENB bone specimens were in general accordance with ASTM standard E1820 [74]. We here evaluate the dynamic mode I fracture toughness of bone specimen in terms of the crack-initiation stress intensity factor K_{Ic} based on the initial crack observed in X-ray images. Its value for a SENB specimen was calculated using the equation [124]:

$$K_{\mathrm{Ic}} = \left[\frac{P_i S}{B W^{3/2}} \right] f\left(a_i / W\right) \tag{4.3}$$

where P_i is the applied load when the micro-crack initiated, S is the span of the three-point bending experiments and $f\left(a_i / W\right)$ is a function depending on the sample's geometry and initial crack length, a_i, to specimen width ratio. The initial crack length a_i was estimated as the projected length in the nominal mode-I plane of the tortuous crack in the synchronized in-situ X-ray images. The function $f\left(a_i / W\right)$ was calculated using the equation [124]:

$$f\left(\frac{a_i}{W}\right)=\frac{3\left(\frac{a_i}{W}\right)^{1/2}\left[1.99-\left(\frac{a_i}{W}\right)\left(1-\frac{a_i}{W}\right)\left(2.15-3.93\left(\frac{a_i}{W}\right)+2.7\left(\frac{a_i}{W}\right)^2\right)\right]}{2\left(1+2\frac{a_i}{W}\right)\left(1-\frac{a_i}{W}\right)^{3/2}} \tag{4.4}$$

For the dynamic three-point bending experiments performed to measure the fracture toughness of bone in this study, qualifications for valid K_{Ic} were met for all the bone specimens, *i.e.*, b (=W-a_0), $B > 2.5(K/\sigma_{YS})^2$, as specified by ASTM Standard E1820, where σ_{YS} is the 0.2 % offset dynamic yield strength in tension. Due to the absence of dynamic σ_{YS} values in literature, the σ_{ult} for pig bone under dynamic tensile loading (300/s), which was determined previously to be 50 MPa [125], was used in this study to judge whether the values of fracture toughness were valid. The generated errors by using the dynamic σ_{ult} instead of dynamic σ_{YS} were considered to be small since the bone behaves as a brittle material especially under dynamic loadings.

Images showing the fracture surfaces and crack path profiles of the postmortem specimens were obtained using a scanning electron microscope (SEM) (Quanta FET, Thermo Fisher Scientific, MA, USA) operated at 5 kV accelerating voltage at high vacuum and low vacuum at a pressure of 60 Pa in the secondary electron mode.

4.3.6 Statistics

The differences in location of crack initiation, the incipient crack's propagation direction and fracture toughness between the cortical bone and cancellous bone were tested using the Welch corrected *t*-Tests assuming different variance. Prior to *t*-Tests, Shapiro-Wilk (S-W) tests were performed to check the normality of all those data. *p*-Values larger than 0.05 were considered normally distributed for S-W tests while *p*-values less than 0.05 were regarded as statistically significant for *t*-Tests in this study.

4.4 Experimental Results

4.4.1 Microstructures in bone from X-ray tomography

As shown in Fig. 4.2, the difference of the microstructures between the cortical bone and cancellous bone is evident in Fig. 4.2a and 4.2b, where the structure of functional unit-osteon composited with matrix are observed in dense cortical bone specimens while the cancellous bone specimen is much more porous and mainly consists of rod and plate-like structures (trabeculae).

Figure 4.2 provides further evidence that the orientation of osteon is aligned perpendicular to notch's normal direction, while the predominant direction of the functional unit-trabeculae is observed along the notch's direction in the cancellous bone specimen. The maximum diameter of the osteon in the cortical specimen is measured to be ~220 μm. The wall thickness of trabeculae measured from the tomographic images for the cancellous bone specimen is in the range of 110 μm-280 μm.

4.4.2 In situ dynamic fracture imaging

A dynamic three-point flexural load was applied on the bone specimens using the modified Kolsky bar facility with a loading velocity of 6.1 ± 0.1 m/s. The entire fracture process was observed using the high-speed X-ray PCI system as described in section 2.4. The dynamic three-point bending experiments under identical testing conditions were performed repeatedly on ten specimens within the available beam time, with five for each of the cortical bone and cancellous bone. The recorded high-speed X-ray images from two representative experiments for the cortical bone and cancellous bone are cropped and provided in Figs. 4.4 and 4.5, respectively. Not surprisingly, all the cracks were initiated at the surface of notch roots. However, instead of on the symmetrical axis where maximum normal stress is expected, the location of the crack initiation was on a plane with an angle to the symmetrical axis. Multiple reasons could lead to this phenomenon, including the complex stress state in the area close to the notch surface, microstructures of bone material and specimens geometry. For both these two representative cortical bone and cancellous bone specimens, subsequent to the point of incipient fracture, the crack propagated straightly for a short distance in the same direction until an occurrence of crack bifurcation or the crack began to interact with the microstructures in bone. The entire crack paths were observed to vary from cortical bone to cancellous bone and such variations can mainly be attributed to the large differences in their microstructures and the relative orientations of their initial crack paths. During the crack propagation, two major types of mechanisms were observed: ligament bridging in the wake of crack alone or combined with fracture deflections at the osteon cement lines, although each of them plays a different role in affecting the crack propagation in the two types of bone.

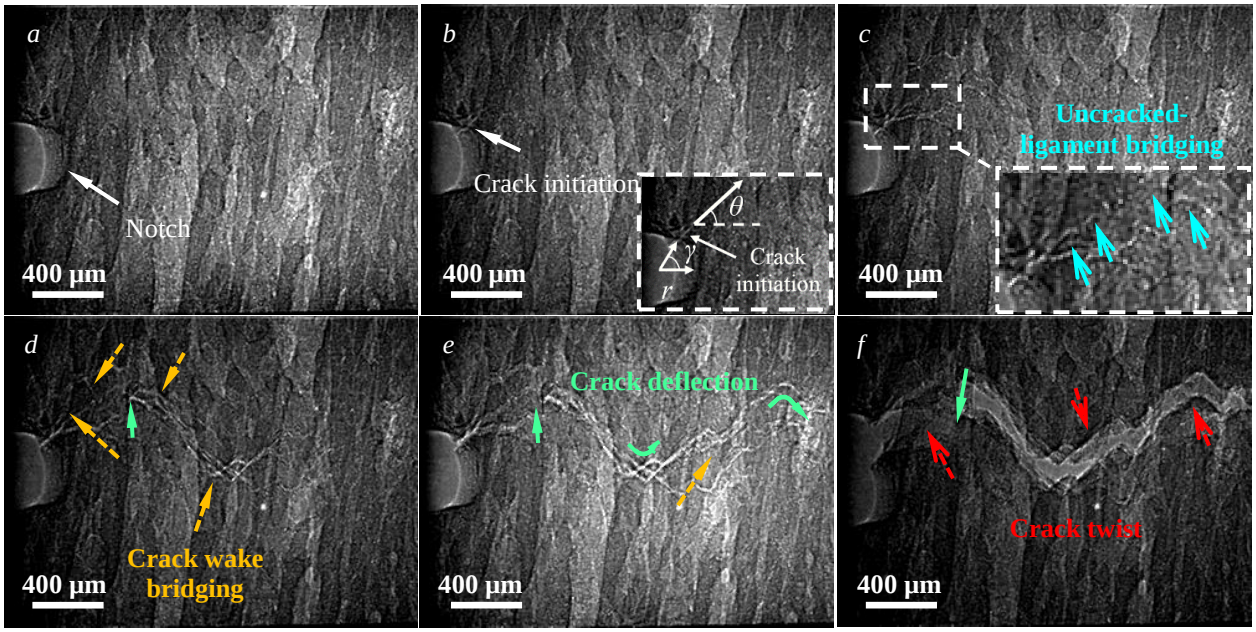

Figure 4.4 High-speed X-ray images of a cortical bone specimen (*a*) *t*=0 μs. (*b*) *t*=23.8 μs. (*c*) *t*=25.6 μs. (*d*) *t*=27.8 μs. (*e*) *t*=29.4 μs. (*f*) *t*=42.2 μs. The crack initiation is indicated in *b*. The cane arrows (open arrows with solid dashes) indicate the uncracked ligament bridging (in *c*). The yellow arrows (solid arrows with dot dashes) indicate the collagen bridging in crack wake (in *d*, *e*). The green arrows (solid arrows with solid dashes) indicate the ~90° crack flections (in *d*, *e*, *f*) and the red arrows (open arrow with dot dashes) indicate the out-of-plane crack twists (in *f*)

The microstructures in cortical bone were shown clearly in Fig. 4.4. The longitudinal dark "strip" featured the Haversian system (osteon) and the light area between the Haversian system was the interstitial lamella (matrix). The initial notch was on the left edge of the images and its initial normal direction was perpendicular to the osteon (Fig. 4.4). The crack was initiated at the radius root surface of the notch (Fig. 4.4b) with an angle γ of 52° to the symmetry axis. The angle between the subsequent crack propagation direction and horizontal symmetry axis was denoted by θ and measured to be 43°, as shown in Fig. 4.4b. The crack then propagated along the direction of θ for a short distance and began to propagate approximately in the horizontal direction. It then penetrated through some osteons and propagated along the horizontal direction for as long as ~406 μm until it deflected ~45° (Fig. 4.4d, e) as it encountered an osteon cement line. As the crack continued to propagate, it deflected ~90° as it encountered another osteon cement line and traveled along a direction inclined ~45° to the horizontal direction, showing an overall zigzag crack path. Further crack propagation evolved more in-plane crack deflections and out-of-plane crack twists, as shown in Fig. 4.4e, f, which generated comparatively tortuous crack paths, rough fracture

surface and in turn resulted in potent fracture toughening mechanisms. In addition to crack deflections and twists, fracture toughening mechanisms such as collagen bridging in the crack wake and uncracked-ligament bridging (Fig. 4.4c, e), commonly shown in the case where the crack growing was parallel to the osteon direction, were also observed in the specimen

The microstructures, crack paths and consequent mechanisms of toughening were quite different in cancellous bone. Figure 4.5 presents the high-speed X-ray images for a cancellous bone specimen. The lattice-like structures were shown clearly in the images: dark rod and plates represented the trabeculae and the bright areas enclosed by trabeculae denoted the pores. The crack was initiated at the notch root that located at the left side in the images as well and the angle γ and θ, with the same definition as in cortical bone specimen (Fig. 4.4*b*), were measured to be 37° and 24°, respectively. The crack then propagated in and penetrated through the trabeculae where it initiated in a nearly straight path along that direction for a distance of (Fig. 4.5) ~166 μm until it reached the edge of trabeculae. Afterward, the crack penetrated through the pores in a highly curved path along a trabecula until it reached and broke one trabecula. It may be surprising that the crack then started to travel in a path by penetrating through trabeculae, displaying an overall wavy crack path. Comparing with the crack in cortical bone, mild deflections over the entire crack path were observed as the crack propagated through the whole structure and broke those trabeculae orientated in the transverse direction in the middle or at end of the trabeculae. Uncracked ligament bridging and crack twists (Fig. 4.5*d, f*) also took place during the crack propagation as fracture toughening mechanisms.

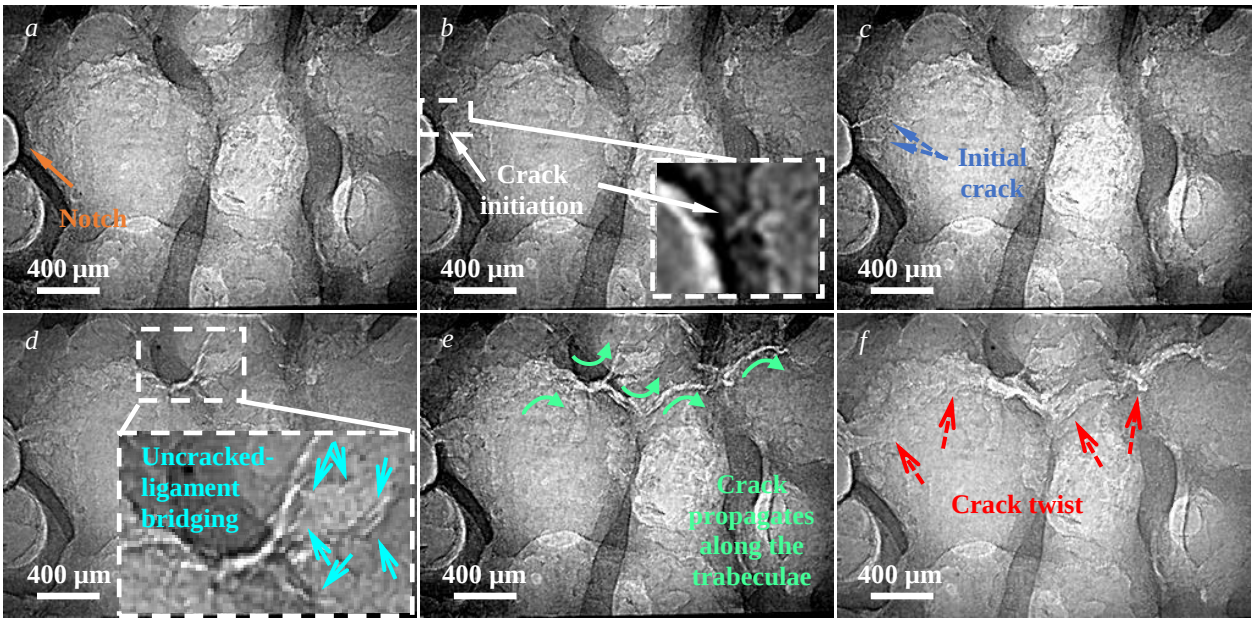

Figure 4.5 High-speed X-ray images of a cancellous bone specimen (*a*) *t*=0 μs. (*b*) *t*=21.8 μs. (*c*) *t*=24.2 μs. (*d*) *t*=33 μs. (*e*) *t*=38.6 μs. (*f*) *t*=50 μs. The definitions of the color and types of arrow and dash are same as in Fig. 4.4

Table 4.1 Geometry parameters for onset location of crack initiation and the direction of its subsequent propagation in bone

Angle	Bone type	No. 1	No. 2	No. 3	No. 4	No. 5	Average	SD	*t*-Test
γ	Cortical bone	52°	-39°	66°	-51°	-48°	51°	9.7°	A
	Cancellous bone	-45°	-50°	37°	45°	44°	44°	4.7°	A
θ	Cortical bone	43°	-48°	45°	-51°	-63°	50°	7.9°	-
	Cancellous bone	-25°	-24°	24°	0°	0°	15°	13°	-

The initiation locations of major fractures and the subsequent fracture propagation directions in terms of angle γ and θ, as defined earlier in Fig. 4.4, for all the tested 10 specimens were measured and listed in Table 4.1. As shown in Table 4.1, all the data was normally distributed except θ for cancellous bone. It should be noted that, in Table 4.1, a positive value of angle denotes counter-clockwise direction while a negative value denotes clockwise direction and *t*-Test of two

groups with the same letter denotes an insignificant difference. The difference in γ between the cortical bone and cancellous bone was statistically insignificant.

4.4.3 Fracture toughness measurements

The corresponding synchronized load-displacement curves for the cortical bone and cancellous bone samples (shown in Figs. 4.4 and 4.5) were plotted in Fig. 4.6*a* and 4.6*b*, respectively. The peak loads were 24.1 N and 8.7 N and occurred at 26.6 μs and 28.8 μs for the cortical bone and cancellous bone specimen, respectively. The points corresponding to X-ray images in Figs. 4.4 and 4.5 on the load-displacement curves were also denoted in Fig. 4.6 for reference. Using the load-displacement curves and synchronized in-situ X-ray images of the entire fracture process, the critical stress intensity factors of the bone specimens were calculated by Eq. (4.3), where the loads at crack initiations were used. The resultant values of K_{Ic} for cortical bone and cancellous bone were listed in Table 4.2, where the *p*-values for S-W normality tests and Welch corrected *t*-tests were also provided, indicating a statistically significant difference in fracture toughness between the two types of bone.

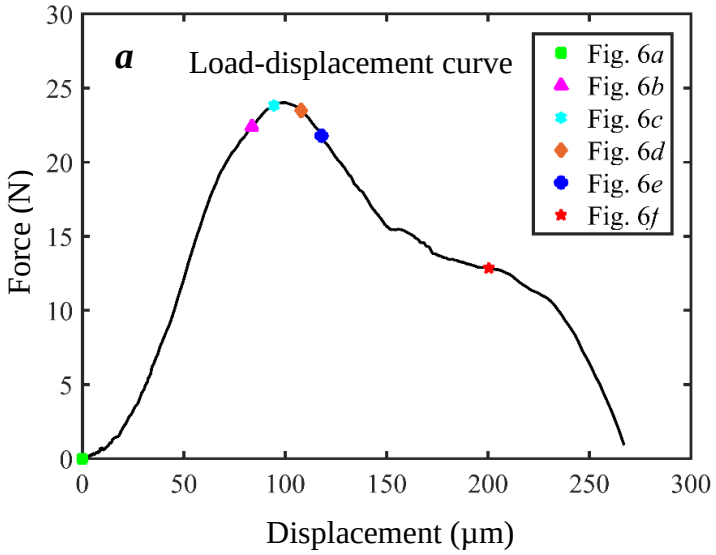

Figure 4.6 Load-displacement curves for the bone specimens with timing points indicating the synchronized X-ray images in Figs. 4.4 and 4.5 (a) cortical bone specimen (b) cancellous bone specimen

Figure 4.6 continued

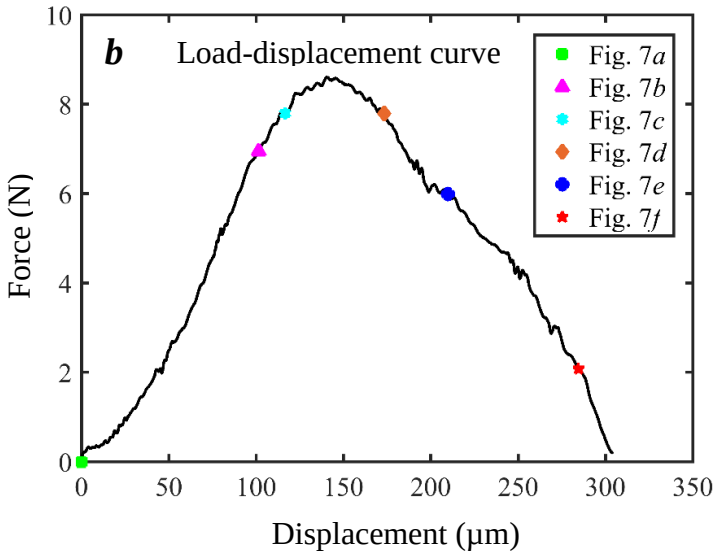

Table 4.2 Fracture toughness of cortical bone and cancellous bone at dynamic loading rate

Bone type	Stress intensity, K_{Ic} (SD)	S-W test	Welch corrected t-Test
Cortical bone	1.61 MPa·√m (0.38)	0.92	6.9×10^{-4}
Cancellous bone	0.38 MPa·√m (0.19)	0.96	

4.5 Discussions

In this study, the crack initiated on the notch root surfaces for all the samples with some degrees of variations in the locations. Interestingly, as shown in Table 4.1, the γ was found to be comparatively consistent and statistically independent of the bone type. This indicates that the locations of crack initiation presumably mainly depend on the mechanical aspects, such as stress state, instead of microstructures in bone. In terms of initial crack propagation direction, the value of θ was consistent for cortical bone while it varied significantly for cancellous bone, with three specimens for ~24° while two for 0°. Such variations could be due to the difference in stress states and the microstructures in the area close to the locations of crack initiation. However, by further examining the locations of the notch in cancellous bone, we found that the case for 0° was that the notch root surfaces were mainly in pores, whereas the cases for ~24° were that notches were on the trabeculae. Furthermore, the values of γ and θ, i.e., the shape of the trajectories at incipient

crack for cortical bone, agreed well with the crack trajectories of a notched sample under tensile loading that inclined ~20°-40° to the symmetry axis predicted using the minimum strain energy density [126], indicating that a mixture of mode I and mode II fractures in the area close to the crack tip. It should be noted that the independence of crack initiation locations on bone type is based on the results with a small sample size (<10) here, future study may be needed to further confirm it.

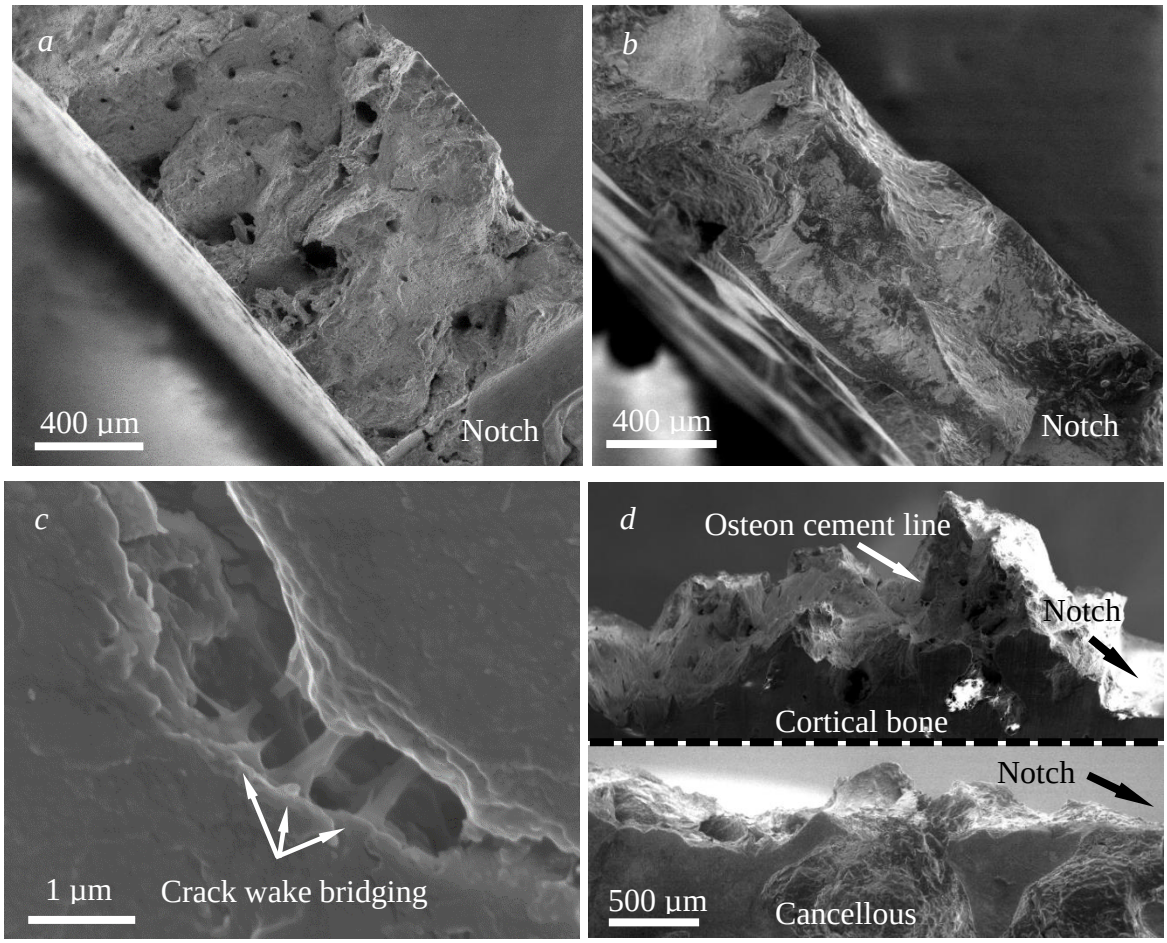

Figure 4.7 SEM images showing the fracture surfaces and crack paths of the bone specimens (*a*) top view of fracture surface of cortical bone (*b*) top view of fracture surface of cancellous bone (*c*) a closer examination at higher magnification of the crack wake bridging of the cortical bone (*d*) corresponding front view of the cortical bone and cancellous bone showing a comparison between their crack paths

As has been reported previously that, in cortical bone, cracks tended to deflect and twist at the osteons during its propagation and the extent of such fracture deflection effectively diminished at

comparatively higher strain rate (0.1/s), which was evidenced with the observations of relatively smoother fracture surfaces in the postmortem SEM images [74]. The presented SEM images in Fig. 4.7*a* of the cortical bone in our study reaffirmed that crack path was less torturous in dynamic fractures when compared with quasi-static loading rate (10^{-5}/s) [74]. However, in both of our in situ X-ray and SEM images, there were still some extent of crack deflections that were observed at the cement-line boundaries of the osteons. The implication of such result is that, despite the osteon-matrix structure ahead of growing crack displaying less plasticity by deflecting crack trajectories with limited extent, the higher mineralized osteons still contributes to fracture toughening even under dynamic loading. Other fracture toughening mechanisms, such as uncracked ligament bridging, crack wake bridging by fibrils were also seen in the X-ray images and such evidence was further displayed in Fig. 4.7*c*.

The crack resistance in cancellous bone, on the other hand, functions in significantly different mechanisms because of the different trabecular microstructure in cancellous bone. As shown in Fig. 4.5, the crack took a straighter and smoother path through the overall bone structures and broke the trabeculae mostly in middle or at ends of the connections to the 'neighbor' trabeculae, and such less tortuous crack path was also verified by the SEM images shown in Fig. 4.7b and 4.7d. Before the crack reached and further propagated along the trabeculae (Fig. 4.5e and 4.5f), the crack took a comparatively straighter path and few crack deflections and twists were observed (Fig. 4.5c and 4.5d). In addition to fracture deflections and twists, uncracked ligament bridging was also observed in Fig. 4.5*d*, although the contributions to crack resistance from all those toughening mechanisms could be significantly diminished under dynamic loadings. The crack propagation speed for each cortical bone (Co) and cancellous bone (Ca) specimen was calculated using the high-speed X-ray images and plotted against the crack extension for all the ten specimens in Fig. 4.8. Overall, the crack velocity can depend on material properties, specimen geometries, loading conditions, etc. However, provided that the major different factor here is the type of bone material, a comparison of wave velocity between the cortical and cancellous bone could shed a light on the influence of their different microstructures on crack velocity. As illustrated in Fig. 4.8, both types of specimens' crack velocities were dependent on crack extension, while the crack propagated at a lower speed in cancellous bone. Theoretical studies showed that crack propagating with a lower speed relates a greater fraction of strain energy for volume change of the area in front of crack tip [126] and thus facilitates the crack propagation with fewer bifurcations, resulting in a

smooth crack surface. This could be further verified by the less tortuous crack surfaces observed in high-speed X-ray images (Figs. 4.4 and 4.5) and SEM images (Fig. 4.7) of cancellous bone.

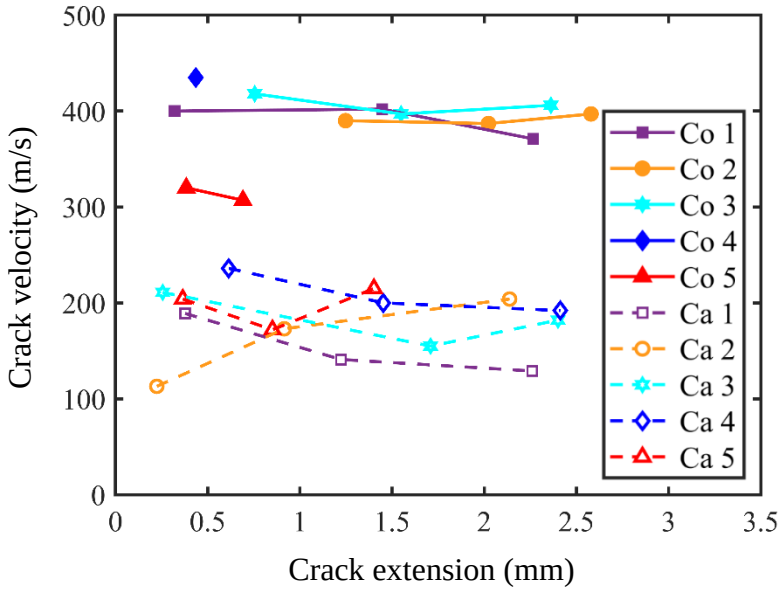

Figure 4.8 Crack velocity-extension curve for cortical bone and cancellous bone (Co: Cortical bone specimen, Ca: Cancellous bone specimen)

The crack-initiation toughness, K_{Ic}, of cortical bone was 1.61 MPa/√m (SD 0.38) and roughly three times higher than cancellous bone, which succinctly showed a higher resistance of cortical bone to fracture initiation under dynamic loadings. It is worth noting that Eq. (4.3) for fracture toughness is based on linear elastic fracture mechanics. The real situations in the bone specimens were much more complicated owing to the dynamic loading conditions and mixed mode I and II fractures [115]. The reported K_{Ic} in our study is determined by simply assuming there is only mode I fracture and all the bone specimens, as a whole at macroscopic length scales, are regarded as continuum. Crack-initiation toughness, K_{Ic}, of human cortical bone, rat cortical bone and bovine cortical bone measured in the same transverse orientation (transverse to osteon direction) at quasi-static loading rates were reported previously to be 2.03 MPa/√m (SD 0.19), 2.16 MPa/√m (SD 0.67) and 5.7 MPa/√m (SD 1.4), respectively [127-129]. The differences could be the results of their specimens being from different species and being from different anatomical locations. The lower fracture toughness in this study is presumably a result of high loading rates as reported in [33, 51, 52, 58, 59, 74, 89] that toughness decreased as the loading rate increased. Our crack-

initiation toughness of porcine cancellous bone was in the range of the results for human cancellous bone and equine cancellous bone measured on SENB specimens in the same longitudinal direction at quasi-static loading rates, where K_{max} values of ~0.1-0.6 MPa/√m were reported [130]. The radiation exposure, with a dose of ~16 kGy for cortical bone and ~18 kGy for cancellous bone, due to X-ray computed tomography could also affect the mechanical behaviors of bone specimens in our study. However, such effect of radiation at low dose (<30 kGy) is still controversial in literature, with a decreasing ratio of ~22% for fracture toughness at a dose of 27.5 kGy reported in [62] while no significant difference in mechanical properties, such as strength, strain at failure and force at failure were claimed for radiation at 20-25 kGy in [63]. It also should be noted that the fracture toughness of porcine bones provided in our study and other bones reported previously in literature [30, 51, 58, 76, 77, 82, 89, 115, 127, 128, 130] could be higher than their intrinsic fracture toughness as the cracks initiated from notches instead of pre-cracks.

4.6 Conclusions

In this study, the in situ visualization of crack initiation and propagation in hydrated porcine cortical bone and cancellous bone under dynamic loadings were performed. Based on the experimental results, we conclude that:

1. The experimental apparatus that combining synchrotron X-ray PCI and modified Kolsky bar facilitated us to investigate the fracture behaviors in bone under dynamic loading. Synchrotron X-ray tomography on each specimen helped us to gain the basic knowledge of the initial microstructures in the specimen before mechanical loading.
2. All the cracks initiated on the notch roots. The locations of crack initiation were statistically independent of the type of bone and the direction of subsequent crack propagation was found to be consistent among cortical-bone specimens while varied remarkably for cancellous bone. Crack velocity was also measured and a dependence on both bone type and crack extension was observed.
3. During dynamic fracture, multiple fracture toughness mechanisms, such as crack deflection, twist and uncracked ligament bridging were observed for the cortical bone or cancellous bone in the high-speed X-ray images. An overall zig-zag facture path was observed in the cortical bone specimen while a wavy crack path with mild crack deflections occurred in cancellous bone. Such observation was further verified by a more tortuous crack path of cortical bone in postmortem SEM images when compared with cancellous bone.

4. Fracture toughness in terms of the stress intensity factor at crack initiation was calculated and the results showed a factor of 4 in fracture toughness of cortical bone than cancellous bone, which further verified the effects of a more tortuous crack path in cortical bone in X-ray images and SEM images.

CHAPTER 5. REAL-TIME VISUALIZATION OF DYNAMIC FRACTURES IN PORCINE BONES AND THE LOADING-RATE EFFECT ON THEIR FRACTURE TOUGHNESS

Adapted from:
X. Zhai, J. Gao, Y. Nie, Z. Guo, N. Kedir, B. Claus, T. Sun, K. Fezzaa, X. Xiao, W.W. Chen. Real-time visualization of dynamic fractures in porcine bones and the loading-rate effect on their fracture toughness, Journal of the Mechanics and Physics of Solids. 131 (2019), 358-371.

5.1 Abstract

We visualized, in real time, the dynamic fracture behaviors in porcine cortical bone from humerus and porcine trabecular bone from nasal bone at a high loading rate using high-speed synchrotron X-ray phase-contrast imaging (PCI). Dynamic three-point bending loading was applied on notched bone specimens by a modified Kolsky compression bar and images of the entire fracture events were recorded with an ultra-high-speed camera. Experiments at a quasi-static loading rate on material testing system (MTS) were also performed to identify the loading-rate effects on the fracture toughness of the two types of bone. Three-dimensional synchrotron X-ray computed tomography was conducted to examine the initial microstructures in the bone specimens before mechanical loading. At the dynamic loading rate, the onset locations of crack initiation were found to be independent from the bone types. The deleterious effect of dynamic loading rate on bone's fracture toughness was verified in this study and the crack was found to propagate at higher speeds in cortical bone than in trabecular bone. In a comparison of the observed more torturous crack paths at the quasi-static loading rate, cracks in dynamically loaded bone specimens generally followed the paths with less in-plane deflections and out-of-plane twists. However, our experimental results also indicated that, although the extent was diminished at dynamic loading rate, the crack deflections at osteon cement lines still played a role as a major toughening mechanism to dynamic fractures in transversely orientated cortical bone.

5.2 Introduction

Bone, as an extremely intriguing and complex biological system, is primarily responsible to support the body and protect the inner vulnerable soft tissues. By manipulating integrations of minerals and collagenous proteins into hierarchical architectures in multiple length levels (ranging

from nano to sub-macro scales), bone is surprisingly one of the hardest yet lightweight materials built in nature [1, 2]. Among those fundamental properties of bone, one with tremendous significance is its toughness or more specifically its resistance to cracking. Cracks in bone not only occur at quasi-static loading rate but also are more regularly associated with dynamic loading conditions. For example, measurements of in vivo loading rates in bone suggested strain rates of ~0.007-0.02/s during walking or running [7-9], while a strain rate as high as ~25 /s for impacts [10]. Therefore, studying bone's fracture behaviors under both quasi-static and dynamic loadings is important to predict the fracture risk and hence avoid its occurrence.

It is until recently that the fracture toughness of cortical bone, a denser bone tissue that distributed mostly at the outer layer of skulls and long bones, have begun to be investigated quantitatively with respect to its microstructures [37-39, 42, 45, 73-82]. At quasi-static loading rates, the major toughening mechanisms were found to be varied in different loading directions because of the bone's anisotropy, as the crack deflections at osteon cement lines played an important role under transverse loadings while crack-ligament bridging in the crack wake is more prominent to inhibit further cracking when crack grows along the osteons [42, 76, 83, 131-133]. Whereas the fracture toughness of most structural materials increases with increasing mode-mixity (the relative amount of shear to tensile loading), experimental studies showed a remarkable decrease in fracture toughness in transverse aligned cortical bone as the mode-mixity increased [51]. Bone is not only anisotropic but also a viscoelastic material: its mechanical behaviors depend on loading rate significantly. Previous studies in macroscopic scales showed that, when loading rate increased from quasi-static to dynamic, a transition from quasi-ductile to brittle fracture took place in bone [33, 52, 58, 59, 74, 89], as the fracture toughness was largely reduced and a typical less tortuous crack surface was observed in postmortem specimen [30, 49, 51, 115]. A numerical study found that the initiation fracture toughness of bone decreased gradually as the strain rate increased from quasi-static to dynamic, while the propagation fracture toughness was only significantly sensitive to quasi-static strain rate (up to 1/s) [49]. The fracture mode in bone, determined by the crack propagation direction (e.g., perpendicular to notch direction for mode I fracture and 45° for mixed mode I and II fractures), was found to be more complex under dynamic loading, with a mode II dominant fracture in bone under quasi-static loading while a mixed mode of both mode I and II fractures at dynamic loading rates [115].

Another common bone fracture occurred commonly in impact events, such as motorcycle accidents and physical confrontations during sports, are fractures in facial bones, which can be accompanied by fatal brain injuries and thus become a potential cause of death [64]. Facial bones mainly consist of trabecular bone and they possess ‘lattice’ like bony tissue and are more porous than cortical bone. The material and mechanical properties of trabecular bone from different anatomical locations, such as skull, long bones and facial bones can be largely varied. Although, in literature, the trabecular bone from skull or long bones are largely studied [54, 56, 57, 84, 116, 130], it is perhaps surprising that there are almost no corresponding works in literature to evaluate the fracture behaviors of facial bone at micrometer length scales quasi-statically, not even to mention dynamically. At macroscopic levels, blunt impact induced fractures of various human facial skull bones, including mandible [67, 68], nasal [64, 65] and maxilla bones [64, 66] were investigated with respect to their tolerance to fractures (critical forces resulting in fractures). In their experiments, the whole human head was mounted on rigid support, which in turn was connected to load cell to measure the impact force during dynamic loading [64-66, 68]. In terms of human mandible bone, there was a large variation in the measured fracture tolerances (critical forces to fractures), with a value in the range of 2500 to 3000 N reported in [67] while a value of 5270 (± 930) N reported in [68]. The tolerance of human nasal bone and maxilla bone under blunt impact were also determined previously, with an applied force in the range of ~450-850 N and ~970-1200 N corresponding to a 50% risk of fracture was reported for nasal bone [65] and maxilla bone [66], respectively. The stiffness of both human nasal bone and maxilla bone under blunt impacts were evaluated previously to be 261 (SD, 217) N/mm and 360 (SD, 142) N/mm [64].

As seen above, the majority of those research efforts invested on fracture behaviors of cortical bone and trabecular bone in literature were either focused on macroscopic length scales or limited to quasi-static loading rates. In addition, the trabecular bone studied previously were mostly from the cancellous bony tissue in skull or vertebra. Consequently, in this study, we focused on in-situ visualization of the entire dynamic fracture processes in porcine cortical bone and trabecular bone that extracted from nasal bone and the effect of loading rate on their toughness.

5.3 Materials and methods

Single edge notched bend (SENB) porcine cortical bone and trabecular bone specimens were prepared for the three-point bending experiments at both quasi-static and dynamic loading rates.

Ultra-fast synchrotron X-ray tomography was performed to help understand the microstructures in bone before mechanical loading. The dynamic three-point flexural loading was introduced using a modified Kolsky compression bar and the entire in-situ fracture event in bone was documented using the synchrotron X-ray PCI technique. Quasi-static experiments were performed on a material testing system (MTS) for comparison with those under dynamic loading. Fracture initiation toughness was calculated in terms of the critical stress intensity factor for mode-I fracture. Scanning electronic microscopes (SEM) were used to obtain the images of fracture surfaces and crack path profiles in postmortem specimens. The specimen preparation and all those experimental measuring methods mentioned above are introduced separately in this section.

5.3.1 Materials

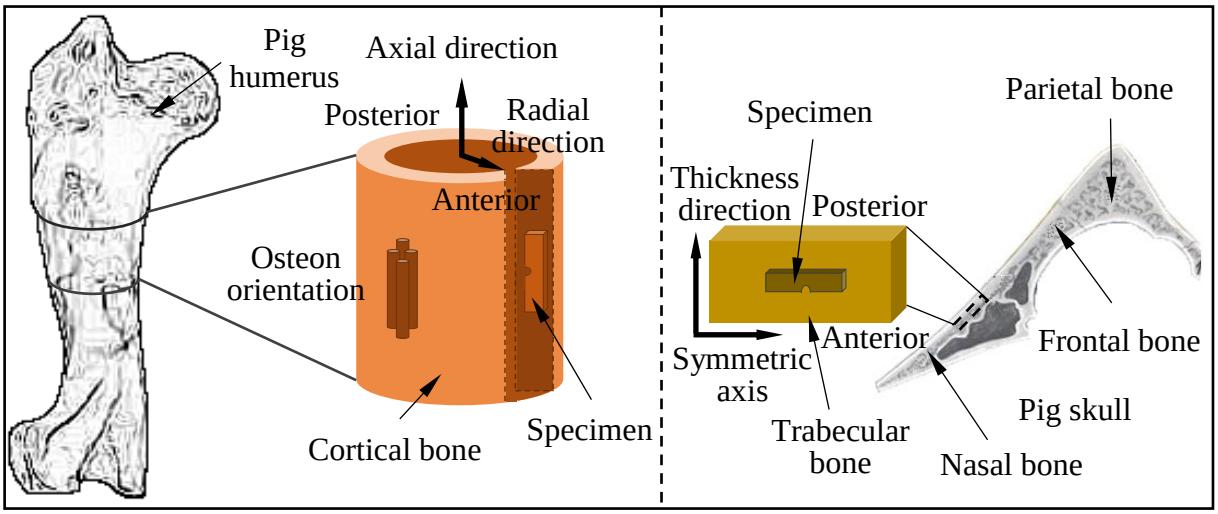

Figure 5.1 Schematic of the bone specimen

In this study, fresh porcine bone was collected from a 6-month-old Yorkshire and Duroc cross-bread male swine raised by the Department of Animal Sciences, Purdue University right after it was slaughtered and was kept frozen immediately at a temperature of -20 °C. The bone was thawed in room temperature one week prior to the experiments. Porcine cortical bone was extracted from the medial cortices of humeral mid-diaphyses of the swine and trabecular bone was extracted from the nasal skull bone. The specimens were cut from the entire cross-section (anterior to posterior) of the bony tissue using a precision saw (IsoMet 1000; Buehler, IL, USA) cooled and lubricated with water at low speed in between 100-150 RPM. All the prepared cortical bone and trabecular bone specimens have thicknesses, B, of ~1-1.2 mm, widths, W, of ~4.0-4.2 mm and lengths, l, of

~ 18.9-21.5 mm. The cortical bone specimens were orientated with its osteon growth direction parallel to the length direction. The trabecular bone specimens were prepared such that the symmetric axis of porcine nasal skull bone was parallel to the length direction. A notch with root radius, r~180 μm and initial depth, ρ~1.4-1.6 mm was introduced to prepare SENB specimens using the same precision saw at low speed (100 RPM). The notch in the cortical bone specimen was machined such that its normal direction was perpendicular to the long axis of osteons (in the longitudinal-radial plane). All the specimens were not pre-crakced as the pre-cracking process would probably induce the toughening effects and bring more stress uncertainties before mechanical characterization [58]. Ten specimens for each of the cortical bone and trabecular bone were prepared, with five specimens selected randomly for dynamic or quasi-static experiments for the two types of bone. Phosphate Buffered Saline (PBS) was used to keep the specimens hydrated during the entire sample preparation and transportation process. Figure 5.1 shows the schematics of the two types of specimens used in this study.

5.3.2 Three-dimensional synchrotron X-ray computed tomography

The interior microstructure of the bone specimen was examined by three-dimensional synchrotron X-ray computed tomography before mechanical loading. The X-ray tomography was performed on one representative specimen for both the trabecular bone and cortical bone at beam line 2-BM at the Advanced Photon Source (APS), Argonne National Laboratory, Lemont, IL, USA. The specimens were mounted on a rotational stage and a monochromatic X-ray beam with an energy of 40 keV was used in this study. A single-crystal scintillator was used to convert X-ray to visible light after it propagated through the specimens. The images of the specimens were magnified by a 5× microscope objective lens and projected on a complementary metal-oxide-semiconductor (CMOS) detector (PCO; Dimax, Kelheim, Germany) of a high-speed camera [117]. Reconstruction using a technique of 1500 projections over 180° rotation was performed on the bone specimens. The synchrotron X-ray tomography has a frame size of 2560 × 960 pixels, a voxel size of 1.3 μm, exposure time of 100 ms per projection and frame rate of 13 s^{-1}.

5.3.3 Integrated modified Kolsky compression bar and synchrotron X-ray PCI

The dynamic three-point bending experiments on bone specimens were performed on a modified Kolsky compression bar apparatus (Fig. 5.2). The transmission bar was replaced with a

low impedance fast response quartz load cell (Type 9212; Kisler, NY, USA) because of the limited space inside the X-ray hutch at APS 32 ID-B. The striker and incident bar are manufactured from a high-strength steel alloy (Vascomax C300 maraging steel) and they both are 12.7 mm in diameter. The striker has a length of 305 mm and the length of the incident bar is 1372 mm. A two-point support steel fixture with a span (*S*) of 16 mm was connected to the incident bar and the one-point loading steel fixture was mounted on the load cell, which was connected to a backstop to minimize signal disturbance [119, 120]. A pair of semiconductor strain gauges was mounted on the surface of the incident bar and then connected in a half Wheatstone bridge configuration to measure both the incident and reflected stress waves. The output from the strain gauge/Wheatstone bridge assembly was amplified by a differential preamplifier while the output from load cell was amplified by a charger amplifier. All the stress output and force output were recorded by an oscilloscope. Pulse shapers were used to shape the created square stress pulse to achieve a constant loading speed on the specimen. A single loading device was used to remove the majority of the stress amplitude after the first reflected pulses from the incident bar so that the specimens were loaded by a single pulse and no overload occurs in the load cell. For experiments on Kolsky bars, the velocity at the sample end of the incident bar could be calculated using the measured incident and reflected strain pulses [101],

$$v(t) = C_{\mathrm{B}}\left[\varepsilon_{\mathrm{I}}(t) - \varepsilon_{\mathrm{R}}(t)\right] \tag{5.1}$$

where $v(t)$ is the velocity at sample end of the incident bar, C_{B} is the elastic bar wave speed, $\varepsilon_{\mathrm{I}}(t)$ and $\varepsilon_{\mathrm{R}}(t)$ are the magnitudes of the measured incident and reflected strain pulses. The displacement $D(t)$ of incident bar end then can be obtained by integration of the velocity,

$$D(t) = \int_0^t v(\tau)\, d\tau \tag{5.2}$$

The high-speed synchrotron X-ray PCI was synchronized with the modified Kolsky bars in this study to record the real-time fracture behaviors in bone under dynamic loading. Figure 5.2 shows the assembly of the high-speed synchrotron X-ray PCI and the modified Kolsky compression bar. Such experimental method was used to investigate the mechanical behaviors in other materials under dynamic loadings [121-123] and the experimental details were well described elsewhere [119, 120].

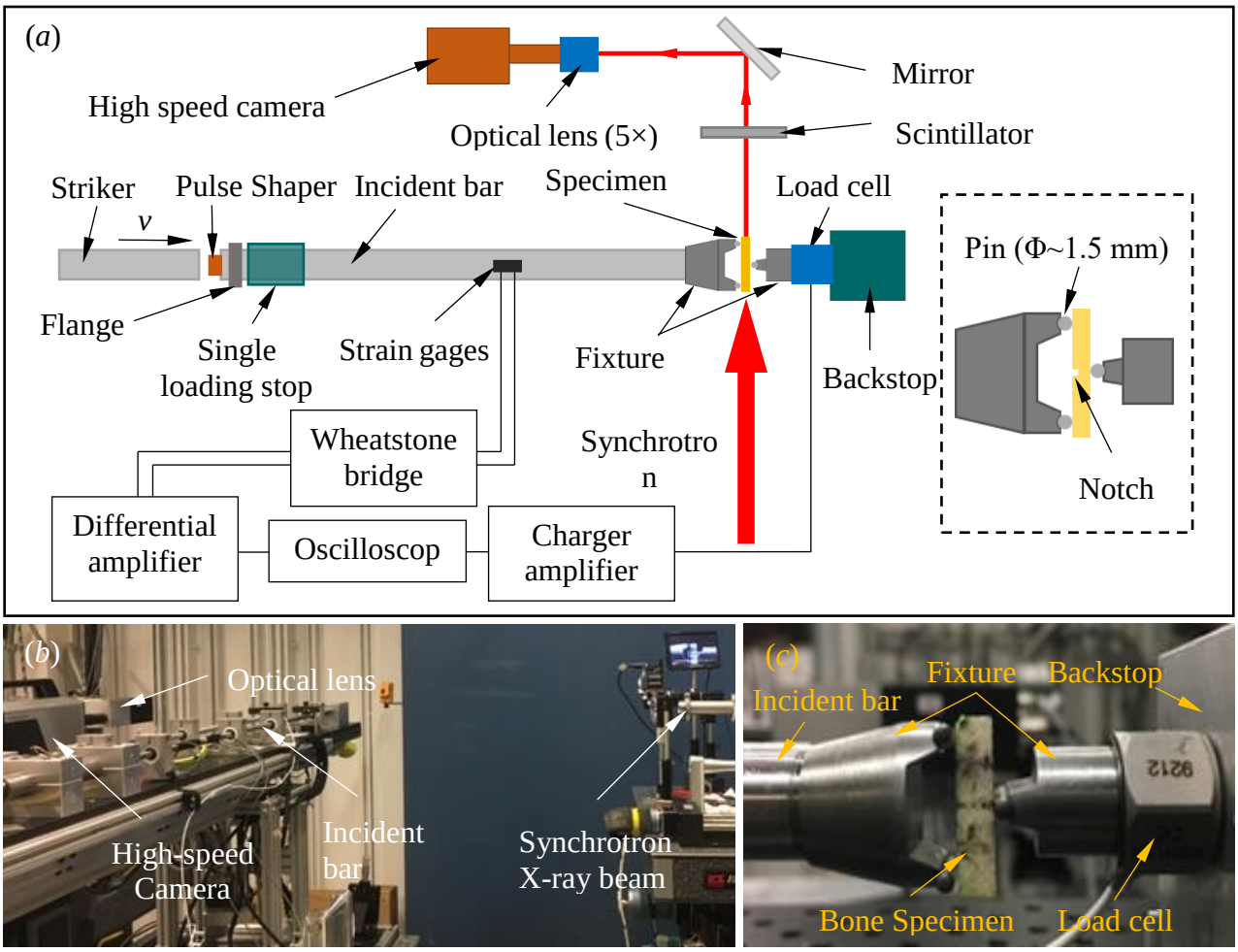

Figure 5.2 Experimental set-up at dynamic loading rate (a) Schematic of the experimental setup (b) Experimental setup in X-ray hutch at APS beamline 32 ID-B (c) A closer image for dynamic three-point bending configuration

X-ray PCI technique possesses two main advantages in visualizing the fractures in bone. On one hand, X-ray PCI utilizes the refraction of highly coherent X-rays and the differences in the change of X-ray phases as it passes through the bone specimens, resulting in an edge enhancement at interfaces in the resultant images and sharp contrasts between different microstructures in bone. On the other hand, X-ray PCI can effectively penetrate through all kinds of bone tissues, thereby allowing the visualization of their microstructures and fracture processes with high spatial resolution inside bone specimens rather than solely at their surfaces. The dynamic experiments using high intensity, high temporal and spatial resolution X-ray beam PCI were performed at the APS beamline 32 ID-B. The Kolsky bar was placed approximately 40 m downstream of the X-ray source and orientated 90° with respect to the beam pathline to subject the specimen to the X-ray

beam. A white X-ray beam with its fundamental energy centered at 25 keV was employed in this study and the cross-section of the evenly magnified beam was controlled to be 2.2 mm wide and 2 mm high. The X-ray wavelengths were converted to visible light via a single-crystal Lu3Al5O12 : Ce scintillator after it passed through the specimen and then reflected by a 45° mirror. The visible light was magnified by a 5× microscope objective lens and eventually recorded by a high-speed camera (Shimadzu Hyper Vision HPV-X2, Japan). A recording frame rate of 5,000,000 frames per second (fps) was used for all the five cortical bone specimens and four trabecular bone specimens, resulting in a temporal resolution of 200 ns for all the X-ray images. A recording frame rate of 2,000,000 fps was used for one trabecular bone specimen to record the entire fracture process using the longer time duration of camera action. The X-ray images were 2D images and the spatial resolution of all the X-ray images in this study was estimated to be 6.4 μm/pixel and the original frame size was 400 pixels in width and 250 pixels in height.

5.3.4 Quasi-static experiments

The quasi-static three-point bending experiments were conducted on MTS 810. A pair of grips made of steel was connected to the actuator and load cell to apply the three-point flexural loading. The configuration of the grips was designed as same as that for dynamic experiments on Kolsky bar. The displacement of the actuator was measured by a linear variable differentiate transducer (LVDT) installed in the testing frame while the force was measured by a quartz piezoelectric load cell (Type 9212; Kisler, NY, U.S.) with a response over a wide range of frequencies. The loading speed for all the quasi-static experiments on both the trabecular bone and cortical bone was controlled to be 0.01 mm/s constantly.

5.3.5 Fracture toughness measurements

The three-point bending experiments at both dynamic and quasi-static loading rates presented in this study were designed and performed such that the fracture toughness measurements on the bone specimens were in general accordance with ASTM standard E1820 [74]. For both of the two loading rate cases, the fracture toughness of bone specimen was determined in terms of the crack-initiation stress intensity K_{Ic} for mode I fracture and its value for a SENB specimen was calculated using the equation provided in [124]:

$$K_{\mathrm{Ic}} = \left[\frac{P_i S}{B W^{3/2}} \right] f\left(a_i / W\right) \tag{5.3}$$

where P_i is the applied load when the micro-crack initiated, S is the span of the three-point bending experiments and $f\left(a_i / W\right)$ is a function depends on the specimen's geometry [124]: the ratio of initial crack length, a_i, to specimen width, W. The initial crack length a_i is the initial depth of the pre-machined notch.

For both the dynamic and quasi-static three-point bending experiments performed to measure the fracture toughness of bone in this study, qualifications of K_{Ic} were met for all the bone specimens, i.e., b_0 (=W-a_0) > 2.5(K/σ_{YS})^2, as specified by ASTM Standard E1820, where σ_{YS} is the 0.2 % offset yield strength in tension. In the case where no available σ_{YS} could be found in literature for porcine cortical bone or trabecular bone, yield strength σ_{YS} or ultimate strength σ_{ult} of porcine bone or human bone determined previously (as listed in Table 5.1) [56, 125, 134] was used as a replacement to examine the validation of the measured fracture toughness in this study. The generated errors using the dynamic σ_{ult} instead of dynamic σ_{YS} was negligible as bone behaves as brittle materials especially under dynamic loadings, while the errors were not known in this study when the quasi-static σ_{YS} of human cortical bone was used as a replacement of σ_{YS} for porcine cortical bone.

Table 5.1 Mechanical properties of bone in literature

Bone type	Quasi-static	Dynamic
Porcine cortical bone	-	σ_{ult}, 50 MPa (300/s) [125]
Porcine trabecular bone	σ_Y, 7.3 Mpa (0.01/s) [56]	σ_Y, 10.1 MPa (400/s) [56]
Human cortical bone	σ_Y, 108 MPa (0.002/s) [134]	-

Images showing the fracture surfaces and crack path profiles of the postmortem specimens at microscopic length scales were obtained using two scanning electron microscopes (SEM). The first SEM (Quanta, FEI, OR, U.S.) was operated at 5 kV accelerating voltage at high vacuum and low vacuum at a pressure of 60 Pa in the secondary electron mode. The second SEM (Nova, FEI,

OR, U.S.) was operated at 5 kV at high vacuum so that higher magnification SEM images could be obtained to capture the smaller microstructures in bone specimens

5.3.6 Statistics

Shapiro-Wilk (S-W) tests were performed first to check the normality of the data. To examine the differences in fracture toughness between the loading rates and bone types, two-way ANOVA with post-hoc tests were performed under Bonferroni correction. *t*-Tests was also performed to examine the difference in geometry parameters of the crack initiation locations between different bone types. *p*-Values larger than alpha level of 0.05 were considered normally distributed for S-W tests while *p*-values less than 0.05 were regarded as statistically significant for ANOVA tests this study.

5.4 Results

5.4.1 Microstructures in bone

The reconstructed three-dimensional tomographic images of the cortical and trabecular bone were presented in Fig. 5.3a, b, respectively. The difference of microstructures is apparent between the two types of bone, as the cortical bone is denser while the trabecular bone is more porous. The light narrow rod alike structures (Fig. 5.3a) features the Haversian canals in cortical bone, showing the osteons, the unit functional structures in cortical bone, are aligned parallel in the same direction. The microstructures in nasal bone possess the typical features of trabecular bone tissue: it is lattice-like and mainly consists of structures in shapes of rod and plates, which is named as trabeculae and act as the unit functional frames in trabecular bone (Fig. 5.3b). However, it is also seen that nasal bone's trabecular bony tissue is comparatively denser and the size of its pores is smaller when compared with trabecular bone found in skull. As verified by Fig. 5.3*a*, the pre-machined notch was orientated such that its normal direction was perpendicular to the osteons in cortical bone. The maximum diameter of the osteon in the representative cortical specimen was observed to be ~220 μm. The wall thickness of trabeculae in nasal bone was in the range of ~50 μm-440 μm. The porosities of the cortical bone and trabecular bone were measured to be 15.8% (SD: 1.0%) and 35.0% (SD: 1.7%).

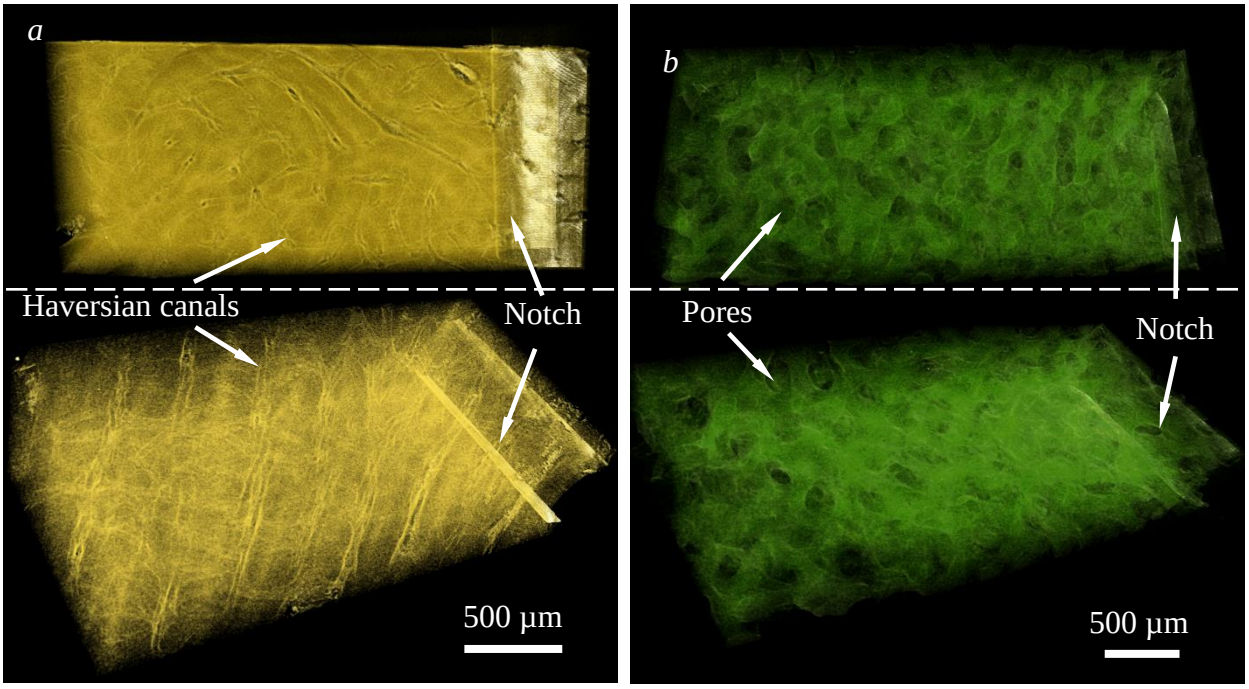

Figure 5.3 Three-dimensional tomographic images for bone specimens (a) cortical bone (b) trabecular bone (nasal bone)

5.4.2 In-situ dynamic fracture visualization

Dynamic three-point bending experiments were performed on the bone specimens using the modified Kolsky bar. The average loading velocity for all the dynamic experiments was calculated to be 6.1 ± 0.1 m/s using equation (5.1). The whole fracture process, including the onset of the fracture initiation and subsequent fracture propagation, were observed with the high-speed X-ray PCI visualization technique. Ten experiments under identical testing conditions, with five for each of the trabecular bone and cortical bone, were performed repeatedly to ensure data repeatability. The recorded high-speed X-ray images (5,000,000 fps) showing the fracture processes in two representative experiments are provided in Figs. 5.4 & 5.5 and Figs. 5.6 & 5.7 for the cortical bone and trabecular bone, respectively. Due to the differences in microstructures of cortical bone and trabecular bone (as seen in Figs. 5.4-5.7), the crack paths varied significantly in the two types of specimens, as crack trajectories in cortical bone were more tortuous while they were comparatively straight in trabecular bone. Fracture deflections at the osteon cement lines, acting as a major crack-resistance mechanism, were observed in the cortical bone specimens under dynamic loading in

this study. On the contrary, very limited toughening mechanisms could be observed in trabecular bone.

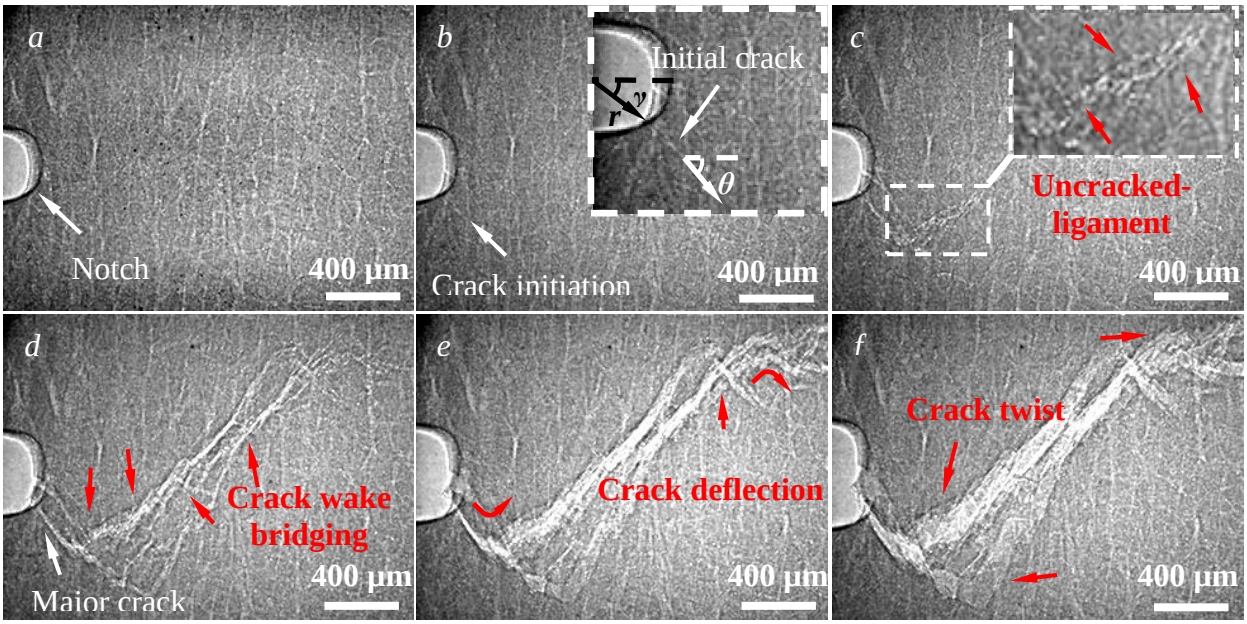

Figure 5.4 High-speed X-ray images of the representative cortical bone specimens I. (a) t=0 μs, (b) t=23.8 μs, (c) t=25.6 μs, (d) t=27.8 μs, (e) t=29.4 μs, (f) t=34.6 μs. The r was the round notch's root radius and the angle γ was measured as the center angle between the location where the crack initiated and the point where the round notch intersected the horizontal symmetric axis. A positive γ denotes counter clock-wise direction while a negative γ denotes clock-wise direction. The angle θ was defined as the angle between the propagation direction of the incipient crack (before a crack deflection occurred) and the horizontal symmetric axis.

As shown in Fig. 5.4 for the high-speed X-ray images of the first cortical bone specimen, the irregular shaped 'strip' featured the lamellae in cortical bone while the light narrow lines represented the Haversian canals (parallel to the lamellae) and Volkmann canals (perpendicular to lamellae). The notch, with its initial normal direction perpendicular to the osteon axis, was located on the left edge of the figures. The two-point fixture connected to the incident bar was located on the left side of the specimen while the one-point fixture mounted on the load cell was on the right side. The onset of the crack initiation took place at the radius root of the notch (Fig. 5.4*b*) and inclined with an angle γ of ~-55° (clockwise direction) to the horizontal direction (transverse to the osteon axis). The initial crack propagation direction, denoted by θ, was measured to be ~-46° with respect to the horizontal axis. After propagating straightly along the initial direction for

approximately ~287 μm, the crack bifurcated into two major cracks, with one crack deflected ~90° at first and followed closely by the other one after it further propagated a short distance along the initial direction. As the crack continued to travel along the direction orientated ~45° to the horizontal axis for about 1.7 mm, it deflected ~90° again, exhibiting an overall serrated crack path and a rough fracture surface. Besides in-plane crack deflections, out-of-plane crack twists (Fig. 5.4*f*) also occurred at the same time and they could both act as potential toughening mechanisms in crack resistance by largely increasing the driving force necessary for further crack propagation. Other fracture toughening mechanisms, such as uncracked ligament bridging and crack wake bridging were also observed in this study in cortical bone (Fig. 5.4*c*, *d*).

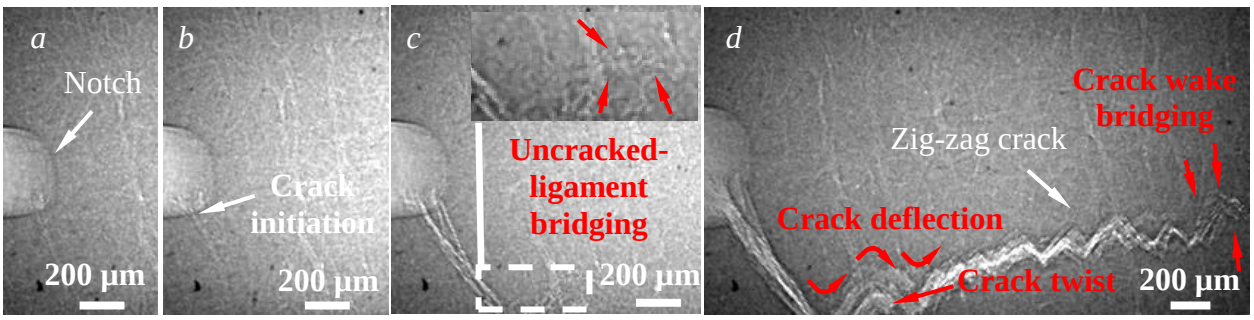

Figure 5.5 High-speed X-ray images of cortical bone specimens II (a) t=0 μs. (b) t=21.8 μs. (c) t=29.2 μs. (d) t=32.8 μs. (e) t=42 μs

High-speed X-ray images of the second cortical bone specimen were presented in Fig. 5.5. The crack initiated at the notch surface and took a straight path at first by directly penetrating through all the osteons until it deflected 90° after propagating ~600 μm along the initial direction (Fig. 5.5). Afterward, the crack started traveling along an approximately horizontal path with a highly zig-zag shape. A further discussion on such a different crack path from that in the first specimen is provided in the next section. With the same definition as demonstrated in Fig. 5.4, the angle γ and θ of the second cortical bone specimen were ~-49° and ~-56°, respectively.

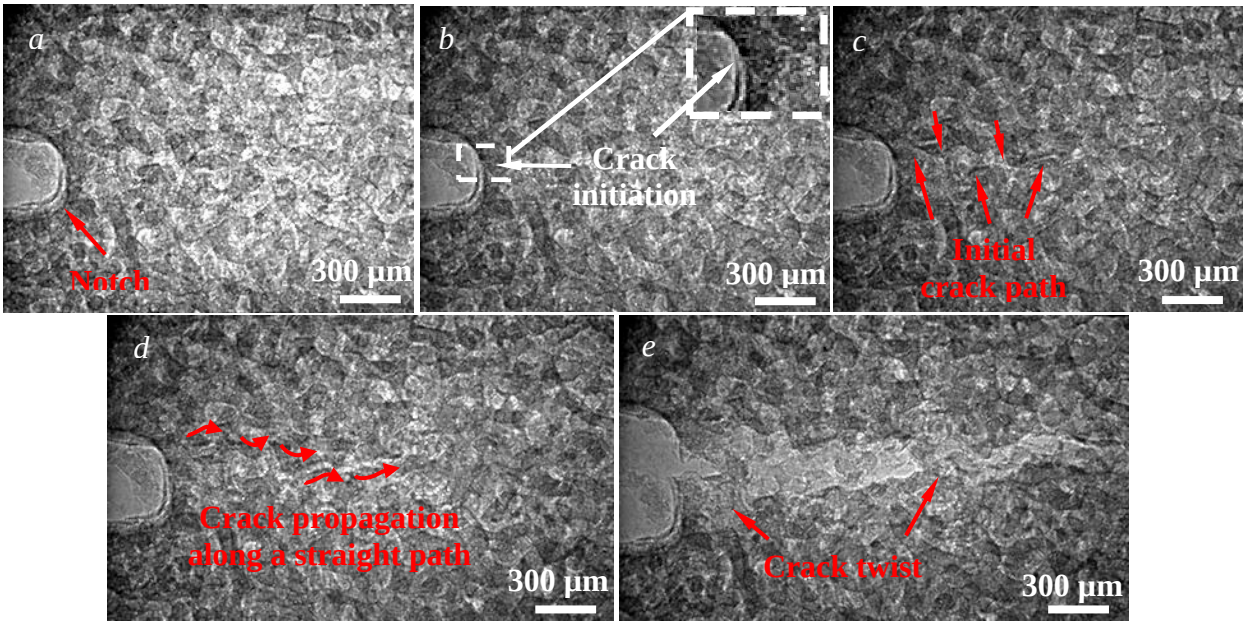

Figure 5.6 High-speed X-ray images of representative trabecular bone specimen I (a) t=0 μs. (b) t=21.8 μs. (c) t=24.2 μs. (d) t=33 μs. (e) t=38.6 μs

As presented in the high-speed X-ray images in Fig. 5.6, the microstructures and crack paths were largely different in nasal bone comparing with cortical bone. The dark area in 'rod' and 'plates' shape represented the trabeculae and the bright areas enclosed by trabeculae denoted the pores. Same as that in cortical bone, the crack was initiated at the notch root (Fig. 5.6b) on the left side in the images. As defined in cortical bone in Fig. 5.4b, the angle γ, denoting the location of crack initiation, and angle θ, representing the crack's subsequent propagation direction, were measured to be 57°/0° and 0°/-21° (two major cracks), respectively. The crack then propagated in a long and slightly wavy path by traveling along or breaking through the trabeculae till the right edge of the image. Comparing with the cortical bone, the entire crack path in nasal bone was straighter, with few deflections and twists (Fig. 5.6d, f) observed during the crack propagation.

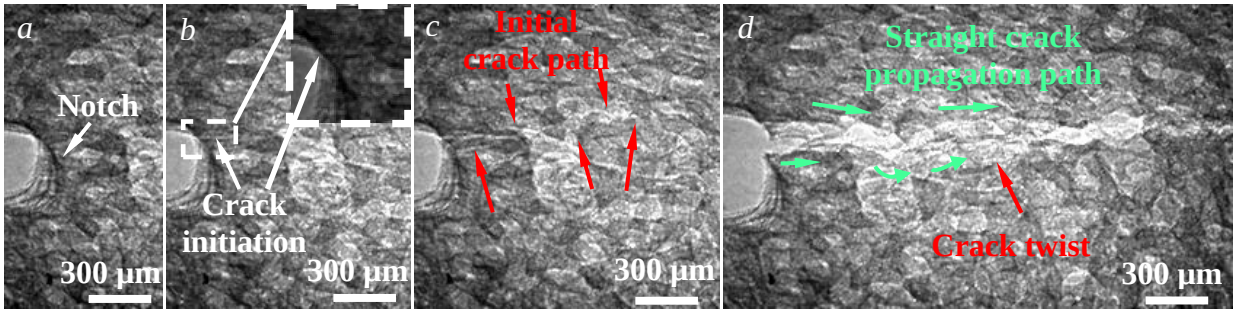

Figure 5.7 High-speed X-ray images of representative trabecular bone specimen II. (*a*) *t*=0 μs, (*b*) *t*=29.2 μs, (*c*) *t*=31 μs, (*d*) *t*=48.2 μs

The high-speed X-ray images of the second trabecular bone specimen were presented in Fig. 5.7. The crack was initiated at the notch root (Fig. 5.7b) as expected. The angle γ and θ were measured to be 45° and 0°, respectively. Comparing with the first trabecular bone specimen, the crack in the second specimen propagated along an even straighter path towards the right edge of the bone specimen by penetrating straight through the whole microstructures. Even along such a straight crack path, there were some mild curves along the trabeculae direction, implying the influence of the trabecular microstructures in trabecular bone on the crack propagation at dynamic loading rate. The load-displacement curves synchronized with the high-speed X-ray images for the first cortical bone and first trabecular bone specimen were plotted in Fig. 5.8, where it was seen the cracks initiated shortly before the load peaks.

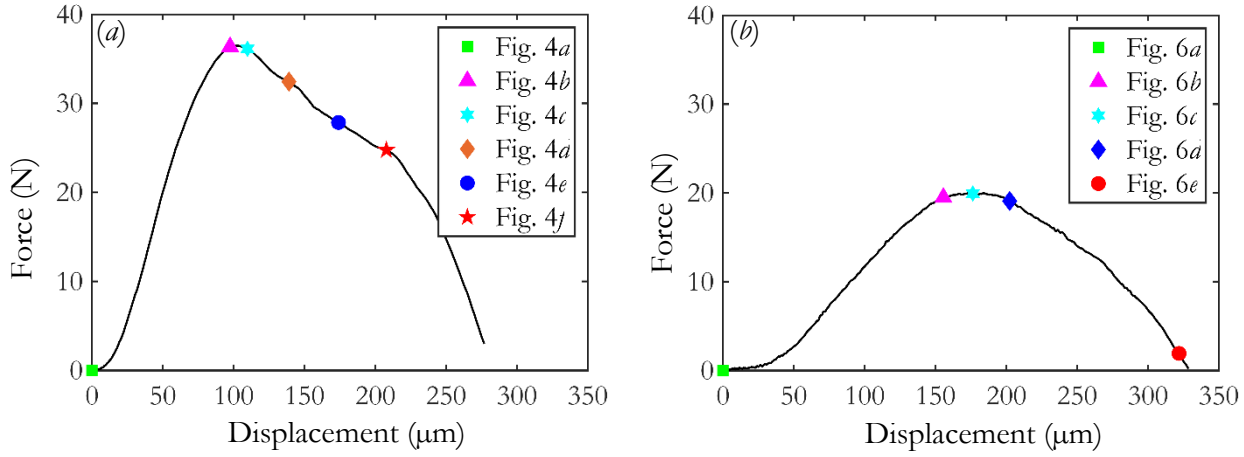

Figure 5.8 Load-displacement curves for the bone specimens (*a*) cortical bone specimen I (Fig. 5.4*a*–*f*) (*b*) trabecular bone specimen I (Fig. 5.6*a*–*e*).

5.4.3 Fracture toughness and crack velocity

The fracture toughness in terms of crack-initiation stress intensity of mode I fracture was determined for both loading cases by assuming that the linear elastic fracture mechanics is valid for more porous trabecular bone and the load reached the peak as the crack initiated for the case of quasi-static loading rate. The crack-initiation toughness, K_{Ic} was plotted against stress intensity rate for all the 20 specimens in Fig. 5.9*a*, where the previously measured crack-initiation toughness, K_{Ic}, of other bones, such as bovine cortical bone [51], equine cortical bone [58] and human cortical bone [74] at different loading rates were also included for comparison. The average K_{Ic} of both types of bone for each loading case was also provided with the *p*-values of the ANOVA tests in Fig. 5.9*b* and Table 5.2. The crack extensions in each of the five dynamically loaded cortical and trabecular bone specimens were measured using the high-speed X-ray images. The fracture toughness, in terms of stress intensity, *K* and the crack propagation velocities of the bone specimens at dynamic loading rate were then determined accordingly and plotted in terms of the crack extension in Fig. 5.9*c* and 5.9*d*.

Table 5.2 Fracture initiation toughness for cortical and trabecular bone at quasi-static and dynamic loading rates

	Quasi-static (0.01 mm/s)		Dynamic (6.1 m/s)	
	Stress intensity (SD)	S-W test	Stress intensity (SD)	S-W test
Cortical bone	3.49 MPa·√m (0.77)	0.77	2.19 MPa·√m (0.24)	0.96
Trabecular bone	1.97 MPa·√m (0.25)	0.99	1.55 MPa·√m (0.27)	0.94

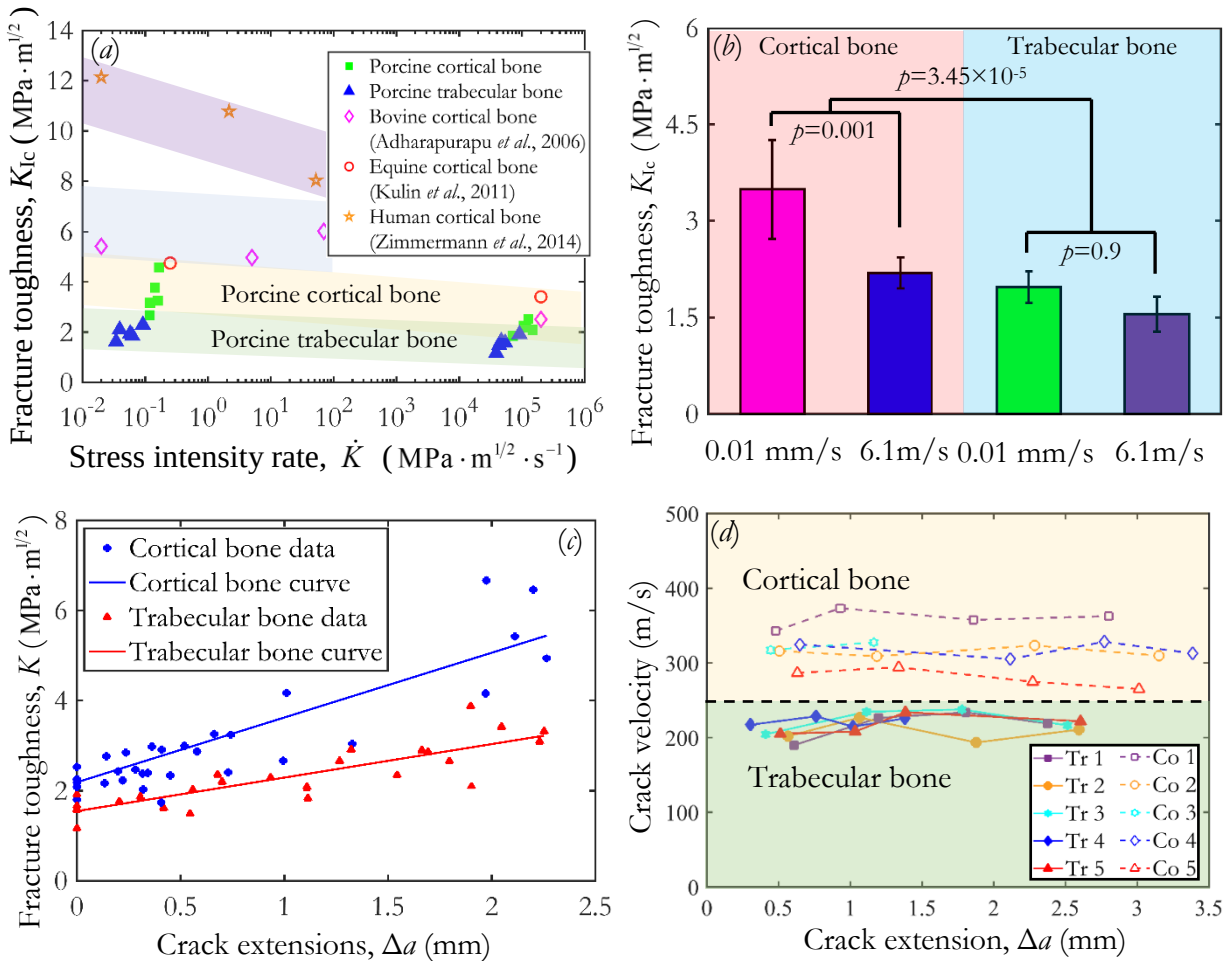

Figure 5.9 Fracture initiation toughness of bone at different loading rates (*a*) fracture toughness of all the specimens in terms of stress intensity rate (*b*) average fracture toughness of cortical and trabecular bone at quasi-static and dynamic loading rates (*c*) crack-resistance curves (*R*-curves) in terms of the stress intensity, *K*, as a function of crack extension at dynamic loading rate (*d*) crack velocity-crack extension curve for cortical bone and trabecular bone at dynamic loading rate (Co: Cortical bone specimen, Tr: Trabecular bone specimen)

Similar as the trend reported previously [37-39, 75, 78], the average K_{Ic} of both types of bone generally decreased as loading rate increased from quasi-static to dynamic (Fig. 5.9*b*). Specifically, the K_{Ic} of cortical bone statistically significantly decreased with a ratio of 37% as strain rate increased. Such decrease in fracture toughness in bones was consistent with the observations of the fracture surfaces in the postmortem specimens as presented in Fig. 5.10. At dynamic loading rate, the fracture toughness of both the porcine cortical and trabecular bones (from Nasal bone) increases as crack propagates, while the R-curve for trabecular bone increases less significantly than the cortical bone. In general, the cracks propagated with higher velocities in cortical bone

specimens, as the average velocity in the cortical bone was 318 m/s (SD: 29 m/s) while it was 218 m/s (SD: 14 m/s) in the trabecular bone specimens. The SEM images indicated that the cracks took comparatively more smooth paths in dynamically loaded bone specimens (Fig. 5.10*a*, *b*), while more tortuous fracture surfaces were observed in specimens that loaded at quasi-static rate (Fig. 5.10*c*, *d*).

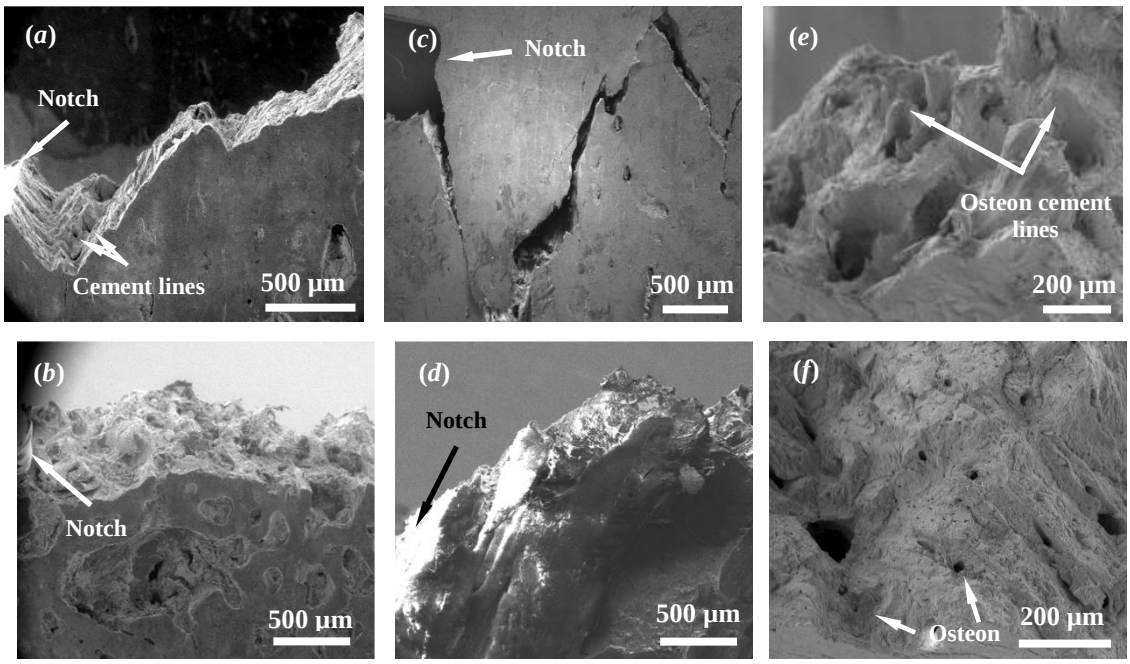

Figure 5.10 SEM images showing the fracture surfaces and crack paths of the bone specimens (*a*) fracture surface of a representative cortical bone specimen under dynamic loading (*b*) fracture surface of the trabecular bone specimen loaded dynamically (*c*) one representative cortical bone specimen loaded at quasi-static rate (*d*) fracture surface of trabecular bone specimen loaded at quasi-static rate (*e*) image at higher magnification showing the highly tortuous fracture surface of cortical bone loaded at quasi-static rate (*f*) image at higher magnification showing the comparatively smooth facture surface of cortical bone loaded at dynamic rate

5.5 Discussions

5.5.1 Fracture toughness and toughening mechanisms

A complete study of fracture behaviors in bone should cover the entire fracture process, including the crack initiation, subsequent crack propagation, fracture toughening mechanisms and consequently its fracture toughness. In this section, each of those aforementioned aspects in the

two types of bone under dynamic loading together with the effect of loading rate on fracture toughness are discussed.

In terms of cortical bone, a large number of studies have reported previously that the crack tends to deflect at osteon cement lines in transversely orientated bone (pre-machined north direction perpendicular to osteon axis), which was regarded as the major crack toughening mechanism at quasi-static loading rate. At comparatively higher strain rate (0.1/s), fracture deflection was significantly decreased when compared with low rate (10^{-5}/s) based on the SEM images of postmortem specimens [75]. Such reduced extent of crack deflection and crack twist was also found in our study, which reaffirmed the findings in previous studies [75]. For example, at the quasi-static loading rate, the crack in cortical bone followed an expected extremely tortuous crack path through the microstructure with numerous deflections and twists, as the crack deflected almost 90° right after it initiated at the notch and then traveled along the axis of osteons (Fig. 5.10c). As shown in closer examinations at high magnifications (Fig. 5.10e), the whole osteons protruded from the fracture surface and some cement lines containing several concentric lamellae rose above the surface, suggesting that the crack deflected at, and then followed, the cement lines as it propagated through the bone microstructure, which provide the major contribution to fracture toughness of bone. However, crack deflections at the cement-line, although the extent was diminished, still existed in those dynamically loaded cortical bone specimens (Figs. 5.4, 5.5 and 5.10a), indicating that the highly mineralized osteons still played a role in crack resistance under dynamic fractures despite the largely decreased plasticity of the microstructures around the crack tip. Besides crack deflections and twists, evidence in the high-speed X-ray images that ligament bridging and bridging by fibrils in crack wake also played a role in resisting crack in cortical bone was further verified by the SEM images as shown in Fig. A1c. On the other hand, as shown in the high-speed X-ray images (Figs. 5.6 and 5.7) and SEM images (Fig. 5.10b), the crack in dynamically loaded trabecular bone traveled along the trabeculae and propagated straight through the overall bone structures, showing a slightly wavy crack trajectory. Such a straight crack path and smoother fracture surface were mainly owing to the largely limited potential fracture toughening in trabecular bone, which in turn could be a consequence of both the dynamic loading and its porous microstructures. The crack path in trabecular bone under quasi-static loading (Fig. 5.10d) was found to be comparatively more tortuous than that under dynamic loading (Fig. 5.10b), indicating that, although no statistical significant difference in fracture initiation toughness

between the dynamic and quasi-static loading rate was found (Fig. 5.9b), there was still some extent of potential deleterious effect on fracture toughening of trabecular bone due to dynamic loading rate.

When a crack impinging on the interface between two different materials, whether it deflects at the interface or more likely penetrates through the whole structure could be determined by the theoretical equations of He and Hutchinson based on the linear-elastic fracture mechanics [135]. The equations were applied in literature for analysis of crack propagation in bone under the assumption that the crack impinges the interface perpendicularly [74, 136, 137]. However, the situation in our study is more complex as it is shown (Figs. 5.4 and 5.5) that the crack impinged the interface between the interstitial lamellae (bony tissue between osteons) and osteons at ~45°. Supposing the crack starts at the interstitial lamellae without losing the generality, the conditions of crack penetration or deflection according to the theoretical framework of He and Hutchinson are [135]:

$$\begin{cases} \text{if} \;\; G_{\text{int}}/G_{\text{ost}} < G_{\text{d}}/G_{\text{p}}, \;\; \text{Crack tend to deflect} \\ \text{or} \;\; G_{\text{int}}/G_{\text{ost}} > G_{\text{d}}/G_{\text{p}}, \;\; \text{Crack tend to penetrate} \end{cases} \tag{5.4}$$

where G_{int} and G_{ost} are the mode I fracture toughness of the interstitial lamellae and osteons, $G_{\text{d}}/G_{\text{p}}$ is the ratio of strain energy release rate between crack deflection and crack penetration, which primarily depends on the Dundurs' parameter $\alpha = (E_{\text{int}}-E_{\text{ost}})/(E_{\text{int}}+E_{\text{ost}})$, a parameter for the mismatch of elastic tensile modulus E in plane strain state between the interstitial lamellae (E_{int}) and osteons (E_{ost}). Generally, osteons are less mineralized and they behave less stiff than the interstitial bone tissue, i.e., $E_{\text{int}} > E_{\text{ost}}$ [49, 138, 139]. For the case where the crack impinged the osteon cement line at 45° and the interstitial bone is stiffer, it yields $\alpha>0$, giving the ratio $G_{\text{d}}/G_{\text{p}}$ only slightly larger than 1 (ranging from 1 to 1.05) and creating the constraint condition $G_{\text{int}}/G_{\text{ost}} < 1.05$ for crack deflection ($G_{\text{int}}/G_{\text{ost}} > 1.05$ for crack penetration) [135]. This implies the generally higher toughness of interstitial bone as it is seen in the high-speed X-ray images (Figs. 5.4 and 5.5) that the crack propagated in cortical bone mostly by penetrating through the osteons. The observed crack deflections could be presumably because of the local specific microstructures. For example, in the area where the crack deflected, the local interstitial lamellae are less tough comparing with the osteons they surrounded, resulting in the ratio $G_{\text{int}}/G_{\text{ost}}$ less than 1. However, the above discussion on crack deflections or penetrations is mainly based on the linear elastic fracture mechanics and by assuming there was only mode I fracture occurring in the bone. The real

situations in bone under three-point bending are actually significantly more complicated and multiple factors, such as the microstructures in the specific bone material, the dynamic loading conditions and the complex mixed fracture of mode I and II, all could play roles and interact with each other in determining the specific crack path as those observed in the cortical bone specimens (Figs. 5.4 and 5.5).

As mentioned previously in the experimental results, the dynamic crack took a highly zig-zag path (a large number of crack deflections in a short distance) during its later period of propagation in the second cortical bone specimen (Fig. 5.5) and such a crack path could be due to the minor different microstructures in the second specimen (Fig. A1*a*). It is well known that each Haversian canal is surrounded by concentrically arranged lamellae and therefore they are named as concentric lamellae [140]. Approaching the surface of the cortical bone, the lamellae are aligned parallel to the surface and are called circumferential lamellae consequently [140]. A schematic of typical microstructures in cortical bone is presented in Fig. A2*a*, where schematics illustrating the crack propagations in the two representative cortical bone specimens (Figs. 5.4 and 5.5) are also included (Figs. A2*b* and A2*c*). By further examining the microstructures and fracture path in the SEM images of second cortical bone specimen, it was found that the zig-zag path ($G_{int}/G_{ost} < 1.05$ for crack deflection) occurred mostly at the interfaces between circumferential lamellae (Figs A1*a* and Fig. A2*c*), suggesting that the fracture toughness of circumferential lamellae is presumably higher than the concentric lamellae. The fracture initiation toughness, K_{Ic} of the second representative cortical bone specimen at dynamic loading rate is 2.19 MPa·m$^{1/2}$, which is same as the average K_{Ic} of all the dynamic loaded cortical bone specimens. The reason is presumably that the K_{Ic}, reported in our study, is measured with respect to the crack imitation and the microstructures (concentric lamellae) are similar at the notches and in the areas around crack initiation locations for all the cortical bone specimens, although the second representative cortical bone specimen exhibited different microstructure (circumferential lamellae) in its later period of crack path. It is also worth noting that there is only one cortical bone specimen with such highly zig-zag crack path and circumferential lamellae microstructure, future study is needed to confirm that the highly zig-zag crack path is a consequence of the circumferential lamellae.

At the same loading rate, it is seen that the crack-initiation toughness of cortical bone was higher than trabecular bone (Fig. 5.9*b*). Such higher crack-initiation resistance of cortical bone evaluated quantitatively was also verified qualitatively by the observed more apparent toughening

mechanisms, such as crack deflections, twists and uncracked ligament bridging in high-speed X-ray images, which in turn result in the much more tortuous crack path in it. It is worth noting that our K_{Ic} of porcine cortical bone for both the quasi-static and dynamic loading rate is at the same level of other cortical bones [51, 131] (except for human cortical bone, showing a significantly higher fracture toughness than other animals bones [74]) under similar measuring conditions (Fig. 5.9*a*). The slight difference in K_{Ic} between porcine bone and other animal bones [51, 131] could be due to the different species and anatomical locations of the specimens used in their studies. The crack-initiation toughness, K_{Ic} of porcine trabecular bone extracted from nasal bone for both loading cases were higher than the human trabecular bone and equine trabecular bone tested at quasi-static loading rates previously, where K_{max} values of ~0.1-0.6 MPa/√m were reported [130]. Such higher toughness could be a result of the relatively lower porosity of the trabecular bony tissue extracted from nasal bone than those in skull bones or at the ends of long bones. It also should be noted that the reported crack-initiation toughness of bone specimens in our study could be higher than the bone's intrinsic fracture toughness as the cracks initiated from notches with comparatively larger radius instead of pre-cracks. Comparing with the reported crack-resistance curves (R-curves) for bovine cortical bone [58] and human cortical bone in the literature [74], it is found that, under dynamic loading rate, the fracture toughness of porcine cortical bone is rising less significantly than the bovine cortical bone as crack propagates. The dynamic R-curve of porcine cortical bone also increases less significantly than the quasi-static R-curve of human cortical bone, which can be due to the dynamic loading conditions and the different species. The dynamic R-curves are based on the results from a small specimen population (5 specimens for each cortical bone and trabecular bone), future study may be needed to further confirm the R-curves presented here. In addition, the radiation exposures in our study, owing to the X-ray tomography before mechanical loading, were ~16 kGy and ~18 kGy for the cortical bone and trabecular bone, respectively, which can potentially apply a deleterious effect on the properties of bone. However, the effect of such low dose radiation (<30 kGy) on the bone's mechanical properties was reported differently in the literature, as the fracture toughness decreased ~22% under exposure of 27.5 kGy in [62] while no significant effect was found in strength, strain at failure and force at failure for radiation of 20-25 kGy in [63].

5.5.2 Crack initiation and propagating velocity

For all the ten bone samples tested under dynamic loadings, the cracks initiated on the notch root surfaces but with a small extent of variations in their locations. Multiple factors determine the location of crack initiation, among which there are two major aspects: intrinsic microstructures in bone and extrinsic mechanical state because of the loading conditions. The angles γ and θ, as defined earlier in Fig. 5.4, were measured for all the ten specimens and listed in Table 5.3. As shown succinctly, the angle γ, denoting the onset location of crack initiation, was in general consistent for all the ten bone specimens (two major cracks were observed in two trabecular bone specimens) and statistically independent of the bone type, indicating that the locations of crack initiation likely mainly depend on the extrinsic loading conditions: such as loading rate and stress state, rather than microstructures in bone. However, the situation for θ, a measurement of the propagation direction of incipient crack, was quite different: it was generally consistent for cortical bone while varied tremendously among the trabecular bone specimens, exhibiting a significant dependence on bone types. Provided that the loading conditions are similar in the two types of bone, such variations could be mainly due to that, in the area close to the locations of crack initiation, the intrinsic microstructure is the primary factor in affecting the crack propagation direction in cortical bone while it was presumably the extrinsic tensile stress state in trabecular bone that played a dominant role in determining the crack propagation direction.

Table 5.3 Onset location of crack initiation and the direction of its subsequent propagation in bone

Angle	Bone type	No. 1	No. 2	No. 3	No. 4	No. 5	Average	SD	*t*-Test
γ	Cortical bone	-55°	-55°	48°	40°	-49°	49°	6.2°	A
	Nasal bone	-56°/0°	57°/0°	45°	49°	40°	49°	7.2°	A
θ	Cortical bone	-46°	-46°	48°	-43°	-56°	48°	4.9°	-
	Nasal bone	-40/0°	0°/-21°	0°	0°	20°	4°	8.9°	-

Note: 1. A positive value of angle denotes counter-clockwise direction while a negative value denotes clockwise direction. Two major cracks occurred in trabecular bone specimen 1 and 2.

2. No significant difference is found in γ between cortical and trabecular bones according to *t*-Test.

The crack velocity was found to be dependent on bone types (Fig. 5.9*d*). Considering that the loading condition and specimen geometry were same for the two types of bone, an observed lower

crack velocity in trabecular bone than in cortical bone (Fig. 5.9*d*) indicates that the crack velocity was influenced by the microstructures in bone. Previous theoretical studies reported that, when crack propagating at a comparatively lower speed, the majority of strain energy is allocated to volume change instead of shape change of the area in front of the crack tip, which results into a crack with fewer bifurcations and therefore a smooth fracture surface in material [126]. This was further verified in our study by the less tortuous crack path and smoother fracture surface observed in trabecular bone than that in cortical bone.

5.6 Conclusions

In this study, the real-time visualization of the entire fracture process, including crack initiation and subsequent crack propagation in porcine cortical bone and trabecular bone under dynamic loadings was achieved using the technique integrating high-speed synchrotron X-ray PCI with a modified Kolsky compression bar. Quasi-static experiments were also performed to investigate the effects of loading rate on fracture toughness for both types of bone. The onset location of crack initiation was found to be independent of the bone type, which was presumably due to the loading conditions instead of microstructures. While the incipient crack propagation direction was mainly determined by intrinsic microstructures in cortical bone while by extrinsic stress state in trabecular bone. Under dynamic loading, the crack took a more tortuous path in cortical bone, as crack deflected approximately 90° at osteon cement lines, acting as a major potential toughening mechanism against crack propagation. In comparison, the crack propagated with lower speed in trabecular bone and traveled straight through the whole microstructures, which is a consequence of its lower crack resistance to dynamic fractures. The loading rate effect was apparent: the fracture surfaces were more tortuous in quasi-statically loaded specimens for both types of bone and the fracture toughness of cortical bone decreased statistically significantly as the loading rate increased.

CHAPTER 6. THE EFFECTS OF LOADING-DIRECTION AND STRAIN-RATE ON THE MECHANICAL BEHAVIORS OF HUMAN FRONTAL SKULL BONE

Adapted from:
X. Zhai, E.A. Nauman, D. Moryl, R. Lycke, W.W. Chen. The Effects of Loading-direction and Strain-rate on the Mechanical Behaviors of Human Frontal Skull Bone, Journal of the Mechanical Behaviors of Biomedical Materials. Under review.

6.1 Abstract

Most fatal human skull injuries occur under impact loading conditions, such as car collisions, where the strain rates fall in the range of intermediate ($1/s-10^2/s$) and high ($10^2/s-10^3/s$) rates. Therefore, knowledge of the mechanical behaviors of human cranial bone at higher strain rates, i.e., intermediate and high strain rates, may provide insight into the prevention of skull injuries and help the design of efficient head protection systems. In the present study, the compressive mechanical behaviors of human frontal skull bone along and perpendicular to its through-the-thickness direction were experimentally characterized at quasi-static (0.01/s), intermediate (30/s) and high (625/s) strain rates in this study. A total number of 75 specimens prepared from three male donors with ages of 70-74 were separated into three groups: quasi-static (N=23), intermediate (N=23), and high (N=29) strain rates. Experiments at quasi-static and intermediate strain rates were performed using a hydraulically driven materials testing system (MTS), while a Kolsky compression bar was used to load the skull bone specimen at high strain rates. X-ray computed tomography was performed to obtain the structural parameters and visualize the microstructures of the skull bone. The *in-situ* failure processes of the specimens under high-rate loading were documented by a high-speed camera. The stress-strain responses for both diploë and cortical bone layers of human skulls were then deduced from the experimentally determined mechanical behaviors of human skulls using simplified mechanical models. The human skull exhibited a loading-direction dependent mechanical behavior, as higher ultimate strength and elastic modulus were found in the direction perpendicular to the thickness when compared with those along the thickness direction, exhibited an increasing ratio as high as 2 and 3 for strength and modulus, respectively. High-speed images revealed that the specimens loaded along the thickness direction generally failed due to the crushing in diploë (the trabecular bone tissue) whereas separation of the

entire architecture was observed as the main failure mode when compressed in the perpendicular direction. The effect of strain rate was also evident: the skull specimens were increasingly brittle as strain rate increased from quasi-static to high rate for both the loading directions. The elastic modulus increased by a factor of 4 in radial direction and it increased by a factor of 2.5 in the tangential direction across the quasi-static, intermediate and high strain rates. Significant differences were also found in ultimate strength and work to failure as loading rate increased from quasi-static to high rates. The results also suggested that the strength in the radial direction was mainly depended on the diploë porosity while the diploë layer ratio played the predominant role in tangential direction. The deduced stress-strain responses of both diploë and cancellous bone layers in the human skulls were found to be strain-rate dependent. The strength of the cortical bone layer obtained in this study agreed well with the data for human skull's cortical bone in the literature.

6.2 Introduction

Human adult cranial bone has a typical sandwich architecture: with the inner and outer layers comprised of dense cortical bony tissue and porous spongy cancellous bone located in between. The cortical bone layers are stiffer and display a highly randomly aligned collagen fibers [141] while the inner lightweight trabecular core develops a homogenous lattice-like structure (lamellae) and exhibits superior energy absorbing properties [70, 142]. A consequence of this architectural structure is that the mechanical behaviors of the cranial bone could be highly loading direction dependent: the porous trabecular core bears more load in radial direction than in tangential direction, resulting in transversely isotropic mechanical properties. The cranial bone is mainly responsible for protecting brain tissue from damage due to injuries, hence fatal traumatic damage in cranial bone occurs under various loading conditions, especially those at the intermediate and high strain rates involved in impact events, such as car collisions and other blunt-force impacts [90]. For example, it was reported that the skull subjected to blunt impact or blast loading experienced a strain rate of at least 14/s [87]. Thus, it is important to quantitatively describe the cranium's dynamic mechanical behaviors in those situations.

While human cranial bone has been extensively studied in the literature [69-72, 87, 90, 91, 142-150], the recorded fundamental mechanical properties of its entire sandwich structure [69-72, 142-147], such as ultimate strength or modulus, are vastly varied as shown in Table 6.1. This can

be attributed to multiple factors: the morphological and physiological variations among the skull subjects, various loading types applied during mechanical characterization, and different specimen shapes and sizes. For example, studies suggested that the mechanical properties of cranial bone are correlated to its structural parameters, such as the apparent ash density and the skull's thickness [48, 69, 151-154]. However, those parameters vary widely among individual skulls or even within the same skull at different anatomical locations, which might be the primary reason for the varied documented mechanical properties [69, 148, 149, 155-157]. Another significant factor is that many studies used bending loads to derive the skull bone's elastic modulus or ultimate strength [142-147]. It should be noted, however, that the skull's aforementioned composite structure [90, 148-150] and its notable curvature [142-147] make the results of these techniques difficult to interpret.

Table 6.1 Summary of previous studies on human skull bones

Bone	Age (yrs)	Loading type	Loading rate	Loading direction	*E* (GPa)	σ (MPa)
F, P [142]	81±11	B	0.5─2.5 m/s	R	7.46±5.39 (0.5 m/s)	─
F, P [70]	─	C	Quasi-static	R	1.4 (0.07─3.7)	36.5 (5.3─108.2)
F, P, O [69]	56─73	C	0.01 in/min	R	2.4 (SD: 1.4)	73.8 (SD: 35.2)
				A	5.6 (SD: 3.0)	96.5 (SD: 35.9)
P [143]	─	B	Quasi-static	R	9.7 (SD: 1.5)	─
F, P, T, O [144]	52─83	B	10 mm/min	R	5.2 (SD: 3.3)	
F, P, T [145]	52─95	B	10 mm/min	R	2.3─15.5	─
F, P, T [146]	~88	B	10 mm/min	R	0.9─9.3	─
F, P [147]	6	B	4─400 mm/s	R	3.69±0.92	27.18±9.23
P [71]	─	C	Quasi-static	R	─	25.1 (11.7─39.8)
F, P, O [72]	41─70	C	0.3─1.8 s^{-1}	R	0.45±0.14	23±6

Note: E = elastic modulus
F = frontal skull
P = parietal skull
O = occipital skull
T = temporal skull
σ = strength
C = compression experiments
B = bending experiments
R = radial direction
A = tangential direction

Quantitative investigation of tensile and compressive specimens of human cranium can be traced back to Evans and Lissner in 1957 [71]. The authors first studied the compressive ultimate strength of the through-the-thickness human parietal bone and suggested a slightly higher average strength of 167 MPa parallel to the through-thickness or radial direction, compared with average strength of 152 MPa perpendicular to the thickness direction, or in a tangential direction [71]. Later, Robbins and Wood measured the mechanical properties of human frontal skull and parietal skull in compression in the radial direction and reported an average elastic modulus and ultimate strength of 1.4 GPa and 36.5 MPa, respectively [70]. They also concluded that the human skull was a highly brittle and viscoelastic material based on the observation of a large amount of recoverable strain in the failed specimens [70]. In 1971, McElhaney et al. conducted a comprehensive investigation on the entire human cranial bone, where the strength, modulus, ultimate strain and energy to failure were provided in both the radial and tangential loading directions [69]. The researchers suggested that the skull bone is reasonably isotropic in directions tangent to the skull surface and their experimental results also found that large variation in the mechanical properties was primarily due to the large variations in the porosity and internal arrangement of the cancellous tissue, or diploë, between the cortical layers [69]. A recent study on the compressive response of human frontal, parietal and occipital skulls was conducted at comparatively higher strain rates (up to 1.8/s) and the mechanical properties again exhibited rate-dependency [72].

Those studies focused primarily on lower strain-rate behaviors whereas the cranial bone is regarded as a strain-rate dependent material. Although some research efforts were invested at higher loading rates, but the specimens were from either single cortical layer of the skull structure [90] or the infant skull bone [91], where the structure mainly consisted of a single cortical layer solely and largely different from the adult cranium. In addition, these studies provided no real-time observations of the deformation and failure processes in the skull specimens over the entire loading process to identify failure initiation and propagation at different loading orientations.

The objective of the present study is to visualize the *in-situ* dynamic failure processes of the human cranial bone under both radial and tangential compressive loadings and experimentally characterize the correlations between its mechanical properties and microstructures over a wide range of strain rates: quasi-static (<1/s), intermediate (1/s-10^2/s) and high strain rates (10^2/s-10^3/s).

6.3 Material & methods

6.3.1 Materials & Specimens

All the operations on the human skulls, including specimen preparation, transportation and mechanical characterization were in accordance with the Purdue University policy for use of human cadavers for research under the guidance of Purdue University Institutional Biosafety Committee. Human frontal skull bone specimens in approximately rectangular shape (Fig. 6.1) were prepared from the skulls of 3 fresh (non-treated) and frozen postmortem human subject (PMHS) donors (skull 11, skull 15 and skull 19). No history of diseases that could potentially change the mechanical properties of the skull was reported. The physiologic information of the donors and the number of prepared specimens are listed in Table 6.2.

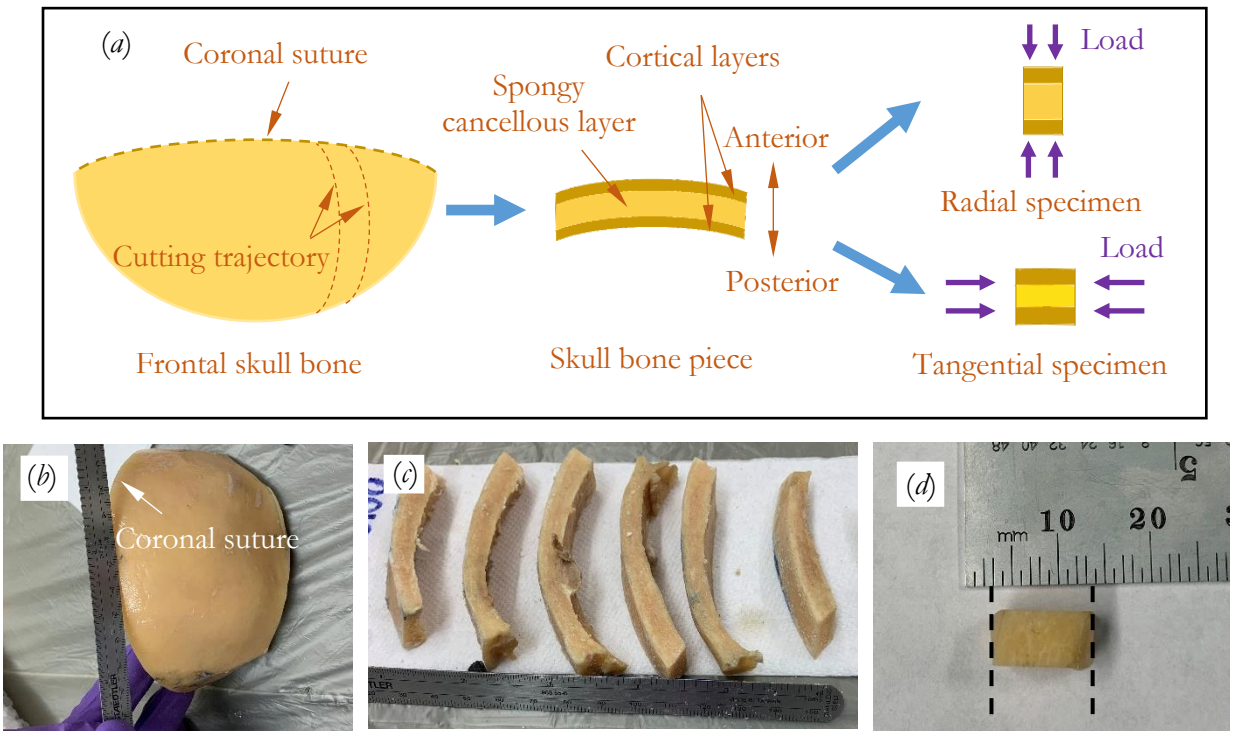

Figure 6.1 Human frontal skull specimen preparation (*a*) schematic of the specimen preparation (*b*) human frontal skull (*c*) human frontal skull pieces (*d*) a presentative specimen

A handheld bone saw was first used to dissect the whole frontal skull bones into multiple bone pieces perpendicular to the coronal suture (Fig. 6.1*a*). Specimens were then collected by further cutting those bone pieces through the skull's thickness direction (radial direction) using a precision

slow-speed diamond saw (IsoMet 1000; Buehler, IL, U.S.). The precision saw was cooled with water to reduce any potential damage during specimen preparation. All the specimens included the entire sandwich structure of the skull, with the outer and inner surfaces left intact, and they were selected randomly for experiments in the radial or tangential directions. The two cases for the tangential loading direction were not differentiated in this study since it was reported previously that the skull is reasonably isotropic in tangential direction [69, 90]. As shown in Fig. 6.1d, multiple images of each specimen were taken first with a dimension reference and then imported into the imaging processing software, Image J [158] to measure its dimensions before mechanical loading. The thickness of the specimen, also referred as the gage length, was measured as the distance from the inner surface, close to the brain, to the outer surface, close to the skin (Table 6.2). The height and width were measured to calculate the volumes or the cross-sectional area of the specimen. The nominal dimensions of the skull bone specimens in radial directions were ~7.2 mm in height, ~4.7 mm in width and ~7.9 mm in thickness, while the nominal dimensions of specimens in tangential direction were ~6.3 mm in height, ~4.8 mm in width and ~7.9 mm in thickness.

Table 6.2 The physiologic information of the donors and the number of prepared specimens

Skull	Sex	Age	Height (cm)	Weight (kg)	Thickness (SD) (mm)	*N* (radial)			*N* (Tangential)		
						0.01/s	30/s	625/s	0.01/s	30/s	625/s
11	Male	70	182	104	7.1 (1.5)	4	4	5	4	5	5
15	Male	73	170	67	10.0 (1.1)	5	4	5	-	-	4
19	Male	74	188	68	8.5 (1.8)	4	4	5	6	6	5

Specimens loaded in tangential direction were further polished with water-irrigated 800 grit silicon carbide paper such that the two cross-sectional surfaces cut by the precision saw were flat and parallel to each other for mechanical loading. Dental epoxy [70] was used to flatten the curved outer and inner cortical bone layers for those specimens such that these surfaces could bear the compressive load along the radial direction (Fig. 6.1*d*). Because of the limited number of specimens that could be prepared from the 3 skulls, a total number of 75 specimens was prepared all for compressive experiments in this study. For each case along the two loading directions (radial

and tangential) at the quasi-static (0.01/s), intermediate (30/s) and high (625±25/s) strain rates, at least four specimens from the same skull (except the tangential direction for skull 0015 at strain rate of 0.01/s and 30/s) were loaded under identical experimental conditions to ensure a sufficient specimen population (Table 6.2). Phosphate Buffered Saline (PBS) was used to keep the specimens fully hydrated during the entire specimen preparation and transportation.

6.3.2 Microcomputed tomography

Microcomputed tomography (micro-CT) was performed using an X-ray micro-CT scanner (Skyscan 1272, Bruker, MA, U.S.). A total of 16 specimens, with 8 from skull 15 and 4 from each of the other two skulls (skull 11 and skull 19) were selected randomly for tomography. The specimens were placed on a movable and rotational stage and imaging was conducted using energy in the range of 90─100 kV. A filter of copper with a thickness of 0.11 mm and a filter of copper/aluminum was used for the 100 and 90 kV X-ray source, respectively. The scanning parameters were chosen based on the condition of each specimen and listed in Table 6.3. It should be noted that, as X-ray radiation can potentially exert a deleterious effect on the mechanical behaviors of bone [60, 62], the specimens subjected to micro-CT scans were not applied for mechanical characterization in this study. The tomography reconstruction software and image analysis software were NRecon (ver. 1.7.1.0) and MATLAB (ver. R2016b).

Table 6.3 Micro-CT scanning parameters

Skull No.	Voxel size (μm)	Frames per step	Step rotation (°)	Random movement
11	7.5─8.0	6	0.3	19─20
15	6.5─7.0	5─6	0.3─0.35	21─23
19	7.5-8.0	6	0.3	19─20

6.3.3 Quasi-static & intermediate strain-rate experiments

Compressive experiments at quasi-static (0.01/s) and intermediate strain rates (~40/s) were performed using a hydraulically driven materials testing system (MTS 810). The MTS possesses a hydraulic power unit (HPU) charged accumulator which is capable of supplying high volumes of hydraulic fluid in a short time and therefore it is able to load the specimens at both quasi-static and intermediate strain rates. A linear variable differential transducer installed in the hydraulic

driven frame was used to measure the displacement of the actuator. The forces applied on the specimens were measured by a quartz piezoelectric load cell (Type 9212; Kisler, NY, U.S.). The load cell is capable of responding to loadings over a wide range of frequencies and hence could measure the loads during quasi-static and intermediate strain-rate experiments. A digital oscilloscope (MDO 3014, Tektronix, Oregon, U.S.) was used to record the displacement of the actuator and the force exerted on the specimen. The gage length for each of the compressive experiment was tuned according to the specimen's dimensions and the loading speed was modified accordingly to achieve a constant strain rate for all the tests. Petroleum jelly was used as a lubricant to reduce the friction between the specimen and fixtures.

6.3.4 High strain-rate experiments

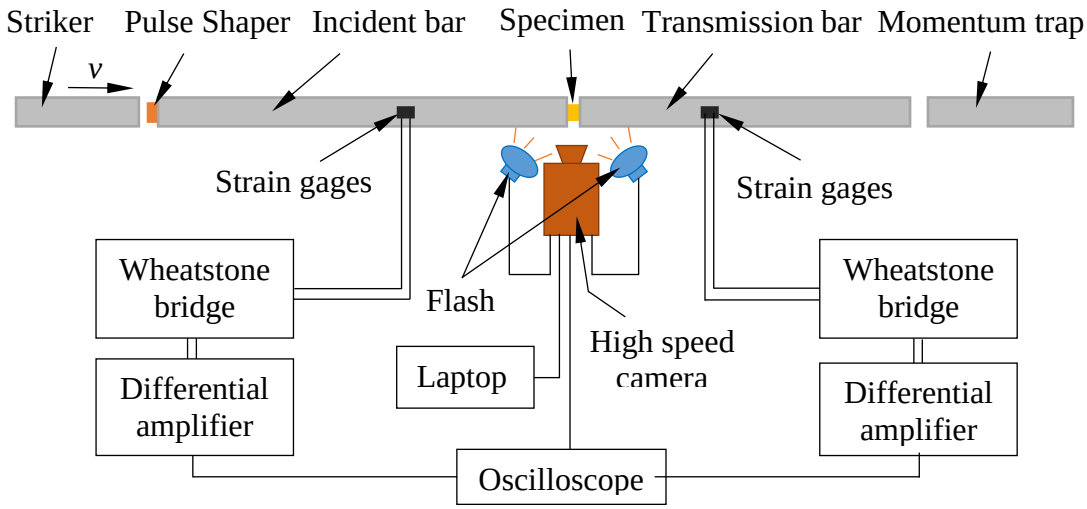

Figure 6.2 Schematic of the high strain-rate experimental setup on a Kolsky compression bar. When the striker impacts the incident bar, a compression stress wave shaped by the pulse shaper is generated and recorded by the strain gages on the incident bar, which is used to trigger the high-speed camera and flashlights. As the stress wave reaches the specimen, part of it reflects back while the remaining propagates further into the transmission bar through the specimen.

Experiments at high strain rates were conducted on an aluminum Kolsky compression bar (Fig. 6.2). The Kolsky bar had a diameter of 19 mm for all the striker, incident bar, transmission bar and momentum trap. The lengths of the incident and transmission bars were 3685 mm and 2134 mm, respectively. The specimen was fixed between the incident bar and the transmission bar. The momentum trap was used to absorb or trap the momentum generated by the impact of the striker to the incident bar after the stress wave propagated through the transmission bar to avoid any

potential interference in the measured signals. Similarly, petroleum jelly was used to reduce the friction at the interfaces between the specimen and bar ends. A pair of semiconductor strain gauges was attached on the surface of each of the incident bar and transmission bars to measure the strain pulses during the experiments. The strain gauges were connected in a half Wheatstone bridge configuration and then amplified by differential preamplifiers. The output of the strain pulses was recorded with the same digital Tektronix oscilloscope. An average strain rate of 625±25/s was controlled for all the dynamic experiments performed on Kolsky bar. Complete design and operational information of the Kolsky compression bar for experiments on brittle materials could be found in references by Chen and Nie [101, 159]. A high-speed camera (HPV-X2; Shimadzu, Japan) was used to document the entire loading process of the specimens, and different recording rates were used for the radial and tangential specimens due to the different failure mechanisms in the two directions. A frame rate of 500,000 frames per second (fps) was used for tangential specimens and 1,000,000 fps was used for radial specimens. A rising-edge output voltage signal from the high-speed camera was also recorded by the same oscilloscope to synchronize each of those recorded high-speed images to the stress and strain histories in the specimen.

A pulse shaping technique was adopted in this study to achieve a compressive pulse with a predetermined shape to ensure that the specimens were loaded in stress equilibrium state during the experiments [101]. By plastically deforming and hence damping the impact induced by the striker, the pulse shaper acted to create an incident stress wave with comparatively longer rising time, i.e., lower initial strain acceleration (the derivative of strain rate in terms of time) such that the specimen had sufficient time to reach stress equilibrium state. A detailed description of the mechanisms by which pulse shapers can be applied to experiments on Kolsky bars can be found in the reference by Chen [101]. In this study, copper disks with a thickness of 0.75 mm and a diameter of 6.35 mm were used as pulse shapers (Fig. 6.2). The stress, as determined by one-dimensional elastic wave propagation theory [101], was given by,

$$\sigma = \frac{A_B}{A_s} E_B \varepsilon_T \tag{6.1}$$

where σ is the stress of the specimen, A_B and A_s are cross-sectional areas of the bar and specimen, respectively, E_B is the elastic modulus of the bar material, and ε_T is the transmission signal. The strain is calculated by integrating the measured reflected signal with respect to time using Eq. (6.2) [101].

$$\varepsilon = -2\frac{C_B}{L_s}\int_0^t \varepsilon_R dt \tag{6.2}$$

where ε is the strain of the specimen, C_B is the elastic bar wave speed of the bar material, L_S is the gage length of the specimen, and ε_R is the reflected signal. The data reduction process of a typical skull bone specimen at high strain rates is shown in Fig. 6.3.

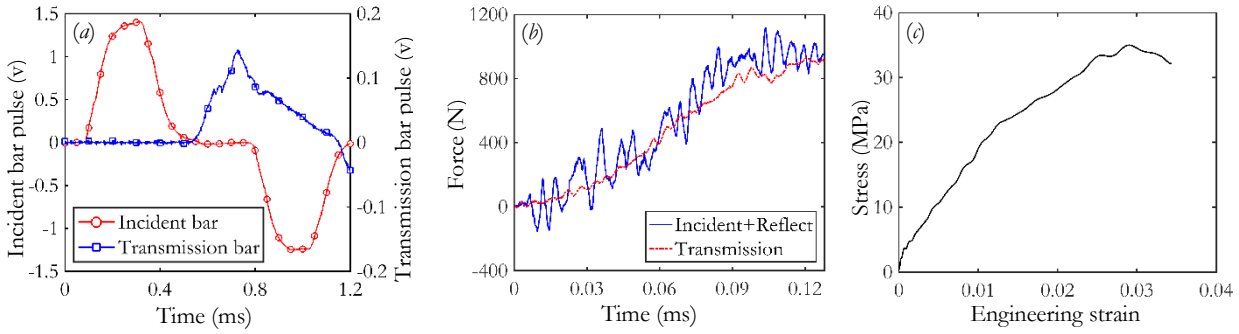

Figure 6.3 Data reduction of a representative radial skull bone specimen at a high strain rate (~650/s) (*a*) raw data measured by the strain gages on incident and transmission bars (*b*) stress at the front (incident + reflect) and back (transmission) ends of the specimen (*c*) stress-strain curve

6.3.5 Mechanical properties

The mechanical properties, including the ultimate strength (σ_U), ultimate strain (ε_U), apparent elastic modulus (E) and work to failure (W_f) were determined for all the specimens (Fig. 6.4). The maximum stress where a catastrophic failure took place was determined as the ultimate strength and the corresponding strain where the ultimate strength occurred were regarded as the ultimate strain. Apparent elastic modulus of each specimen was measured by first linearly fitting the elastic region of stress-strain curve, which was in the similar manner as that applied in previous study [70], and then averaging the gradients at all the points that are within ±15% of the fitting line's gradient. The work to failure was calculated as the area enclosed by the stress-strain curve until the failure of the specimen.

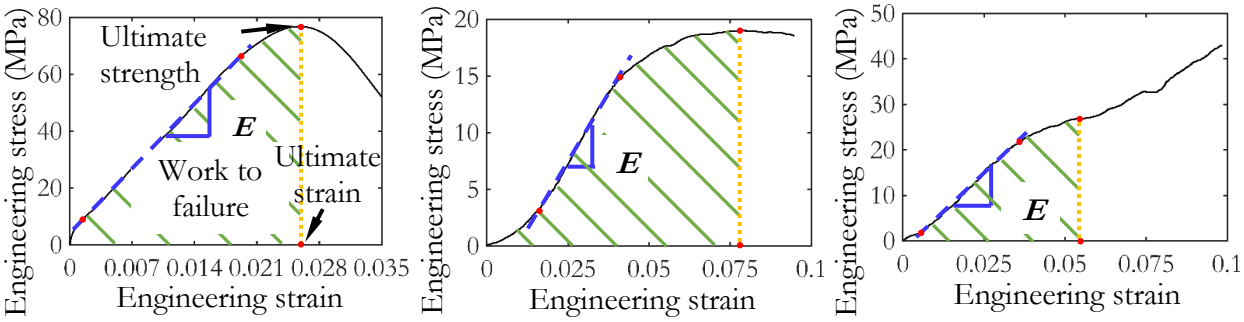

Figure 6.4 Determination of mechanical properties for three typical types of stress-strain curves

6.3.6 Statistics

An alpha level of 0.05 was used for all the statistical analysis in this study. Shapiro-Wilk (S-W) tests were conducted first to ensure the normality distribution of the data from specimens within each loading condition. A two-way analysis of variance (ANOVA) with post-hoc tests (Tukey) was performed for comparisons among the three loading rates and between the two loading directions. A one-way ANOVA with a post-hoc Tukey test was performed for comparisons of strength and apparent elastic modulus among the three skulls. *p*-Values larger than the alpha level was considered normally distributed for S-W tests while *p*-values less than the alpha level were regarded as statistically significant for the ANOVA test.

6.4 Results

6.4.1 Microstructure

From a representative three-dimensional tomographic image (Fig. 6.5*a*), the sandwich structure of the skull is apparent, and no predominant directions of the lamellae in diploë was observed (Fig. 6.5*c*). The thickness of each layer was determined (Fig. 6.5*b*) by the onset of the threshold porosity, as reported to be 30% in [160], and the average thickness and porosity for each layer was also determined for all the three skulls (Fig. 6.6) using the reconstructed two-dimensional tomographic images (Fig. 6.5*c*), where the images were colored solely for visual effect using DataViewer (ver. 1.5.3.4). The overall porosity of each layer of the three skulls was calculated by taking the average of all the scanned specimens from the same skull and the wet weight of each specimen was also measured using an analytical balance with a sensitivity of 0.005 g. Accordingly, the average wet structural density (apparent density) were determined using the

measured wet weight and calculated volumes, which were 0.4 g/cm^3 (SD: 0.04), 0.43 g/cm^3 (0.03) and 0.43 g/cm^3 (0.03) for skull 11, 15 and 19, respectively.

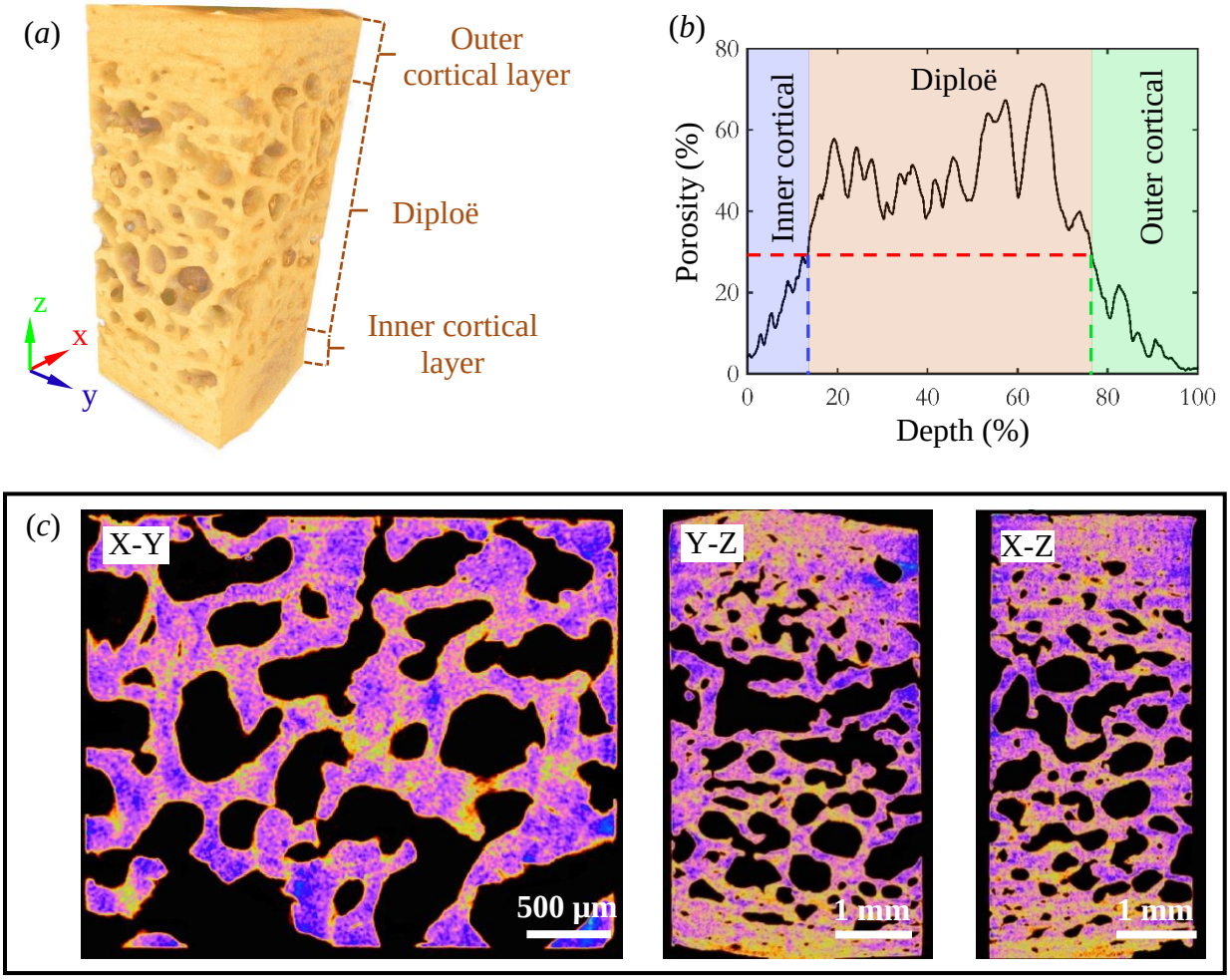

Figure 6.5 Topographical images of the human frontal skull specimen (a) 3D image (b) porosity distribution in through-the-thickness direction (c) 2D images in the three orthotropic planes at the center of the specimen

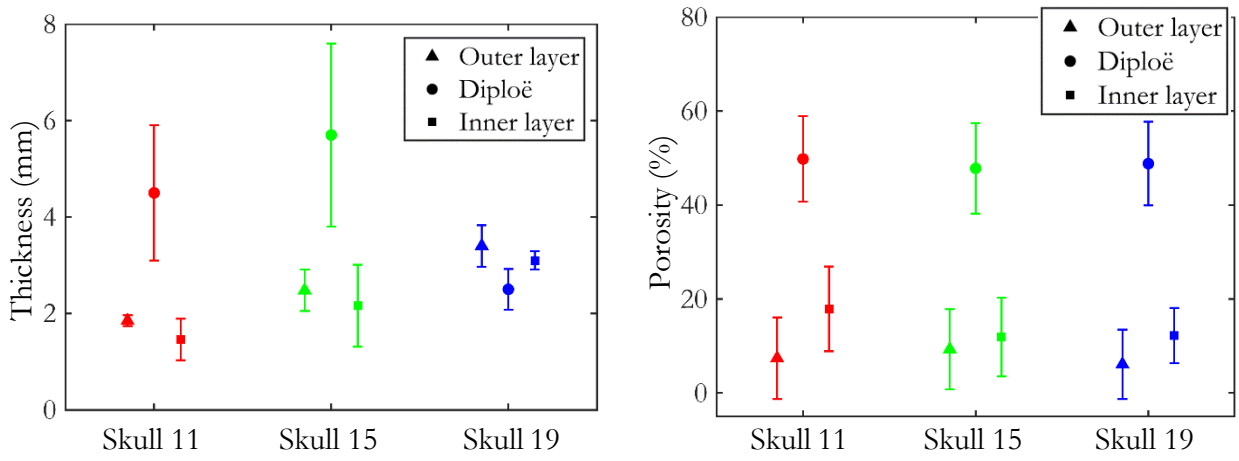

Figure 6.6 Thickness and porosities of each layer of the three skulls

6.4.2 Failure mechanisms

The real-time failure processes of five specimens at the high loading rate were recorded for each of the two loading directions: radial and tangential loading directions. The high-speed images of two representative experiments are provided in Fig. 6.7 and Fig. 6.8 for respective radial (1,000,000 fps) and tangential direction (500,000 fps). The failure mechanisms were consistent among specimens in same loading directions yet varied significantly between the two loading directions, as most of the specimens loaded radially crushed in the diploë section first while delamination was observed in specimens loaded along tangential direction. High-speed images (Fig. A5) of other representative specimens were also provided in appendix.

For a representative specimen at the radial direction (Fig. 6.7), the thickness of the entire structure of the specimen was aligned parallel to the axis of the Kolsky bar (horizontal in the images). In all the images, the incident bar and transmission bar were located on the left and right ends of the specimen, respectively. The crack first initiated at the bottom edge in the diploë and propagated along a direction of ~60° with respect to the horizontal direction (Fig. 6.7*b*). As the specimen was further compressed, a major structural crush occurred in the diploë (Fig. 6.7*c*) and subsequently two cracks initiated at the same time (Fig. 6.7*d*), with one major crack propagating toward the bottom and top edges of the specimen along a direction of ~48° (Fig. 6.7*e*). At the same time, cracks along the interface between the cortical layer and diploë were observed and the specimen ultimately failed by crushing into small pieces. The stress-strain curve for the representative radial specimen is also provided (Fig. 6.7*f*), where the stress-strain state in the

specimens corresponding to each high-speed image was also denoted on the curve. The peak stress and corresponding strain were ~42.1 MPa and 2.9%, respectively (Fig. 6.7*f*). It could also be seen that peak stress was reached in the specimen approximately at the crack initiation in the diploë.

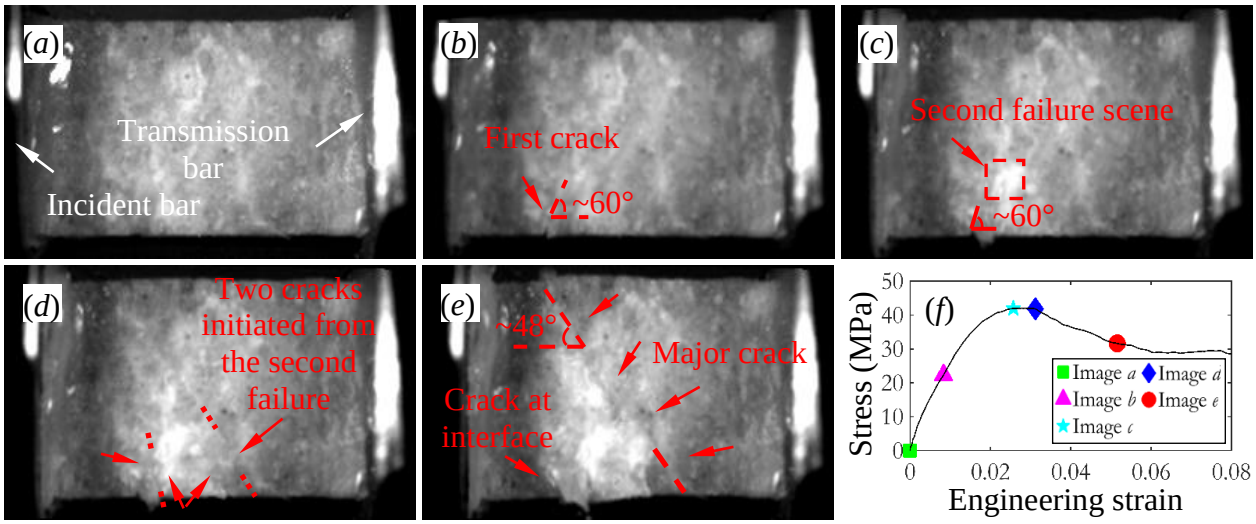

Figure 6.7 High-speed images showing the failure process in a representative skull bone specimen at radial direction (*a*) *t*=0 μs (*b*) *t*=56 μs (*c*) *t*= 89 μs (*d*) *t*=98 μs (*e*) *t*=130 μs (*f*) corresponding stress-strain curve

High-speed images for a representative specimen in the tangential direction are provided in Fig. 6.8. Similarly, the incident bar was on the left and the transmission bar was located on the right. The specimen was sandwiched between the incident and transmission bars such that its entire thickness was perpendicular to the axis of the Kolsky bar. As the loading started, two minor cracks appeared, with one in the diploë and the other one at the interface between the diploë and bottom cortical layer (Fig. 6.8*b*). As the incident bar further compressed the specimen, in an area close to the impact site, the bony tissue in the diploë was crushed first (Fig. 6.8*c*). Approximately at the same time, two additional cracks appeared, with one initiated in the top cortical layer and followed closely by the other one at its interface to the diploë (Fig. 6.8*c* and *d*). The two cracks then continued propagating towards the specimen's right end, separating the entire top cortical layer from the diploë and breaking the diploë into two parts, resulting in delamination of the sandwich structure (Fig. 6.8*e*). The stress-strain curve correlated with the stress state of each high-speed image for the representative tangential specimen showed that the specimen reached maximum

stress when the separation of the structure in radial direction took place (Fig. 6.8*f*). The ultimate strength and ultimate strain were 103.5 MPa and 3.4%, respectively (Fig. 6.8*f*).

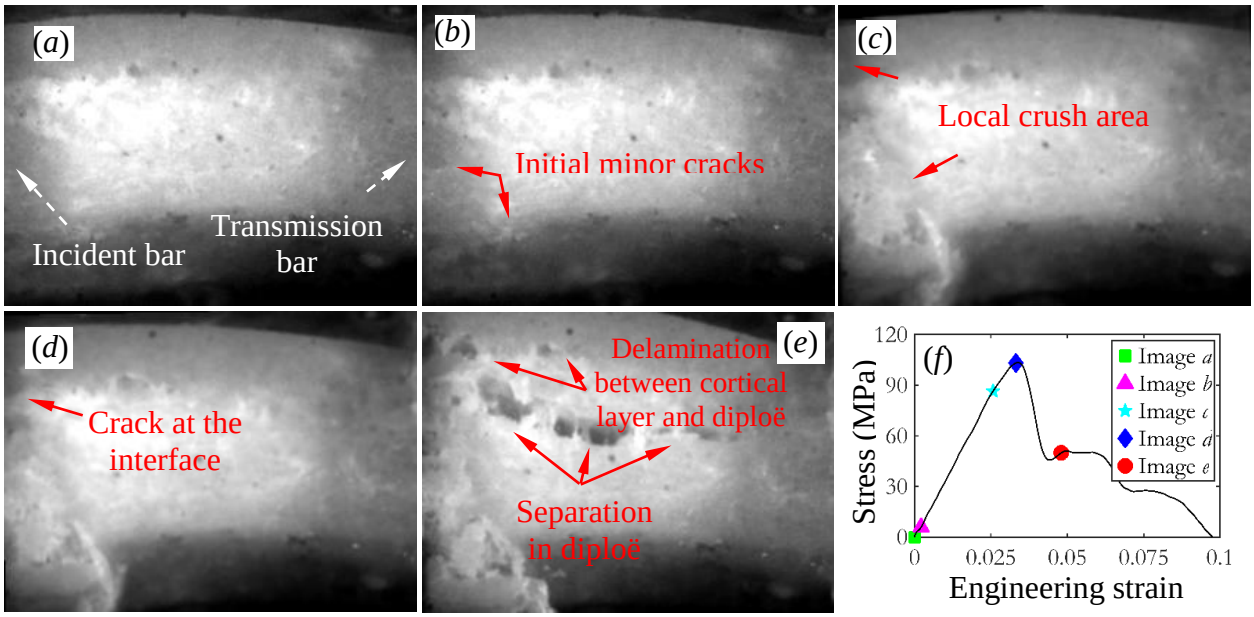

Figure 6.8 High-speed images showing the failure process in a representative skull bone specimen at tangential direction (a) t = 0 μs (b) t = 14 μs (c) t = 78 μs (d) t = 94 μs (e) t = 126 μs

6.4.3 Mechanical behavior

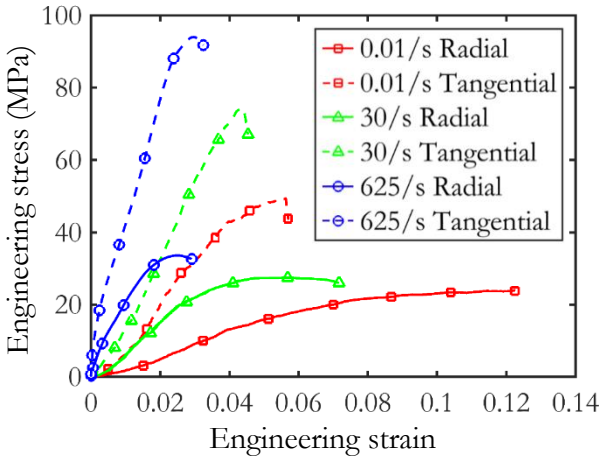

Figure 6.9 Stress-strain behaviors of representative human frontal skull specimens along radial and tangential loading directions at quasi-static, intermediate and high strain rates

The stress-strain curves of representative specimens under each loading condition (loaded over four decades of strain rates for both the radial and tangential loading directions) are presented in Fig. 6.9. The representative specimen was selected such that its mechanical properties were closest to the value of the average stress-strain curve of the corresponding loading condition. The stress-strain curves for all the specimens (Fig. A6) and the average stress-strain curves for each loading conditions (Fig. A7) are presented in the appendix for reference. Three types of stress-strain curves of human cranial bone at quasi-static loading rate reported previously [70] were also observed in our study (Figs. 6.4 and A6).

Stress-strain behaviors with an 'r' shape, typically seen in brittle materials, were observed for most of the skull specimens (Figs. 6.9 and A6) except for some specimens in the radial direction at lower strain rates that exhibited quasi-ductile behaviors. For lower strain rates (quasi-static and intermediate), the stress-strain curves mainly consist of a non-linear toe region, approximately linear elastic region, and followed by a 'creep' region or a region with an abrupt drop in stress, denoting the ultimate failure of the specimen (Figs. 6.9 and A6). At the high strain rate, a highly brittle stress-strain curve without an initial toe region is observed (Figs. 6.9 and A6), as the specimen failed in diploë after a short linear elastic region at relatively higher stress but lower strain. Overall, the stress-strain curve of the bone specimen shows a more brittle behavior as strain rate increases (Figs. 6.9, A6 and A7): the ultimate strength and elastic modulus increases but the ultimate strain decreases as the loading rate increases. Such strain-rate effect is apparent for both the loading directions across the quasi-static, intermediate and high strain rates.

The effect of loading direction was statistically significant on all the mechanical properties of human frontal skull bone in this study (Fig. 6.10 and Table 6.4). The effect of strain-rate was found varied among the different mechanical properties of human frontal skull bone (Table 6.4 for the *p* values of the statistics). Specifically, for ultimate strength, it increased significantly as strain rate increased from quasi-static to intermediate while showing no statistical significance as strain rate continued increasing to high rate. For both ultimate strain and elastic modulus, they displayed significant differences across the quasi-static, intermediate and high strain rates: the ultimate strain decreased while the elastic modulus increased as strain rate increased from quasi-static to high rates. No significant effect of strain rate on work to failure was observed as strain rate increased from quasi-static to intermediate rates nor did the work to failure significantly change as strain rate

increased from intermediate to high rates. However, it was significantly different between the cases of quasi-static and high strain rates.

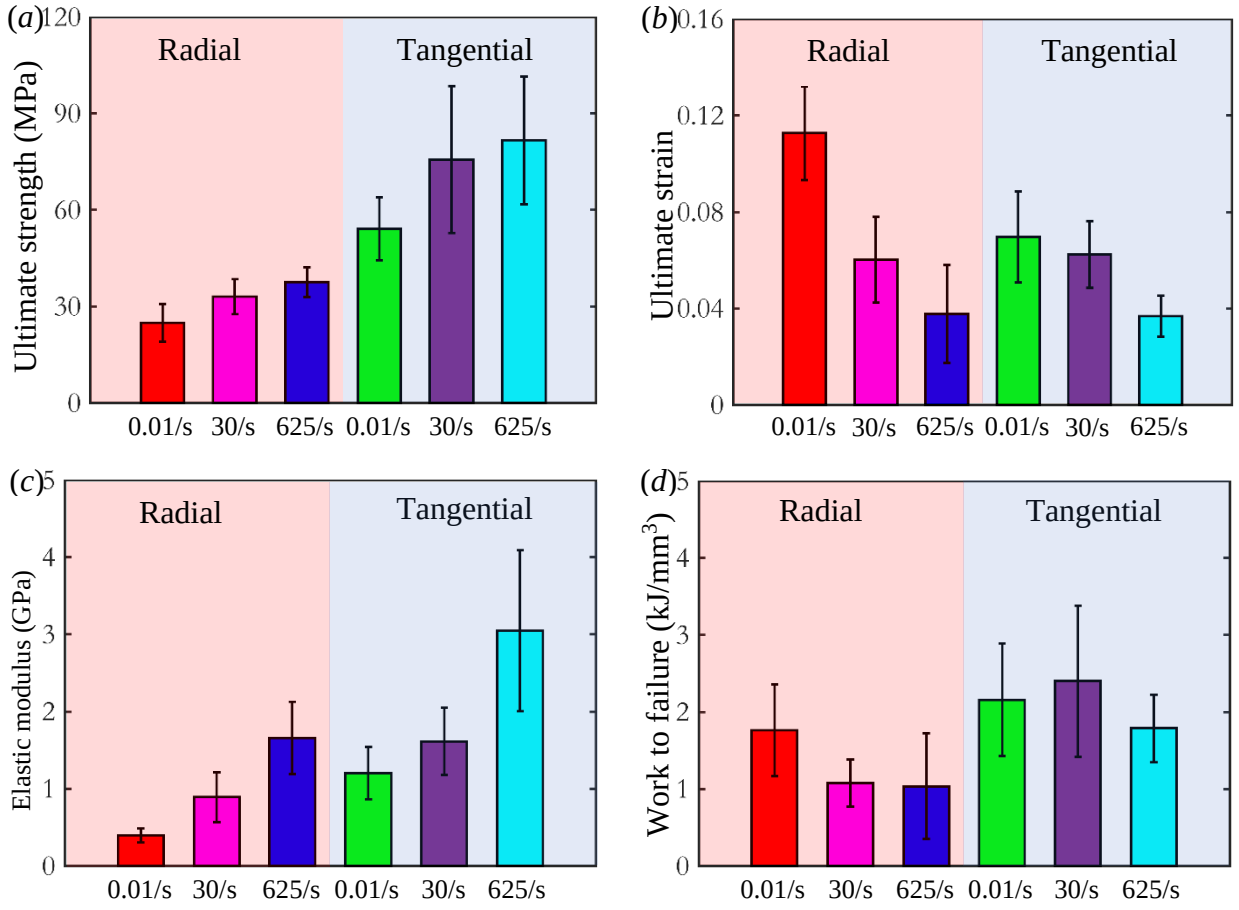

Figure 6.10 Mechanical properties (with SD) of the human frontal skull bone at quasi-static, intermediate and high rates for all the three skulls (*a*) ultimate strength (*b*) ultimate strain (*c*) elastic modulus (*d*) work to failure

Table 6.4 Statistical results for the comparisons of the skull's mechanical properties

	Properties	Q-I	Q-H	I-H	Direction	Interaction	Skulls	
							R	A
p	Strength	4.7×10^{-4}	7.6×10^{-6}	0.3	2.5×10^{-19}	0.1	0.66	1.3×10^{-3}
	Strain	1.1×10^{-8}	0	7.6×10^{-6}	3.3×10^{-4}	1.8×10^{-5}	-	
	Modulus	0.01	0	0	4.0×10^{-8}	0.07	0.19	0.13
	Work	0.5	0.01	0.2	1.2×10^{-6}	0.06	-	

Note: Q = quasi-static, I = intermediate, H = high. The definitions of all the other symbols are same as Table 6.1.

The stress-strain responses of both cortical bone layer and cancellous bone layer were determined using the stress-strain curve for each human skull specimen based on the simple mechanical models as shown in Fig. 6.11. For specimens loaded in radial direction, the stress applied on the cancellous bone layer was assumed to be same as the stress applied on the entire specimen and same among each of the three layers. Under the assumption that the cortical bone layers were incompressible as they were significantly harder and stiffer when comparing with the soft cancellous bone layer, the deformation of the entire radial human skull specimen was from the cancellous bone. Therefore, the strain of the cancellous bone layer could be hence reduced via dividing the deformation by the average thickness of the cancellous bone layer of the corresponding skull that was measured from the micro-CT (Fig. 6.6). When the specimen loaded in tangential direction, it was assumed that the cortical bone layers were the main load bearing structure and took all the load applied on the entire structure. The strain of the cortical bone layers for tangential specimen was same as the cancellous bone as well as the entire structure. Therefore, the stress-strain responses of cortical bone layers and cancellous bone layers for each skull could be estimated from the experimentally determined mechanical behaviors of the specimens.

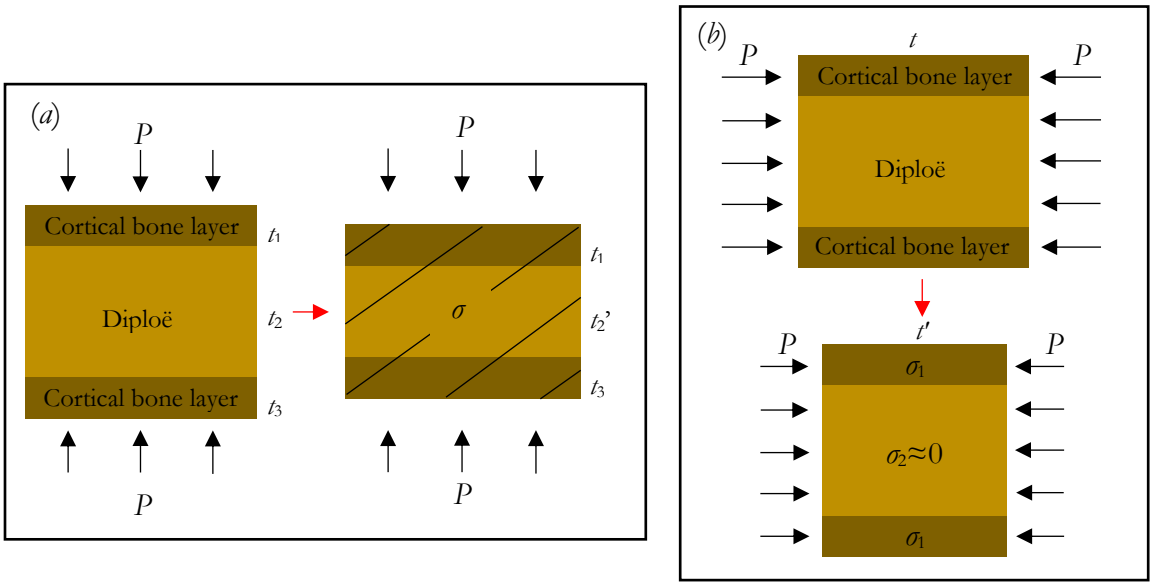

Figure 6.11 Simplified mechanical models for the mechanical behaviors of bone layers from human skull specimens (a) cancellous bone layer from radial specimen (b) cortical bone layer from tangential specimen

The average stress-strain curves of both cortical bone layer and cancellous bone layer at quasi-static, intermediate and high strain rates for all the three skulls were presented in Fig. 6.12. The mechanical behaviors of the two types of bone in human skulls were found to be highly strain-rate dependent: as stiffer stress-strain behaviors were observed for both the cortical bone and cancellous bone layers at higher strain rates (intermediate and high rates).

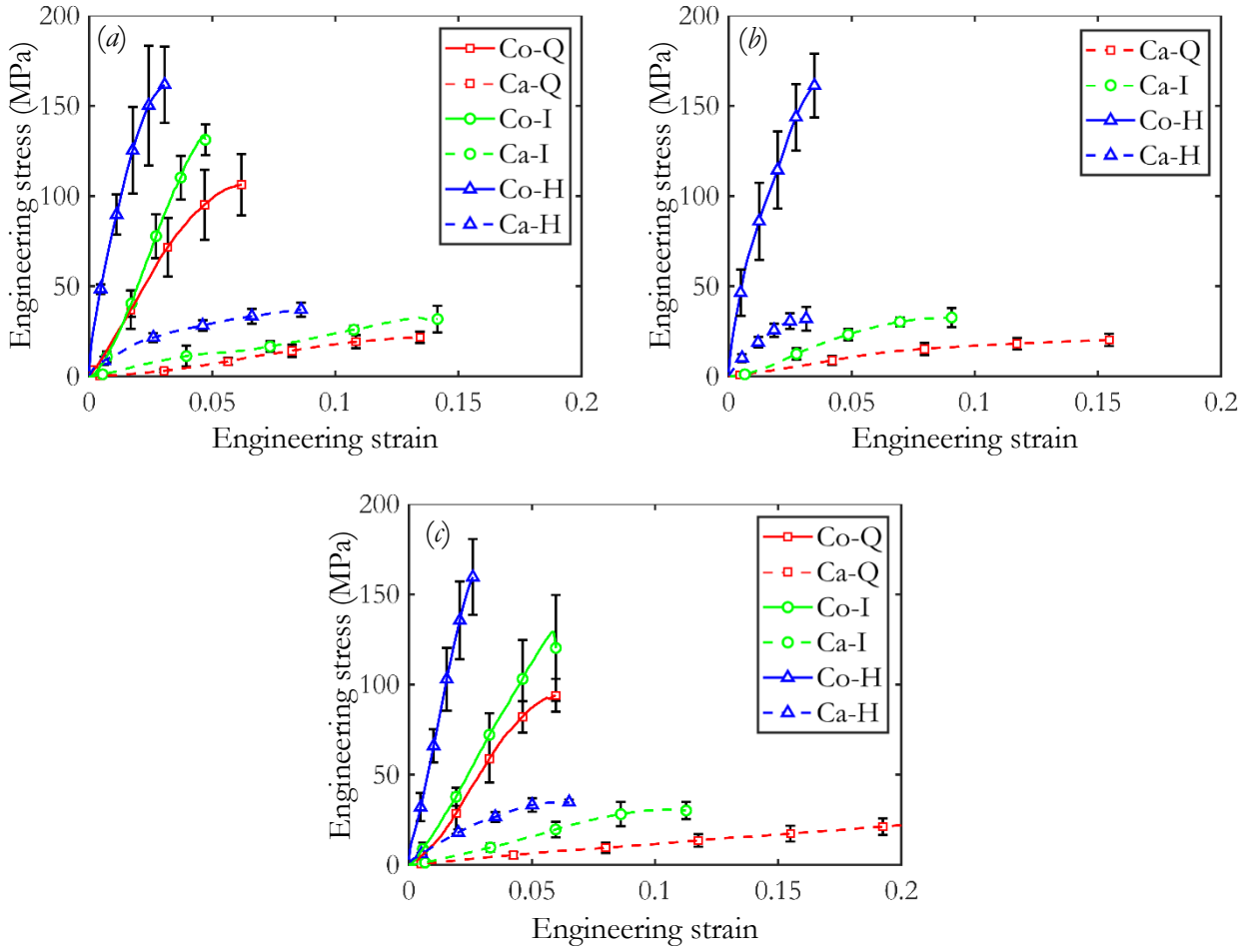

Figure 6.12 Average stress-strain curves (with standard deviations) for cortical bone and cancellous bone layers in human skulls at quasi-static, intermediate and high strain rates (a) skull 11 (b) skull 15 (c) skull 19 (Co: cortical bone layer, Ca: cancellous bone layer, Q: quasi-static rate, I: intermediate rate, H: high rate)

6.5 Discussions

It has been stated that the modulus and strength of the skull bone is correlated to its thickness or apparent ash density [48, 69, 151-154]. However, the apparent density is also dependent on both

the porosity and thickness ratios of each layer of the entire sandwich structure. In this study, for both the radial and tangential loading directions, no statistic difference in apparent elastic modulus were found among the three skulls (Table 6.4). This implies that the dominant factors in determination of the modulus are highly related to the diploë porosity, which is similar among all the three skulls. Although the strength is not significantly different among all the three skulls in radial direction it is statistically different in the tangential direction (Table 6.4). Specifically, skull's strength in radial direction could be highly related to the diploë porosity, while the thickness ratio of the diploë to the entire sandwiched structure plays an important role in determining the strength in the tangential direction (Fig. A8). For example, the average strength of skull 19 is 45 % higher than that of skull 11 in tangential direction and the diploë ratios for skull 11 is twice that of skull 19, suggesting that strength is related to diploë ratio (Figs. 6.6 and A8). Studies on more skull subjects are needed in future to verify these observations to conclusions.

Owing to the sandwich structure of the human skull (as shown in Fig. 6.5), the human skull specimens failed with different mechanisms (Figs. 6.7 and 6.8) depending on the loading direction, resulting in different mechanical behaviors in the two directions. For example, in the radial direction under high loading rate (Fig. 6.7), the specimen failed in the diploë in compression presumably in shear (Fig. 6.7e) when the first stress wave reached and propagated in it. For the tangential loading direction (Fig. 6.8), although there was a local initial crush in the specimen (Fig. 6.8c), it subsequently failed due to the separations of the diploë layer and delamination between the diploë and cortical layers (Fig. 6.8d, e). The specimens also failed through similar mechanisms at quasi-static and intermediate strain rates in both the loading directions (radial and tangential) as similar failure types were observed in the postmortem specimens as presented in Figs. A3 and A4. It also should be noted that, the failure mechanisms observed in the high-speed images in this study were based on the visualization of the loading processes at the surface of the specimens.

Most of the specimens exhibited brittle stress-strain curves at intermediate and high strain rates along both the radial and tangential loading directions (Fig. 6.9). In the radial direction especially at quasi-static rate, ductile-like stress-strain curves were found for some specimens while others exhibited brittle behaviors (Fig. A6). The plastic deformation or buckling of the trabeculae in diploë can be a reason for such observed ductile behaviors of the skull. An initial toe region that was specific for lower strain rate case occurred less frequently in specimens loaded at high strain rates, especially in the tangential direction (Fig. A6). Such toe regions were likely a result of the

plastic deformations or buckling of some trabeculae in diploe layer. As the strain rate increased from quasi-static to high rates or the skulls were loaded in tangential direction, the less frequently occurring toe region indicated that the skulls were more brittle at higher rates as well as in tangential loading direction.

The mechanical properties of the human skull bone could be strongly direction dependent as the failure mechanisms were entirely different in the two loading directions. The ultimate strain is smaller at quasi-static strain rate and it takes more work to fail the specimen in tangential direction at intermediate and high rates. For example, at high strain rate, the work to failure in tangential direction is approximately twice of that in radial direction (Fig. 6.10). In addition, the largest increasing ratios of tangential to radial loading direction are as high as 2 and 3 for strength and modulus (Fig. 6.10), respectively, which indicates a more brittle mechanical behavior in the tangential direction. Such higher compressive ultimate strength and modulus yet smaller ultimate strain along tangential loading direction than radial direction at quasi-static strain rate (0.01 in/min) were also reported in the literature [69]. However, at quasi-static loading rate, no significant difference in work to failure between the two loading directions was found in this study and similar results was also reported in [69].

The effect of loading rate in the range of quasi-static rate on the mechanical behaviors of human bone has been investigated in the literature and a transition from ductility to brittleness was reported [10, 33, 74, 90]. Such a trend in human cranial bone in this study was also observed over the quasi-static, intermediate and high strain rates: the specimen shows an increasing brittleness as strain rate increased. The loading rate effect is succinct on all the mechanical properties as the strain rate increases from quasi-static to high strain rates (Fig. 6.10 and Table 6.4), with the elastic modulus and ultimate strain varies vastly across all the three rates. For example, the elastic modulus increased by a factor of 4 across the quasi-static, intermediate and high loading rates along radial direction and it increased by a factor of 2.5 along tangential direction (Fig. 6.10). A significant difference in ultimate strength was observed between quasi-static and intermediate strain rates and work to failure was statistically different between quasi-static and high strain rates.

Table 6.5 lists the previously determined mechanical properties of human cortical and cancellous bones for comparison with our results (marked with star in the first row) [47, 71, 134, 148-150, 161, 162]. As seen, the strength of human frontal skull bone at the quasi-static strain rate obtained in this study agrees with those reported in [69-72] (Table 6.1). It is also found both the

strength and elastic modulus of the skull are lower than those of cranial bone's cortical layer [71, 148-150]. This indicates that the trabecular bone plays an important role in determining the mechanical properties of the entire cranial bone structure. However, the strength of cranial bone specimens is higher than that of the trabecular bony tissue extracted from human vertebra and long bones [47, 161, 162], which could imply that the strength of the diploë is higher or there is a strengthening effect of the entire sandwiched structure. It also should be noted that the elastic modulus presented here falls in the range provided in [70, 72] (Table 6.1) while it is lower than those in [69] (Table 6.1).

Table 6.5 The mechanical properties of human cortical and cancellous bone tissues at quasi-static rates

Bone location	Type	Age (yrs)	Rate	Direction	E (GPa)	σ (MPa)
F *	Entire structure	70─74	0.01 s^{-1}	R	0.39 (SD: 0.09)	25 (SD: 5.8)
				A	1.2 (SD: 0.34)	54 (SD: 10)
P [148]	Cortical	58─88	─	─	10.6─21	─
F, O, P, T, Z [149]	Cortical	27─100	─	3D	10.4─23.4	─
F, P, O, T [150]	Cortical	41-70	4 s^{-1}	A	12.01±3.28 (Tensile)	64.95±21.08 (Tensile)
P [71]	Cortical	─	─	R	-	166.4 (31.0─323.4)
				A	-	152.5 (85.5─329.6)
Vertebral [161]	Cancellous	15─87	2 mm/min	V	0.067 (SE: 0.007)	2.45 (SE: 0.24)
				L	0.020 (SE: 0.003)	0.88 (SE: 0.12)
Vertebra and long bones [162]	Cancellous	31─69	0.01 s^{-1}	3D	0.001─1.5	0.1─16
Proximal tibia [47]	Cancellous	42─76	─	─	0.49 (SD: 0.33)	2.22 (SD: 1.42)
Femoral neck [134]	Cancellous	51─85	0.005 s^{-1}	R	18±2.8	135.3±34.3

Note: 3D = three orthotropic directions, L = horizontal, V = vertical, Z = zygomatic skull. The definitions of all the other symbols are same as those in Table 6.1.

The effect of strain rate is also apparent in the stress-strain behaviors for both cortical bone and cancellous bone layers that determined from the resultant compressive mechanical behaviors of entire human skull structure using the simplified models (Figs. 6.11 and 6.12). For all the three

skulls, when strain rate increases from quasi-static to intermediate first and then to high rates, the strength and elastic modulus increase while the ultimate strain decreases for both cortical bone and cancellous bone layers, showing transitions from quasi-ductile to highly brittle in their mechanical behaviors. For example, the strength of cortical bone layer for skull 19 increases 76% and the corresponding increasing ratio is 30% for its cancellous bone layer. The strength of cortical bone layer at quasi-static strain rate obtained in this study are found fall in the range of strength of human skull's cortical bone layers that determined previously in literature. It also should be noted that, the mechanical behaviors for the cortical bone and cancellous bone layers in human skulls in this study are solely rough estimations. Significant errors (Fig. 6.12), potentially originating from the applications of ideal mechanical models and average human skull's structural properties, could be generated in deducing the stress-strain curve of either the cortical bone layer or cancellous bone layer for all the three skulls.

6.6 Conclusions

In this study, the compressive mechanical behaviors of human frontal skull bone were characterized along radial and tangential loading directions at quasi-static (0.01/s), intermediate (30/s) and high strain rates (625/s). The entire *in-situ* failure process of the specimens at high strain rate was also visualized for both the loading directions. Specimens were crushed in the diploë and failed presumably along the maximum shear stress direction when loaded along the radial direction. On the other hand, separation of the entire bone structure was observed as the main failure mechanism for specimens loaded in the tangential direction. The mechanical properties of human cranial bone were both loading direction dependent and strain rate sensitive. Stiffer mechanical behaviors were observed in the tangential loading direction than in radial direction, with increasing ratios of 2 and 3 for strength and modulus, respectively. For both the loading directions, the ultimate strength and elastic modulus of the specimen at high strain rate were significantly higher while the ultimate strain is smaller than that at quasi-static strain rate, demonstrating an increasing brittle mechanical behavior as the strain rate increases. The mechanical properties of the skulls in both the loading directions were dependent on the diploë porosity more significantly while the modulus was found to be more sensitive to diploë ratio in tangential direction. Estimations simply based on ideal mechanical models and average skull structural properties showed that the

mechanical behaviors of both cortical bone layers and cancellous bone layers were strain-rate dependent.

CHAPTER 7. THE EFFECTS OF LOADING-DIRECTION AND STRAIN-RATE ON THE MECHANICAL BEHAVIORS OF HUMAN FRONTAL SKULL BONE

Adapted from:
X. Zhai, Y. Nie, J. Gao, N. Kedir, B. Claus, T. Sun, K. Fezzaa, W.W. Chen. The effect of loading direction on the fracture behaviors of cortical bone at a dynamic loading rate, Journal of the Mechanical and Physics of Solids. Under review.

7.1 Abstract

In this study, the dynamic cracking processes in porcine cortical bone were visualized in real-time using the high-speed synchrotron X-ray phase-contrast imaging (PCI) technique in three osteon orientations: in-plane transverse, out-of-plane transverse and in-plane longitudinal. The dynamic flexural loading applied on the pre-notched bone specimens was introduced by a modified Kolsky compression bar. High-speed X-ray images of the entire loading events were documented with a high-speed camera. Three-dimensional X-ray micro-computed tomography was conducted to examine the intact microstructures and obtain the basic material properties of the bone material used for mechanical characterizations. The onset location, where crack initiated, and the subsequent direction, along which the incipient crack propagated, were measured quantitatively using the high-speed X-ray images and the latter was found dependent on the osteon direction significantly. The crack propagation velocities were dependent on crack extension over the entire crack path significantly for all the three directions while the initial velocity for in-plane longitudinal direction was lower than the other two directions. Straight-through crack paths were observed for in-plane longitudinal specimens while the cracks were deflected and twisted in the in-plane transverse direction. For out-of-plane transverse direction, the cracks follow paths with tortuosity fall in between the other two directions, showing a mixed mode of fractures of the former two extreme cases. The toughening mechanisms, visualized by the high-speed X-ray images, and the corresponding fracture toughness, evaluated in terms of fracture initiation toughness and crack growth resistance curve (*R*-curve), were also found significantly different among the three osteon directions, suggesting an overall transition from brittle to ductile-like fracture behaviors at the dynamic loading rate (5.4 m/s) as the osteon orientation varies from in-plane longitudinal to out-of-plane transverse, and to in-plane transverse eventually.

7.2 Introduction

Built as a hierarchical assembly of collagenous protein and minerals in multiple length scales [1-4], bone is found to be a tough, adaptive and self-remolding yet lightweight material in nature. It serves as not only a loadbearing framework of the body, but also a protective gear for the inner vulnerable soft tissues. In recent years, the fracture toughness of bone, especially at dynamic loading rates, (> 1 m/s) is of increasing interests for researchers attempting to model the cracking in bone that mostly associated to impact events, such as car collisions or sports accidents [4].

It is believed that the crack initiation or propagation is energetically favorable when the elastic energy gained by the advance of a crack is no less than the energy required for an additional new crack surface [163, 164]. Therefore, the more energetic gain needs for cracking, the more toughening mechanisms (or energy dissipation) exist, and the more difficult it is to fracture a material. In reality, microscopic cracks are always largely distributed in bones, but the hierarchical features in its structures develop various toughening mechanisms (Fig. 7.1) [42, 73, 76, 77, 83, 163-171], ranging from nanoscopic to macroscopic length scales, making them remarkably resistant to cracking [163].

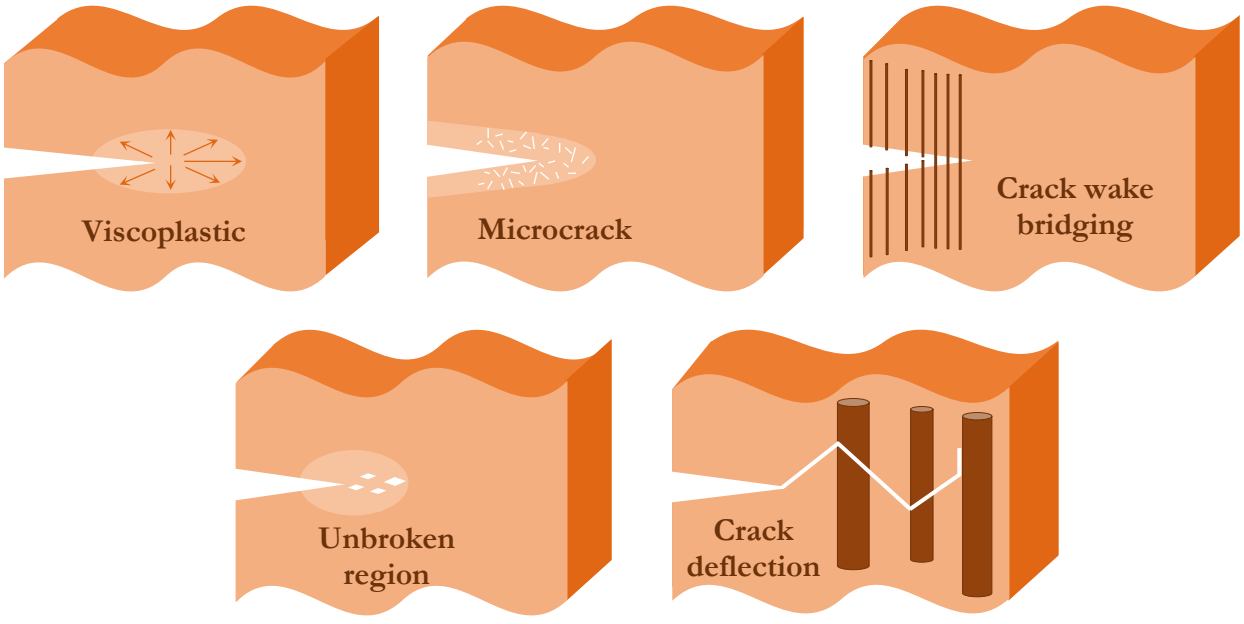

Figure 7.1 Mechanisms of toughening developed in bone

As a typical toughening mechanism at the nanoscale, viscoplastic flow near the crack tip, owing to the ‘sacrificial bonds’ in collagen fibrils, dissipates the strain energy used for creating a new fracture surface and thus functions as a mechanism of toughening in bone [42, 73, 164]. Moreover, the formation of microcracks at nanoscopic length scales dilates the area around the major crack tip, compressing the crack from further propagation effectively and acting as a toughening mechanism [42, 163, 165]. It is also found that such microcracks, ahead of the main crack, plays a critical role for the development of other toughening mechanisms in macroscopic scale, notably crack bridging and crack deflection, typically at scales of few microns and above [42, 83, 166, 167]. Specifically, crack bridging is associated with the unbroken collagen fibrils that bridge the gap in the crack wake and therefore increases the driven force necessary for further crack extension, acting as a toughening mechanism in bone [42, 76, 77, 163, 165, 168, 169]. It is also proposed that unbroken region between a major crack and other minor cracks initiated in front of it plays a role in consuming the driving force otherwise applied to develop the crack, which regarded as a common crack-resistance mechanism (unbroken-region bridging or uncracked-ligament bridging) in bone [76, 77, 83, 163, 165, 168, 170]. Particularly when crack propagates perpendicular to osteons, crack deflection or twist, as deviation from the direction of maximum tensile stress, tends to occur at the interlamellar boundaries (inside the osteons) or the cement lines (between osteons and interfaces), which reduces the local stress field, necessitates the reinitiation of the crack following local arrest, and correspondingly increases the toughness significantly [42, 76, 77, 163, 165, 171]. These toughening mechanisms in bone are found dependent on crack propagation direction significantly as a consequence of its anisotropic microstructures, which in turn results in the largely varied fracture toughness in different osteon orientations. For example, previous studies found that bone is more difficult to break than to be split, i.e., bone is much tougher when the crack propagates perpendicular to the axis of the osteon rather than parallel to it [76, 83, 165]. The main reason behind why this fact is that, in transverse loading direction, the crack must penetrate through the osteons and hence the crack deflection or twist at the cement lines, one of the most effective toughening mechanisms found in bone, plays the predominant role.

Although there has been indeed a large amount of studies investigating the fracture behaviors of bone [42, 73-77, 83, 115, 163-172], most of them aimed at either the transverse-to-fiber direction or the quasi-static loading rates [42, 76, 83, 131]. However, bone’s fracture behaviors are found to be not only anisotropic [42, 76, 83, 131-133, 172], but also regarded as a rate-sensitive

[30, 33, 49, 52, 58, 59, 74, 89, 115] property. Specifically, when loading rate increases, the fracture toughness of bone diminishes and less tortuous crack surfaces are observed, suggesting an increasingly brittle fracture [33, 52, 58, 59, 74, 89]. In addition, most of the data for fracture toughness of bone in literature were available only in terms of a single parameter, such as fracture toughness, K_c, or the strain energy release rate, G_c. While it is appropriate using K_c or G_c to evaluate the fracture toughness for many materials, the resistance to fracture in bone actually increases as crack propagates in most of the cases, which therefore requires a resistance-curve (*R*-curve) fracture-mechanics approach [77]. Accordingly, in this study, we evaluated the *R*-curve behaviors of porcine cortical bone in three osteon orientations at a dynamic loading rate and visualized, in real-time, the entire dynamic fracture processes to identify the corresponding toughening mechanisms.

7.3 Materials and methods

Single edge notched bend (SENB) porcine cortical bone specimens were prepared for the dynamic three-point bending experiments. Micro-computed tomography (micro-CT) was conducted to obtain the basic material properties of the bone materials. A modified Kolsky compression bar was used to apply the dynamic three-point bending loading to the specimens and the entire in-situ fracture event was imaged using the synchrotron X-ray PCI technique. By synchronizing the load histories and the high-speed X-ray images, the fracture toughness of the cortical bone specimens was determined in terms of the critical stress intensity factor for mode-I fracture. A scanning electronic microscope (SEM) was used to take images of the fracture surfaces and crack path profiles of the postmortem specimens. Introductions of the specimen preparation and descriptions of all those experimental methods mentioned above are presented separately in this section.

7.3.1 Materials

Fresh porcine cortical bone from the femur of a 2-year-old Yorkshire female swine was collected right after it was slaughtered. The swine was raised by the Department of Animal Sciences at Purdue University. We prepared the cortical bone specimens following the methods introduced with detailed information in reference by Zhai [173, 174]. The average thicknesses, *B*, widths, *W*, and lengths, *l*, of all the specimens were ~0.81 (SD: 0.06) mm, ~3.0 (SD: 0.1) mm, and

~16 (SD: 0.2) mm, respectively. The specimens were also pre-notched with the root radius, *r*, of ~170 μm and initial depth, ρ of ~1.4-1.6 mm. Specimens in three osteon orientations (anatomical locations), in-plane transverse, out-of-plane longitudinal and in-plane longitudinal were prepared:

in-plane transverse (medial-lateral) ─ the nominal direction of the notch is in the plane of the osteons but perpendicular to long axes of the osteons,

out-of-plane transverse (anterior-posterior) ─ the nominal direction of the notch is out of the plane of the osteons and perpendicular to the long axes of the osteons,

in-plane longitudinal (proximal-distal) ─ the nominal direction of the notch is in the plane of the osteons and parallel to the long axes of the osteons.

A total number of 25 specimens, with 9 for in-plane longitudinal direction and 8 for both the other directions, were prepared in this study. The specimens were not pre-cracked as the pre-cracking process would probably induce the toughening effects and bring more stress uncertainties before mechanical characterizations [58]. Phosphate Buffered Saline (PBS) was used to keep the specimens hydrated during their preparation and transportation. All the operations on porcine bones were in accordance with the policy for use of animal subjects for research under the guidance of Purdue University Institutional Biosafety Committee. A schematic illustrating the specimen preparation is provided in Fig. 7.2.

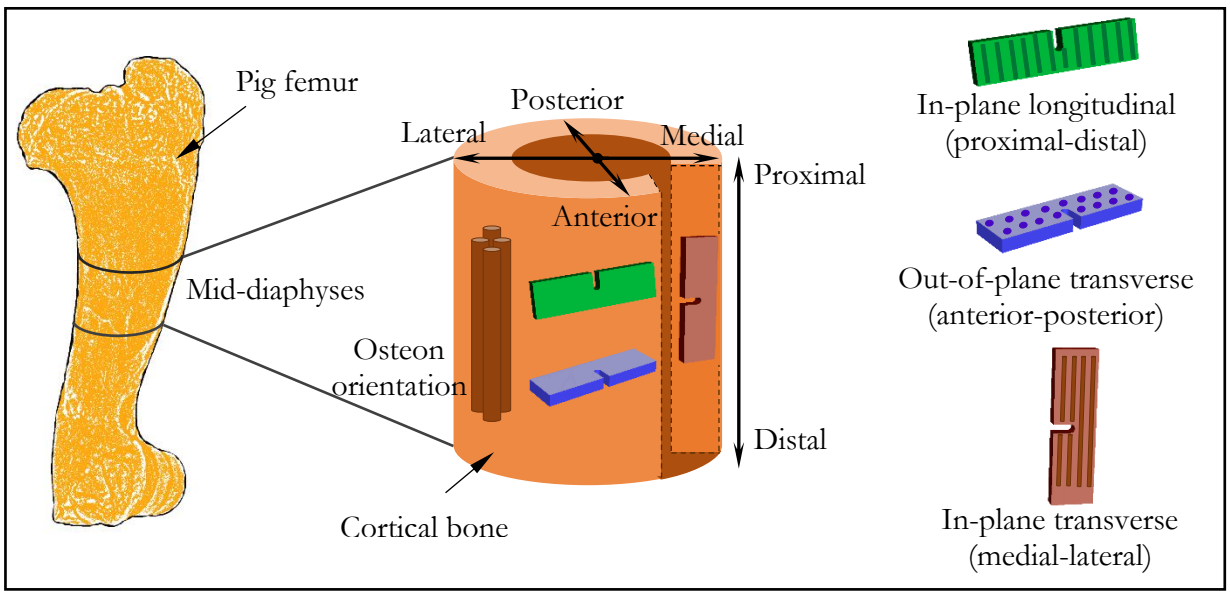

Figure 7.2 Schematic of the bone specimen preparation

7.3.2 Three-dimensional X-ray micro-computed tomography

To obtain the intact microstructures of the porcine cortical bone used in this study, three-dimensional computed tomography was performed using an X-ray micro-CT scanner (Skyscan 1272, Bruker, MA, U.S.). Two specimens from each of the three directions were selected randomly for micro-CT and they were not applied for mechanical characterizations due to the potential deleterious effect of the X-ray radiation [60, 62]. The specimens were mounted on a movable and rotational stage where the X-ray, with an energy level of 80 kV, penetrated through to obtain the microstructures in the potential cracking regions of the specimens. A filter of 1 mm thick aluminum was used for the scans. For all the micro-CT scans, the resolution was 4904 × 3280 in pixels , and the resultant voxel size was controlled to be 0.9 μm, respectively. Despite the highest resolution was applied, the micro-CT scan was performed within a band region (~4.4 mm × 3.0 mm), where the notch was enclosed and fracture took place, rather than the entire specimen.

7.3.3 Integration of modified Kolsky compression bar and synchrotron X-ray PCI

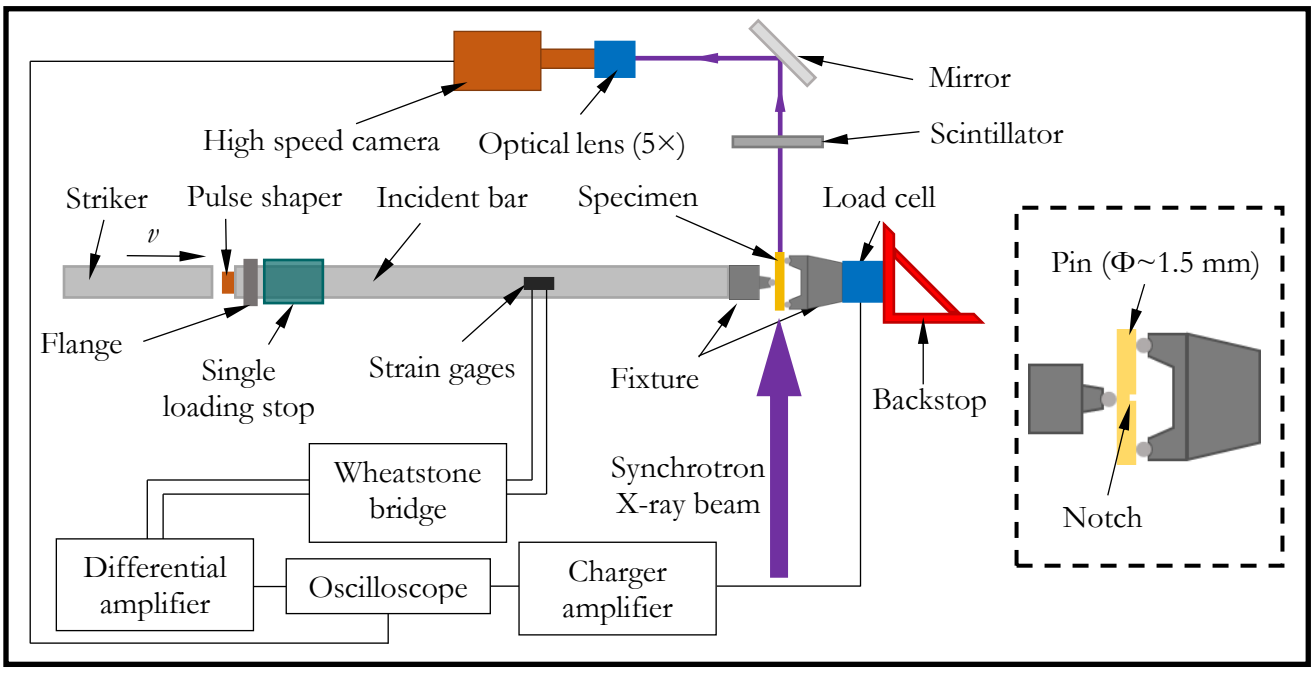

Figure 7.3 Schematic of the experimental setup in X-ray hutch at APS beamline 32 ID-B

The inherent advantages using the experimental technique that combines the synchrotron X-ray PCI and Kolsky bar were introduced in our previous works [101, 119-123, 173, 174]. The same experimental technique, as illustrated by a schematic in Fig. 7.3, was also used in this study to

apply the dynamic three-point bending loadings and to record, at the same time, the entire cracking processes in the 19 specimens (N=7 for 9 for in-plane longitudinal direction, and N=6 for both the in-plane transverse and out-of-plane transverse directions). Because the X-ray beam size is limited within 2.2 mm × 2.0 mm, specimens with smaller dimensions than those used in our previous works [173, 174] were prepared here to obtain the full views of the entire crack paths in the high-speed X-ray images. Correspondingly, a pair of fixtures for three-point bending experiments with smaller configuration was designed. The one-point loading steel fixture was connected to the incident bar and the two-point support steel fixture with a span (S) of 12 mm was mounted on the load cell. A recording frame rate of 1,000,000 frames per second (fps), with a temporal resolution of 1 μs, was used for one in-plane transverse specimen, two out-of-plane transverse specimens and one in-plane longitudinal specimen to record the fracture process with longer time duration of camera action. A higher recording frame rate of 5,000,000 fps was used for all the other specimens and the temporal resolution were accordingly 200 ns for the X-ray images. The spatial resolution of all the high-speed X-ray images was estimated to be 6.4 μm/pixel and the frame was 400 pixels wide and 250 pixels high.

The velocity and displacement at the sample end of the incident bar were reduced using the recorded incident and reflected strain pulses by applying the equations found in references by Zhai and Chen [173].

7.3.4 Fracture toughness

The crack extensions during the entire cracking process in each specimen were determined using the recorded high-speed X-ray images. The corresponding fracture toughness, in terms of the stress intensity factor, K, for mode I fracture, was thus evaluated for all the bone specimens and the qualifications of the determined K were also examined based on the equations and criteria provided in ASTM standard E1820 [124]. The calculations of K_{Ic} and the examinations of its qualification as fracture toughness of the bone were described in detail in reference by Zhai [173, 174].

7.3.5 Imaging of the postmortem fracture profiles

Images showing the fracture surfaces and crack path profiles of the postmortem specimens at microscopic length scales were obtained using a scanning electron microscope (SEM). The SEM

(Nova, FEI, OR, U.S.) was operated at 5 kV accelerating voltage at high vacuum in the secondary electron mode to obtain the images of fracture surfaces in full view and capture the smaller microstructural features in the specimens.

7.3.6 Statistics

An alpha level of 0.05 was used for all the statistical analysis in this study. Shapiro-Wilk (S-W) tests were performed first to examine the normality of the data. A one-way ANOVA with post-hoc tests was then performed under Bonferroni correction to test for the comparisons in fracture toughness and geometry parameters of the incipient crack profiles among the specimens in the three osteon orientations.

7.4 Results

The microstructures of the porcine cortical bone were presented in the reconstructed three-dimensional tomographic images. The high-speed X-ray images of the representative specimens that are orientated in each of the three directions were provided to understand their fracture behaviors and identify the toughening mechanisms at the dynamic loading rate. The fracture toughness and crack velocities, as functions of crack extensions, were determined quantitatively to understand their crack resistance to dynamic cracking in different directions. SEM images, showing the fracture profiles in postmortem specimens, were also provided to help study their dynamic fracture behaviors qualitatively. All the results mentioned above are presented and described separately in this section.

7.4.1 Microstructures in bone

The reconstructed three-dimensional tomographic images of the representative bone specimens in the three directions were cropped using Image J and presented in Fig. 7.4. Typical cortical bone microstructures are observed for all the scanned specimens. The light narrow rod alike structures feature the Haversian canals in in-plane transverse specimen (Fig. 7.4*a*), showing that the osteons, as the unit functional structures in cortical bone, are aligned perpendicular to the notch. As also verified by Fig. 7.4*b*, the osteons are perpendicular to the notch plane and orientated transverse to the nominal direction of the pre-machined notch for out-of-plane transverse specimen. As shown in Fig. 7.4c, the osteons are in the same plane and orientated parallel to the

notch. The average porosity was also estimated to be ~1.4% (SD: 0.6%) for all the specimens subjected to micro-CT scans. It is worth noting here the 3D tomographic images of the specimens presented in Fig. 7.4 are all in front views to succinctly show the relative orientations between the microstructures and notches. 3D images of the specimens in other views were provided in the appendix (Fig. A9).

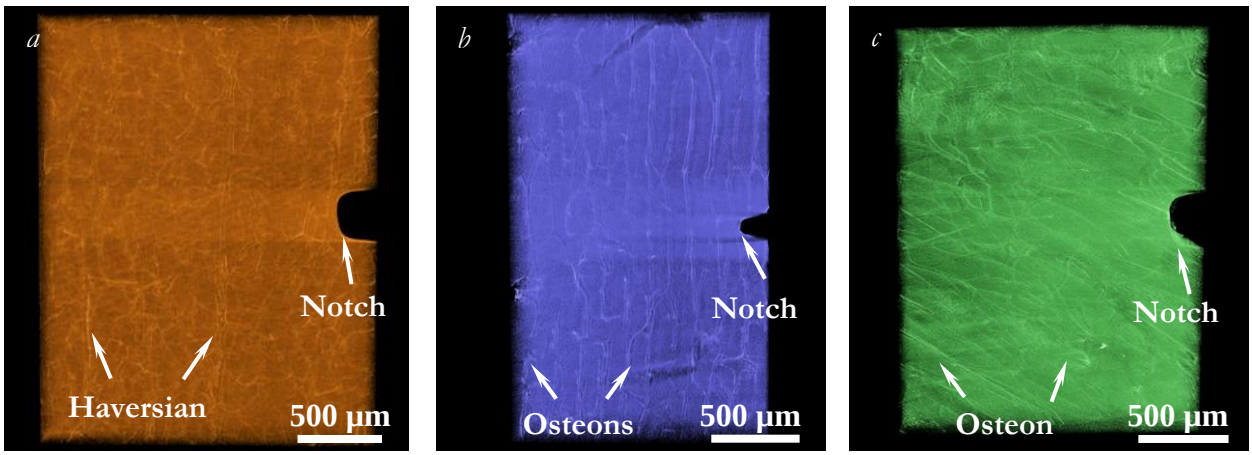

Figure 7.4 Three-dimensional tomographic images for bone specimens (*a*) in-plane transverse specimen (*b*) out-of-plane transverse specimen (*c*) in-plane longitudinal specimen

7.4.2 In-situ dynamic fracture visualization

The average loading velocity, i.e., the velocity at the sample end of the incident bar, for all the dynamic three-point bending experiments was calculated to be 5.6 ± 0.1 m/s. The entire cracking process, including the onset of the crack initiation and subsequent fracture propagation, was visualized thanks to the high-speed X-ray PCI imaging technique. The experiments for all the 19 specimens were performed under identical measuring conditions to minimize all the other experimental variables except the osteon direction. The recorded high-speed X-ray images of three representative specimens (5,000,000 fps) orientated in each of the three directions were cropped using Image J and presented in Figs 7.5─7.7. As a consequence of different osteon orientations (with respect to the crack propagation direction), the crack paths are varied significantly among the three representative specimens, as comparatively more tortuous crack trajectories were observed for the in-plane transverse and out-of-plane transverse specimens (Figs. 7.5 and 7.6) while straighter crack profile was found in the in-plane longitudinal specimen (Fig. 7.7).

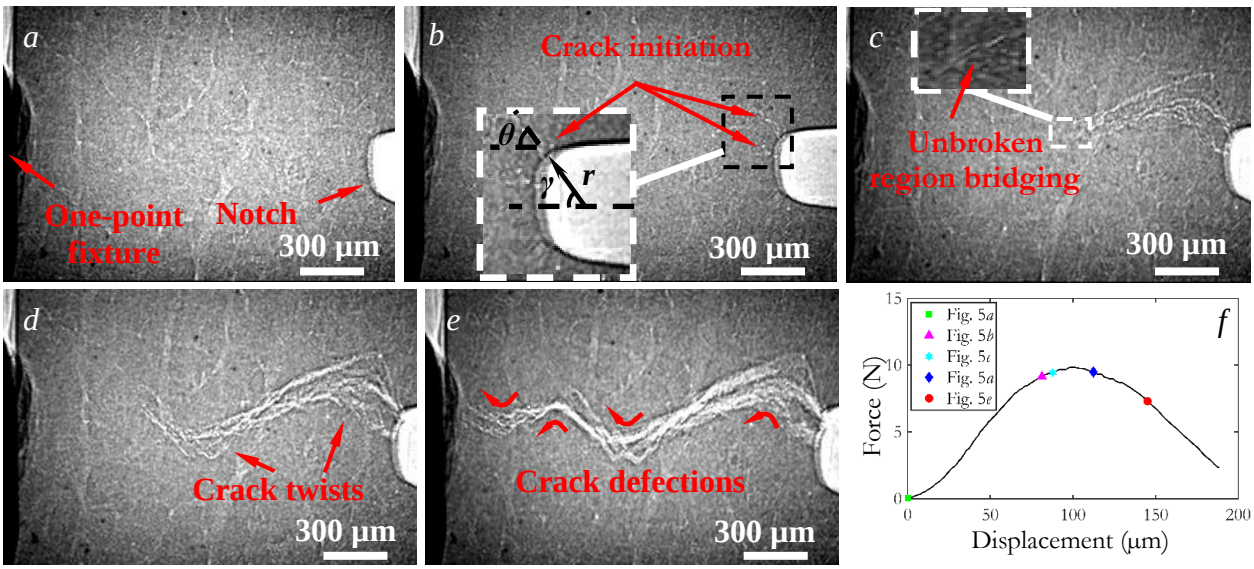

Figure 7.5 High-speed X-ray images of a representative in-plane longitudinal specimen (*a*) t = 0 μs, (*b*) t = 22 μs, (*c*) t = 23 μs, (*d*) t = 26.6 μs (*e*) t = 31.6 μs (*f*) corresponding load-displacement curve. The r was the round notch's root radius and the angle γ was measured as the center angle between the location where the crack initiated and the point where the round notch intersected the horizontal symmetric axis. The positive sign in front of γ denotes counter-clockwise direction while the negative sign denotes clockwise direction. The angle θ was the angle between the propagation direction of the incipient crack (before a crack deflection occurred) and the horizontal symmetric axis.

The high-speed X-ray images of a representative in-plane transverse (medial-lateral) specimen are provided in Fig. 7.5, where the one-point fixture was on the left side and the notch was located on the right edge. In the X-ray images, the bright narrow lines aligned perpendicular to the nominal direction of the notch (parallel to the osteons) are the Haversian canals, while those bright lines aligned parallel to the notch (perpendicular to the osteons) are Volkmann canals. For the representative in-plane transverse specimen, one major crack initiated at the radius root of the notch (Fig. 7.5*b*) with a highly twisted and curved fracture surface, showing two different initiation locations at the front and back surfaces (across the width direction) of the specimens. The inclined angles, γ, to the horizontal symmetric axis for the two crack initiation locations on the front and back surfaces were ~-48° and -39° (Fig. 7.5*b*), respectively. The propagation direction of the incipient crack (before an occurrence of crack deflection), described by θ (Fig. 7.5*b*) was measured to be ~-56° and -34° to the horizontal symmetric axis. After propagating straightly along the initial crack direction for approximately ~287 μm, the crack first deflected ~110° and then further traveled a distance of ~910 μm along that direction until another crack deflection of ~90° took

place (Fig. 7.5*c*, *d*). After continuing to propagate along a comparatively straight path orientated ~45° to the horizontal symmetric axis for about ~480 μm, the crack deflected ~100° again and advanced to the left edge of the specimen in a slightly wavy path, finally resulting in an entire failure of the specimen (Fig. 7.5*e*). Overall, the crack path was highly serrated, and the fracture surface was rough (Fig. 7.5*e*). During the entire cracking process, crack twists and unbroken-region bridging were also observed and they both acted as potential toughening mechanisms (Fig. 7.5*c* and *d*) in such direction. The corresponding load-displacement curve (Fig. 7.5*f*) showed that the crack initiation occurred prior to the maximum force and the entire specimen was still capable to bear the load until the end of the incipient crack phase (Fig. 7.5*c*).

High-speed X-ray images of a representative out-of-plane transverse specimen were presented in Fig. 7.6. The microstructures were revealed under the synchrotron X-ray, as the irregular shaped dark area were the osteons that aligned perpendicular to the X-ray images and the bright areas surrounding the osteons were the interstitial lamellae (interfacial materials). As expected, the crack-initiation also took place at the notch. The angle γ and θ, describing the crack-initiation location and incipient crack propagation direction, were measured to be 52° and 0°, respectively. Comparing with the in-plane transverse specimen (Fig. 7.5), the crack path in the out-of-plane transverse specimen was generally straighter and less curved. The crack first propagated along the interfacial bony tissues in a short distance of ~330 μm (Fig. 7.6*b*) and then directly cut through all the osteons it encountered as it propagated toward the left edge of the specimen until it traveled another distance of ~1.1 mm (Fig. 7.6*d*). As the crack impinged upon the interface between two osteons again, it bifurcated into two cracks, with one continued propagating in the interstitial lamellae while the other drove forward by splitting the osteon into multiple parts (Fig. 7.6*e*). Shortly, the two cracks converged into one at the interstitial lamellae and started to propagate forward along the cement lines or interstitial lamellae until it finally failed the entire specimen (Fig. 7.6*e*). Slight extent of crack deflections and/or twists were only observed in the late period of the cracking process (Fig. 7.6*e*), resulting in a comparatively smoother crack trajectory. Unbroken-region bridging was also observed as a mechanism of toughening in the X-ray images of such out-of-plane transverse specimen (Fig. 7.6*c*). As shown in the load-displacement curve in Fig. 7.6*f*, the crack initiated shortly before the maximum load and the force dropped gradually after the incipient crack period.

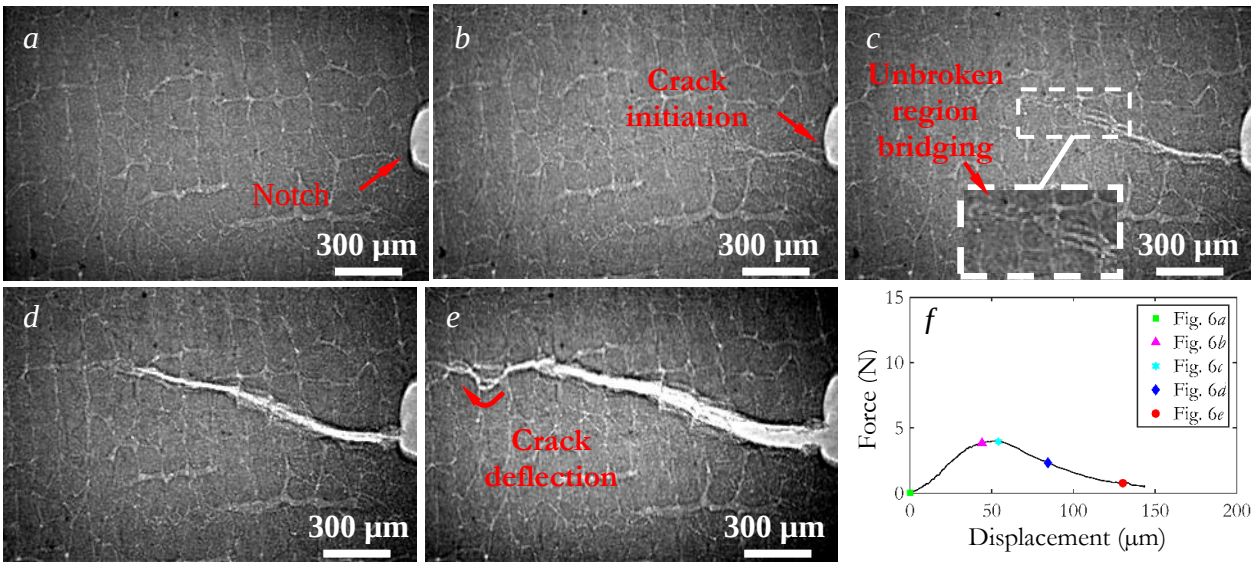

Figure 7.6 High-speed X-ray images of two representative cortical bone specimens. (*a*) t = 0 μs, (*b*) t = 15.6 μs, (*c*) t = 17.6 μs, (*d*) t = 22.8 μs, (*e*) t = 29.6 μs, (*f*) corresponding load-displacement curve.

As presented for the high-speed X-ray images of a representative in-plane longitudinal specimen in Fig. 7.7, where the long axes of osteons were orientated approximately in the same direction (with a misorientation of ~15°) as the notch's nominal direction, the crack developed an overall smoother and straighter trajectory than the other two representative specimens (Figs. 7.5 and 7.6). The crack was also initiated at the notch root (Fig. 7.7*b*) that located on the right side in the images. As defined earlier in Fig. 7.5, the angle γ, denoting the location of crack initiation, and angle θ, representing the crack's subsequent propagation direction, were measured to be 41° and 11°, respectively. The crack propagated along a straight path by first penetrating through the microstructures for a distance of ~700 μm and then traveled along the osteon cement lines for another ~900 μm (Fig. 7.7*c*-*e*). Afterward, the crack curved its propagation direction slightly to cut through the osteons and finally broke the entire specimen (Fig. 7.7*e*). In general, few crack deflections and twists were observed along its entire crack path and, in the X-ray images, only unbroken-region bridging was found acting as a main toughening mechanism. Similar as that for out-of-plane transverse specimen, the load-displacement curve indicated that the crack initiated shortly ahead of the peak load and the force started to drop rapidly as the crack continued to propagate after the incipient crack phase.

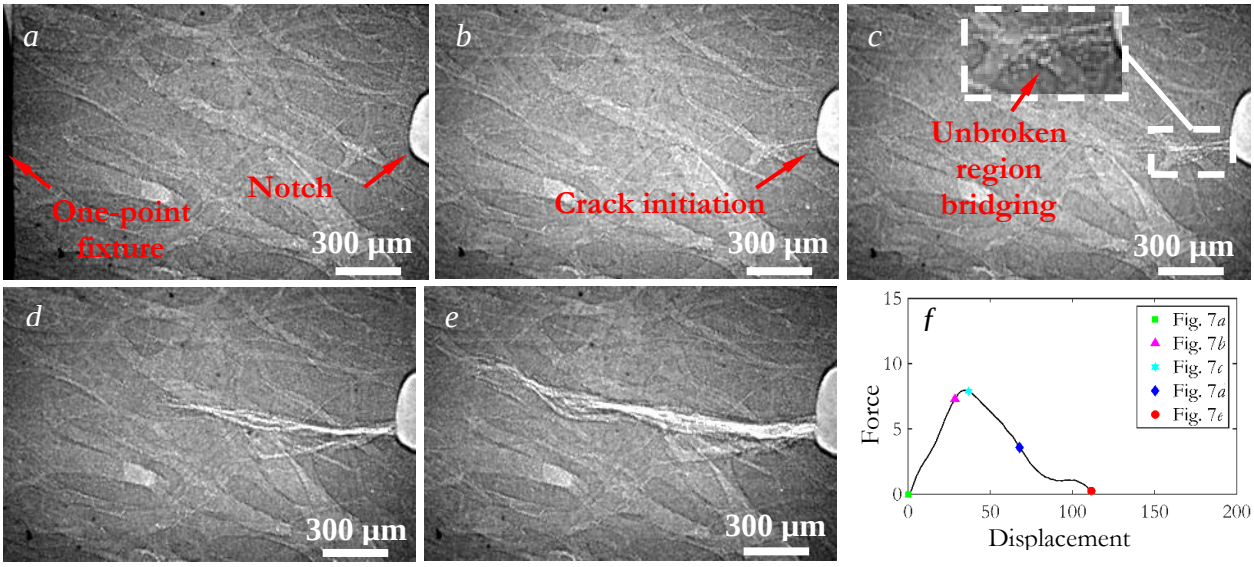

Figure 7.7 High-speed X-ray images of a representative in-plane longitudinal specimen (a) t = 0 s, (*b*) t = 12.6 μs, (*c*) t = 14.4 μs, (*d*) t = 20.2 μs, (*e*) t = 26.8 μs, (*f*) corresponding load-displacement curve.

7.4.3 Fracture toughness and crack velocity

The crack extensions in each bone specimen were measured using the high-speed images that synchronized with the recorded load-displacement data. The dynamic fracture toughness in terms of stress intensity factor of mode I fracture at each step of crack extension was thus determined using Eq. (5.3) for all the specimens in the three osteon directions. The fracture toughness, K, was then plotted as a function of crack extension as shown in Fig. 7.8*a*, where the crack-growth resistance curves (R-curves) were also provided for reference. The average fracture initiation toughness, K_{Ic}, of the specimens was provided with the p-values of the statistical tests in Fig. 7.8*b*. All the specimens exhibited rising R-curves while the degree of growth was varied as the osteon orientation changed among the three directions. The average K_{Ic} increased in general as the osteon orientation changed from in-plane longitudinal to out-of-plane transverse first and then to in-plane transverse finally, with a significant statistical growth by 80% found between the in-plane longitudinal and in-plane transverse directions.

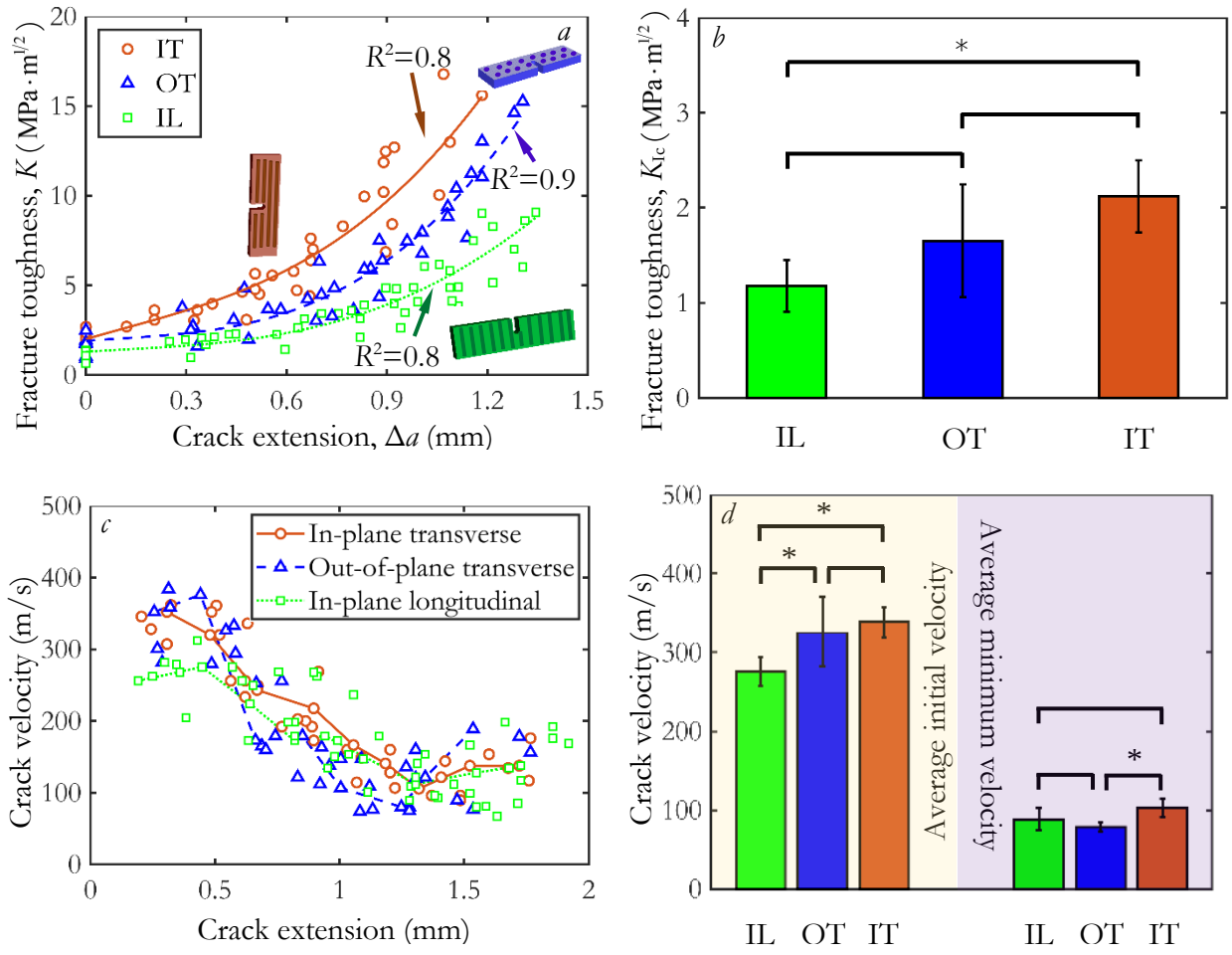

Figure 7.8 Fracture behaviors of porcine cortical bone in different osteon orientations at dynamic loading rate (*a*) crack-growth resistance curves (*R*-curves) (*b*) average fracture initiation toughness (*c*) crack velocity of the specimens in terms of crack extension. The crack velocity data for all the specimens are plotted, where the crack velocity-crack extension curves of three specimens representing the average curves of their corresponding osteon orientations are also provided (*d*) initial crack velocity and minimum crack velocity (*: $p<0.05$)

The crack propagation velocities of all the specimens for the three osteon orientations were determined and plotted in terms of the crack extension in Fig. 7.8*c*, where the crack velocity-crack extension curves of three specimens representing the average crack velocities of their corresponding osteon orientation were also presented for comparison. For all the specimens, the crack velocity was dependent on the crack extension significantly and exhibited similar variation trend: the crack propagated with a higher initial speed upon the crack initiation for a short period and then dropped continuously until reached the minimum value and finally turned to grow up again. It was also found that, although the average initial crack propagation velocity for the in-

plane longitudinal direction was lower than the other two directions (Fig. 7.8*d*), the cracks ultimately propagated at similar speeds for all the specimens in the three directions (Fig. 7.8*c* and *d*).

The SEM images of the postmortem specimens are provided in Fig. 7.9 to demonstrate the differences in crack profiles among the three osteon orientations. The cracks in in-plane transverse specimens took more rugged paths and the fracture surfaces were more tortuous than the specimens in the other two directions. It is clearly seen the concentric lamellae were aligned perpendicular to the crack path and the osteons were mostly cut through directly in transverse by the crack, with only several lamellae protruding from the fracture surface (Fig. 7.9*a* and *d*), suggesting that the crack was deflected or twisted as it impinged upon the cement lines, which made a major contribution to the fracture toughness in such direction. However, the in-plane longitudinal specimens developed expected the smoothest and straightest crack trajectories among all the three directions (Figs. 7.9*c*): the crack propagated straight through the microstructure along the axis of osteon with fewest crack deflections and twists. As shown in the image with higher magnification, the osteons were either incised by the crack at a small angle with respect to its axis or split entirely along the longitudinal direction (Figs. 7.9*f*), indicating that the crack followed the concentric lamellae as it traveled in the bone microstructure. The tortuosity of crack path for out-of-plane transverse direction generally fell in between that in the other two directions and even varied among the specimens in such direction. In other words, some of the cracks traveled along comparatively more curved paths (Figs. 7.9*b*) as those for in-plane transverse specimens (Fig. 7.9*a*) while others (Fig. 7.6), similar to those in-plane longitudinal specimens, created smoother trajectories (Figs. 7.7 and 7.9*c*). The image at a closer view showed that the osteons were either split radially or cut through transversely by the crack (Fig. 7.9*f*), which was a mixed mode of the two main failure types observed in specimens in the other two directions. In addition, proof for crack wake bridging as a mechanism in resisting crack from propagation in in-plane transverse specimens was also provided (Fig. A10).

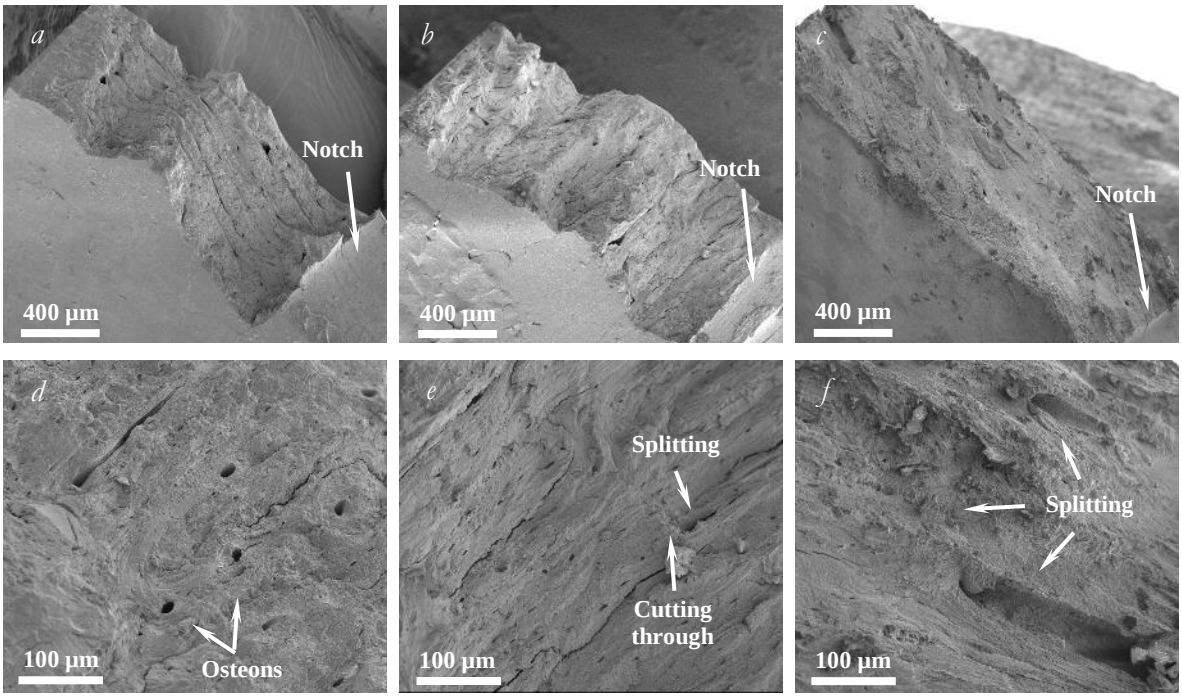

Figure 7.9 SEM images showing the fracture surfaces and crack paths of the porcine bone specimens in three osteon orientations at dynamic loading rate (*a*) an overview for the fracture surface of the in-plane transverse specimen (*b*) a full view for the fracture surface of the out-of-plane transverse specimen (*c*) an overview for the fracture profile of the in-plane longitudinal specimen (*d*) a closer image with higher magnification showing the fracture surface of the in-plane transverse specimen (*e*) a closer image showing the fracture profile of the out-of-plane longitudinal specimen (*f*) a closer view with higher magnification showing the fracture surface of the in-plane longitudinal specimen

7.5 Discussions

In this section, the effect of osteon orientation on the dynamic fracture behaviors of cortical bone are discussed on multiple aspects covering the entire fracture process, which includes the crack initiation, incipient crack propagation direction, crack propagation velocity, fracture toughening mechanisms and consequently fracture toughness.

7.5.1 Incipient crack and crack velocity

For all the 19 porcine cortical bone specimens subjected to dynamic three-point bending loadings in this study, the cracks initiated on the notch root surfaces as expected. The onset locations of crack initiation and incipient crack propagation direction are only slightly varied within the specimens aligned in the same direction. The angles γ and θ, defined as the geometry

parameters of the initial crack in Fig. 7.4*b*, were measured for all the specimens and listed in Table 7.1, where the statistical results of ANOVA tests were also provided. The geometry parameters (γ and θ) can be dependent on many factors, among which two aspects play the most important roles: the intrinsic microstructures around the notch and extrinsic mechanical states because of the loading conditions. Specifically, the angle γ, defining the onset location of crack initiation, is merely varied among all the specimens in in-plane transverse and out-of-plane transverse directions, i.e., insignificant difference is found between the two directions. Although the γ of the specimens for in-plane longitudinal direction, according to the statistical analysis, is significantly different from the other two directions (in-plane transverse and out-of-plane transverse), the difference of mean values is comparatively small (14%), indicating that the crack initiation location is likely dependent on the extrinsic loading conditions rather than to the osteon orientation, or the microstructures around the notch, which is consistent with the experimental results of our previous works [173, 174]. On the other hand, the situation for the propagation direction of the incipient crack, as defined to be θ, is consistent for the specimens within the same direction but largely different among the three osteon orientations. Specifically, the incipient crack propagates along a direction that is largely deviated from the horizontal direction for in-plane transverse specimens, while the initial crack direction, as measured to be ~9°─10°, is only slightly inclined to the horizontal direction (the specimen's symmetrical axis) for the specimens in the other two directions. Provided that both the intrinsic microstructure and extrinsic loading condition play significant roles in determining the incipient crack propagation direction, such variation is mainly a consequence of the interactions between the two factors: the extrinsic loading conditions is the primary factor for out-of-plane transverse and in-plane longitudinal specimens while it is presumably the intrinsic microstructures that play the dominant role in in-plane transverse specimens [173, 174]. It should be noted that the horizontal propagation direction of incipient crack indicates a primarily tensile stress state and a predominant mode I crack in the two former directions while the largely deviated initial crack direction from the horizontal direction can be a consequence of the mixed crack modes I and II in the latter direction [115, 175].

Table 7.1 Onset location of crack initiation and the direction of its subsequent propagation

Angle	Direction	No. 1	No. 2	No. 3	No. 4	No. 5	No. 6	No. 7	Mean	SD	ANOVA	
	IL	-36°	43°	44°	46°	-39°/-14°	41°	-44°/0°	42°	3°	A	
γ	OT	45°	-50°	52°	46°	-49°	-45°	-	48°	3°		B
	IT	46°	-55°	-49°	48°	44°	-48°/-39°	-	48°	4°		B
	IL	18°	-10°	-13°	15°	18°/0°	11°	0°/0°	10°	7°	A	
θ	OT	-14°	-10°	0°	5°	-24°	-3°	-	9°	9°	A	
	IT	42°	-45°	-50°	-44°	41°	-56°/-34°	-	46°	6°		B

Note: 1. A positive value of angle denotes counter-clockwise direction while a negative value denotes clockwise direction. Specimens with two values of γ and θ denote either two major cracks or one crack showing two different paths on front and back surfaces of the specimens, and only the first value is chosen for statistical analysis.
2. Values of γ and θ denoted with the same letter between any two groups are insignificantly different, while values of γ and θ denoted with different letters between any two groups are significantly different in ANOVA tests.

The crack propagation velocity is a function of many factors, such as the material's microstructure, stress state, crack mode, loading rate, specimen geometry and size. In this study, the crack velocity is found to be dependent on crack extension significantly over the entire crack path and a similar variation trend is observed for all the specimens in the three directions: the velocity drops first while grows up again as the crack extends continuously. The statistical results suggest that, although the cracks in specimens propagate with largely varied initial velocities among the three directions, the crack velocity-crack extension curves of all the specimens finally converged (Fig. 7.8*d*) and the cracks ultimately travel at similar speeds for most of the specimens. A theory relating the crack propagation speed and crack bifurcation was proposed by Sih in [126], where it is suggested that, when crack is propagating with a lower speed, the majority of strain energy in the area in front of the crack tip is allocated for volume changing rather than shape changing, which in turn tends to develop a crack path with fewer bifurcations and hence results in a smoother fracture surface. Such relation is further verified in our study: during the initial crack phase, less tortuous crack path and smoother fracture surface are observed in most of the in-plane longitudinal specimens (Fig. 7.7) while bifurcations occur more frequently in the specimens in the other two directions (Figs. 7.5 and 7.6). Comparing with our previous works where the crack velocity is less sensitive to crack extensions, the crack velocity varies significantly as the crack

propagates in specimens in this work. This is mainly because that the recorded images of the cracking process enclose the entire specimen since smaller specimens are used in this study, and consequently, the crack propagation velocity plotted in Fig. 7.8 are based on the specimens' full crack paths rather than that just based on the earlier crack paths in [173, 174]. However, it is worth noting that the initial crack propagation speeds of the in-plane transverse specimens provided in Fig. 7.8 are within the same level as those reported in our previous works for specimens in the same direction [173, 174].

7.5.2 Fracture toughness and toughening mechanisms

Previous studies in the literature suggested that the large variation found in cortical bone's fracture toughness at quasi-static loading rate can be mainly attributed to the transition in its toughening mechanisms when the loading direction continuously changes from along the osteon to transverse to the osteon [42, 76, 83]. In our study, it is found that such a transition in toughening mechanisms and consequently the fracture toughness still remains even at dynamic loading rate, although it is widely believed that bone always turned into a significantly brittle material as loading rate increased from quasi-static to dynamic in no matter which osteon orientation. To resist the crack initiation along the osteon orientation, the cortical bone developed an average toughness K_{Ic}, of ~1.2 MPa·m$^{1/2}$, whereas the average fracture initiation toughness is ~2.1 MPa·m$^{1/2}$ for the in-plane transverse specimens, which is nearly a twice increase. The K_{Ic} for out-of-plane transverse direction varied more significantly among the specimens, with its average value measured to be ~1.7 MPa·m$^{1/2}$, which falls in between that of the other two directions. This is likely due to that the out-of-plane transverse specimen's microstructure around the notch can be either similar to one of the other two directions or a combination of both the extreme cases. All the specimens exhibit rising *R*-curves as cracks extend, but the degree of growth for the in-plane transverse specimen is significantly higher than the in-plane longitudinal specimen and it lies in between the former two directions for out-of-plane transverse direction. For example, as shown in Fig. 7.8*a*, after only a crack extension of 1.2 mm, the fracture toughness, *K*, increased more than eight times of the initial values for the in-plane transverse direction, but it only increased by a factor of five for the in-plane longitudinal direction. As the osteon orientation continuously changes from in-plane longitudinal to out-of-plane transverse first and to in-plane transverse finally, the corresponding continuous variations found in both the fracture initiation toughness and *R*-curves

suggest a transition, from a highly brittle to a comparatively ductile-like fracture behavior, also takes place even at dynamic loading rate.

The dynamic fracture initiation toughness, K_{Ic}, of the in-plane transverse specimens obtained in this study is lower than but at the same level as those of porcine, bovine and equine cortical bones that measured in the same orientation at dynamic loading rate in other works [51, 58, 173, 174]. Such a slight difference in K_{Ic} can be owing to the different species, anatomical locations and specimen dimensions of the bone used in their studies [51, 58, 173, 174]. Comparing with the few available *R*-curves of bones in the in-plane transverse direction in literature [58, 77, 170, 174], the dynamic *R*-curves of porcine cortical bone presented in Fig. 7.8 are increasing more rapidly than the dynamic *R*-curves of porcine cortical bone [174] as well as bovine cortical bone [58] reported in previous works, which is primarily due to the smaller specimens used in this study, and the differences in bone's breeds, ages, species and anatomical locations.

The real fact behind the observed transition in fracture toughness is that different toughening mechanisms are developed in bone and they play different roles in cracking resistance in different osteon orientations. Indeed, the transition found in fracture toughness evaluated quantitatively is verified by the observed transition in toughening mechanisms unveiled by the high-speed X-ray images. When the crack propagates perpendicular to the osteons as the case for in-plane transverse specimen, the cement lines that aligned roughly transverse to major crack act as cracking barriers to deviate the growing cracks significantly from its original direction, causing marked crack deflections and twists (Fig. 7.5), which in turn necessitates higher applied load for further cracking and provides the major contribution to the high toughness consequently [165]. In addition, other mechanisms, such as crack-wake bridging and unbroken-region bridging, also play roles in such in-plane transverse specimens (Figs. 7.5, 7.9 and A10). The primary mechanism of toughening is quite different for in-plane longitudinal specimens, where the main crack propagates longitudinal to the osteons, generating a straight crack path and smooth fracture surface. In such case, microcracks initiated ahead of the major crack tip lead to the formation of unbroken regions along the crack length (Fig. 7.7), which acts to bridge the main crack and to carry the load that would otherwise be applied to develop the major crack [165]. For several of the in-plane longitudinal specimens with a small misorientation (~8° inclined from the notch direction), the slightly misaligned fibrils behind the crack tip can also act as crack bridges to reduce the driving force for further crack propagation [42]. However, the toughening resulting from mechanisms of unbroken-

region bridging and crack wake bridging is far less potent than that due to crack deflection/twist [76, 83], leading to a comparatively low toughness in the longitudinal direction. The case for out-of-plane specimens is in between the above two extreme cases, where a transition in toughening mechanism, from crack deflections or twists dominant to unbroken-region bridging dominant occurs and crack-wake bridging disappears (Fig. 7.6).

The transition in toughening mechanisms observed in high-speed X-ray images are further confirmed by the SEM images of the postmortem specimens (Fig. 7.9). The crack paths for in-plane transverse specimens are highly tortuous and cranked (Fig. 7.9a). Crack deflections and twists, although diminished to some extent compared with the quasi-static situation, still exist and act as the primary toughening mechanisms at dynamic loading rate. Besides crack deflections and twists, evidence that crack-wake bridging by fibrils in the in-plane transverse specimen is also provided by the SEM images as shown in Fig. A10. Owing to the limited potential mechanisms of toughening for in-plane longitudinal specimens, cracks propagate straight through its entire microstructures along the lamellae direction and most of the osteons were directly split either along the cement lines or interlamellar boundaries, generating an overall highly smooth trajectory (Fig. 7.9*c*). Cracks in out-of-plane transverse specimens travel along paths with fewer crack deflections and twists than the in-plane transverse specimens, showing comparatively less rough fracture profiles. Some osteons were cut through transversely while others were split longitudinally, suggesting a mixed mode of fractures in such direction.

7.6 Conclusions

In the present study, the entire fracture process, including crack initiation and subsequent crack propagation in cortical bone in three osteon orientations at dynamic loading rate was visualized, in real-time, by the integration of high-speed synchrotron X-ray PCI technique with a modified Kolsky compression bar. The onset location of crack initiation is found largely deviated from the plane of maximum tensile stress for all the specimens, while the initial crack propagation direction varies significantly among the different osteon orientations. It is found that crack propagation velocity is dependent on crack extension significantly, and the initial crack velocity is lower for the in-plane longitudinal direction than the other two directions. Both the fracture toughness, measured in terms of stress intensity factor, and the toughening mechanisms observed in high-speed X-ray images, suggests a transition, from a highly brittle to a ductile-like fracture behavior

in cortical bone at the dynamic loading rate, as the osteon orientation varies continuously from in-plane transverse to out-of-plane longitudinal first and then to in-plane longitudinal finally.

APPENDIX

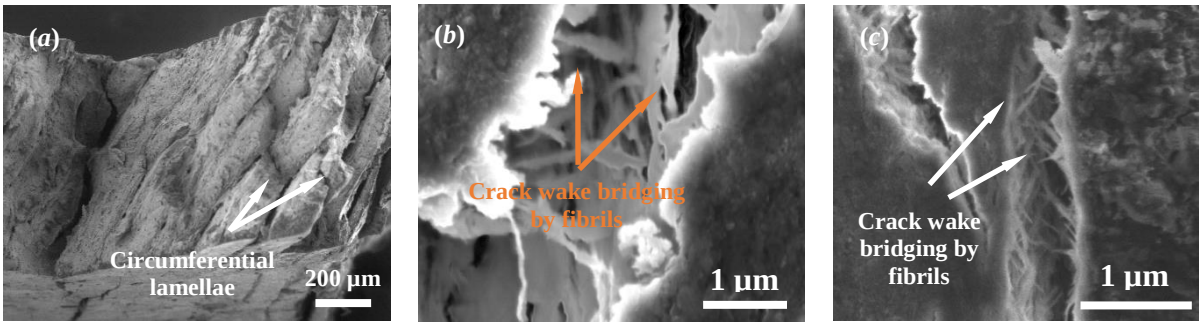

Fig. A1 SEM images showing the fracture surfaces and crack paths of the bone specimens (*a*) a close image showing the circumferential lamellae in the second representative cortical bone specimen with zig-zag crack path (*b*) observed crack wake bridging in cortical bone loaded quasi-statically (*c*) image showing the crack wake bridging in cortical bone loaded dynamically

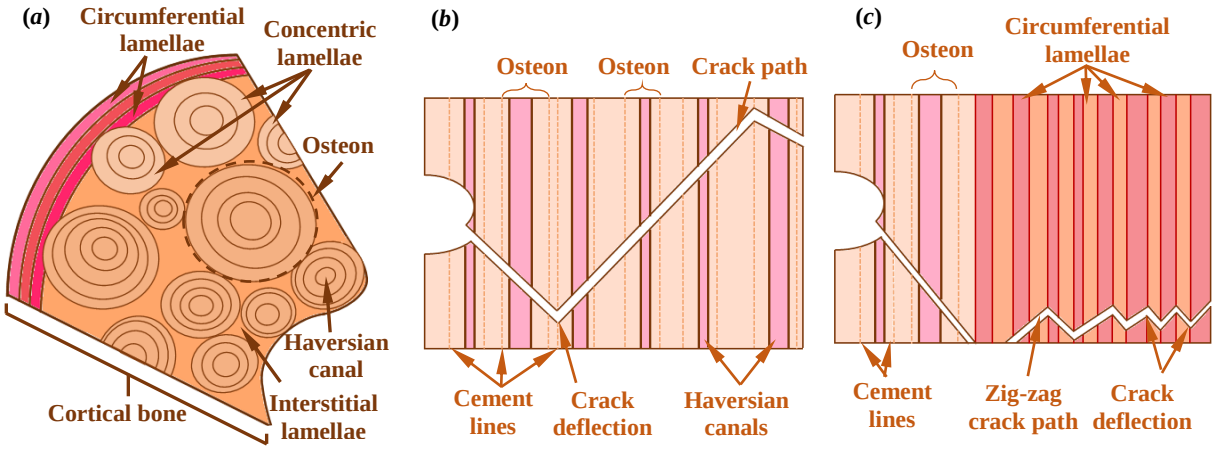

Fig. A2 Schematic of the crack propagation in cortical bone specimens (*a*) schematic of the microstructures in cortical bone (*b*) crack propagation in the first cortical bone specimen (*c*) crack propagation in the second cortical bone specimen

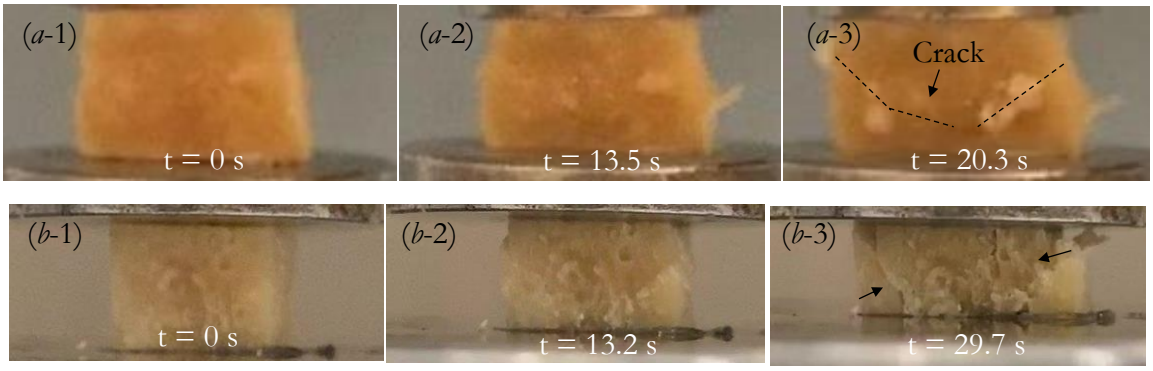

Fig. A3 Images of the skull specimens at quasi-static strain rate (a) radial direction (b) tangential direction

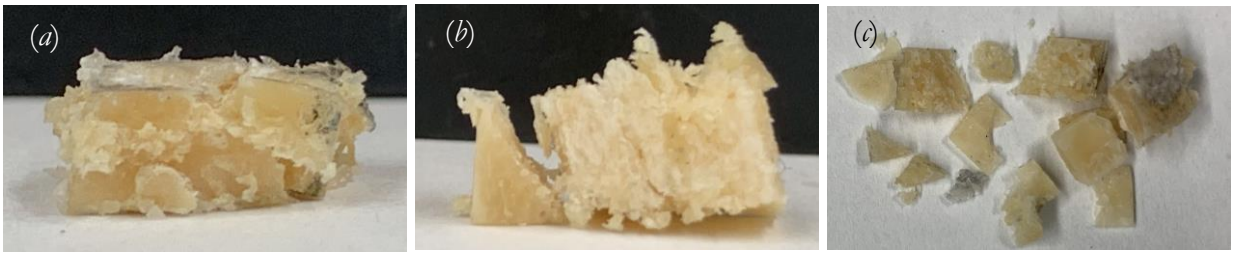

Fig. A4 Images of the skull specimens at intermediate strain rate (a) radial direction (b) first representative specimen in tangential direction (c) second representative in tangential direction

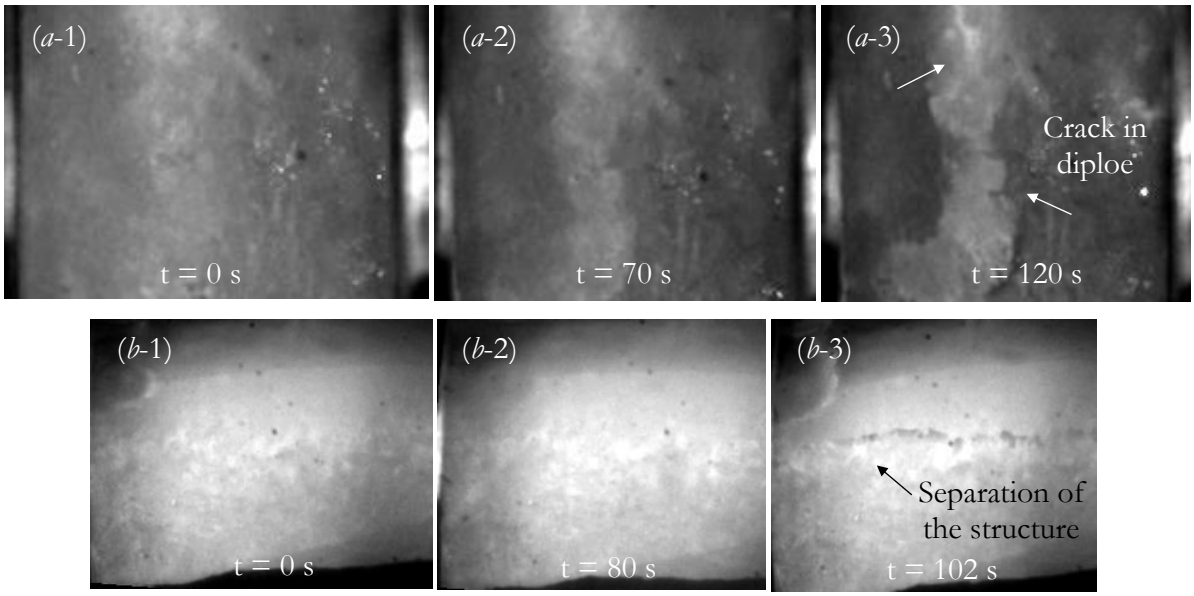

Fig. A5 Images of the skull specimens at high strain rate (a) radial direction (b) tangential direction

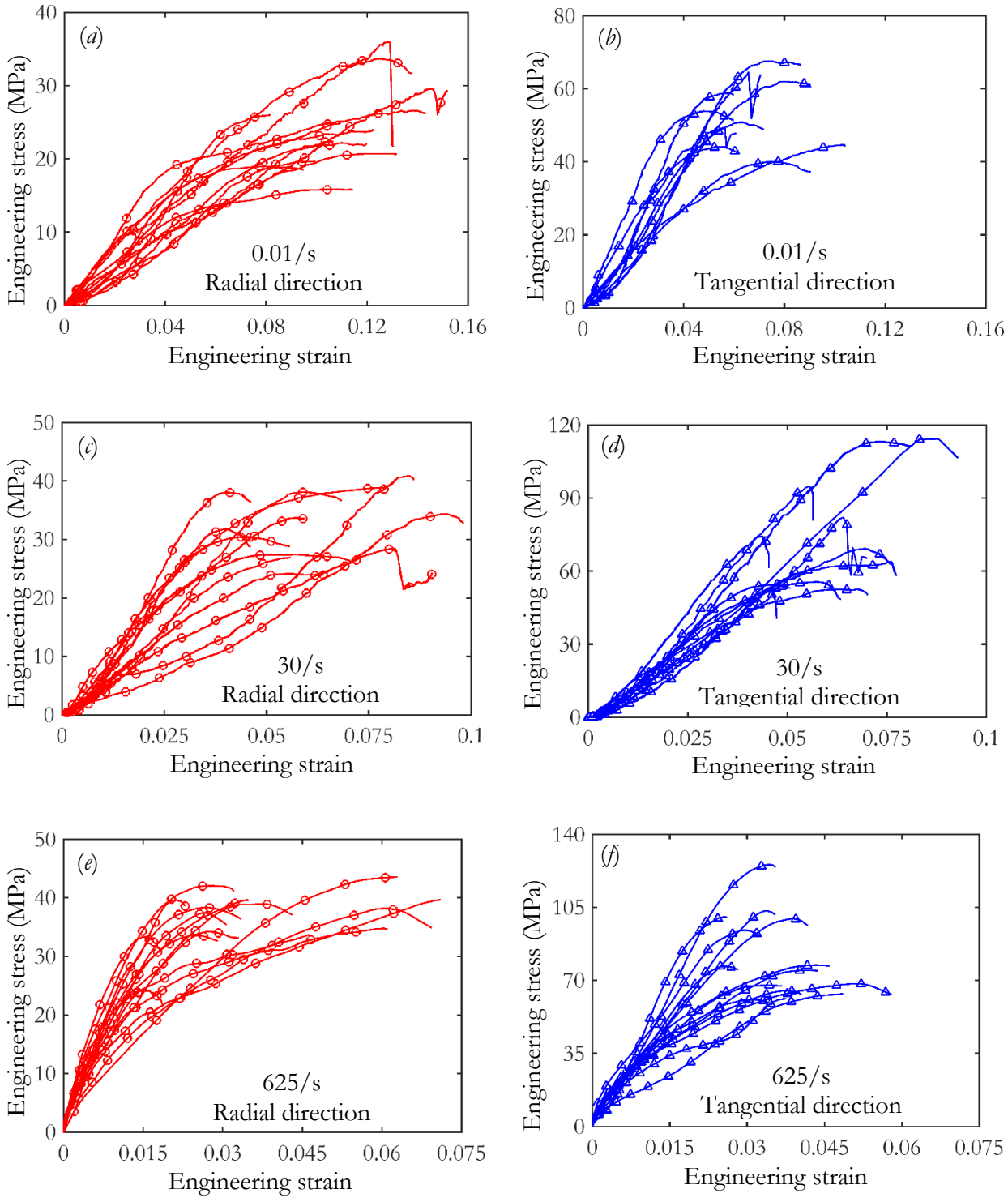

Fig. A6 Stress-strain curves of human frontal skulls along radial and tangential loading directions at quasi-static, intermediate and high strain rates

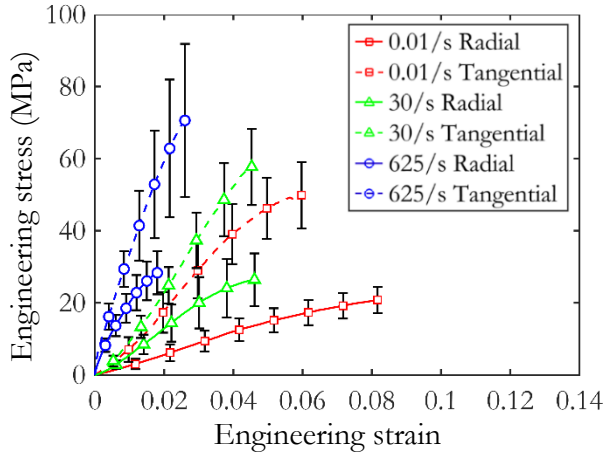

Fig. A7 Average stress-strain curves of human frontal skulls in radial and tangential loading directions at quasi-static, intermediate and high strain rates

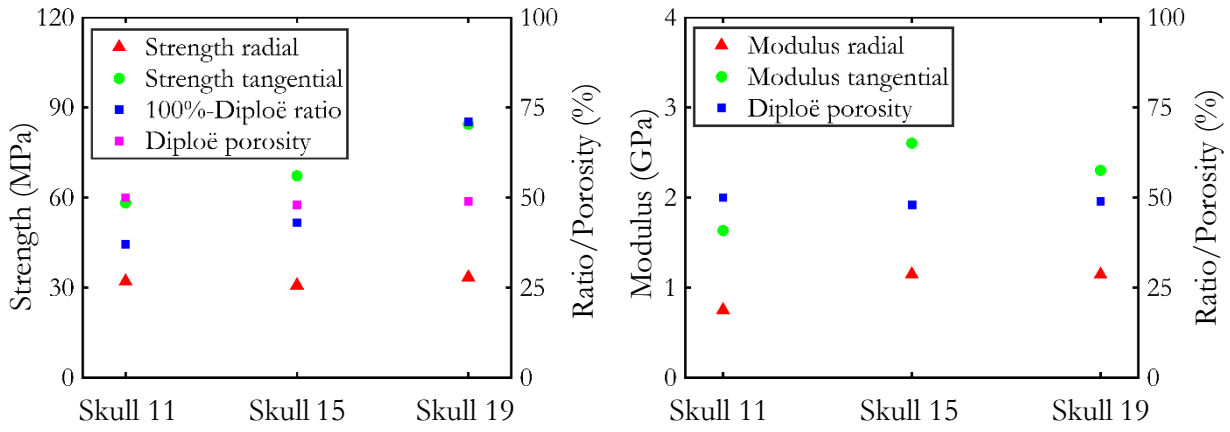

Fig. A8 Relations between structure parameters of the skulls and their mechanical properties

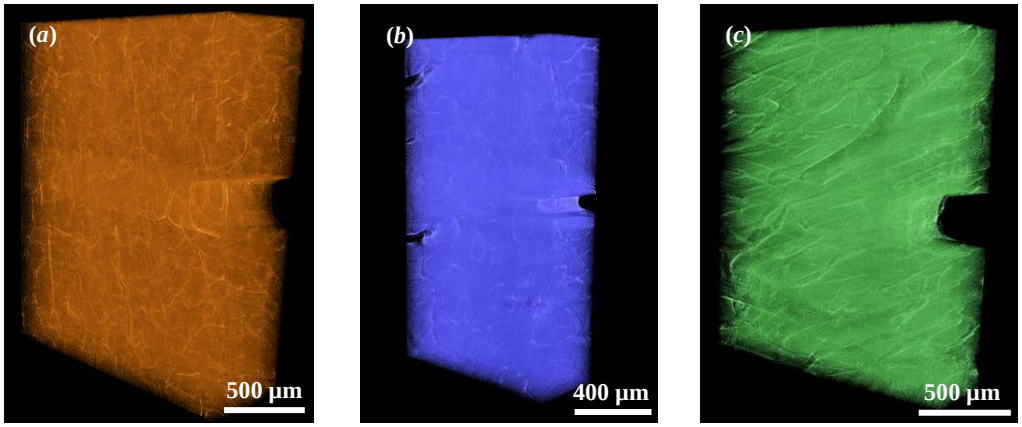

Fig. A9 3D tomographic images of the cortical bone specimens (a) in-plane transverse direction (b) out-of-plane transverse direction (c) in-plane longitudinal direction

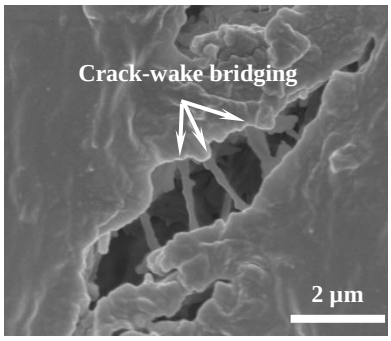

Fig. A10 SEM image showing the crack-wake bridging in a representative in-plane transverse specimen

REFERENCES

[1] S. Weiner, H.D. Wagner, The Material Bone: Structure-Mechanical Function Relations, Annual review of materials science. 28 (1998), 271-298.

[2] J.-Y. Rho, L. Kuhn-Spearing, P. Zioupos, Mechanical Properties and the Hierarchical Structure of Bone, Medical engineering & physics. 20 (1998), 92-102.

[3] G. Marotti, A New Theory of Bone Lamellation, Calcified Tissue International. 53 (1993), S47-S56.

[4] J. Currey, 'Osteons' in Biomechanical Literature, Journal of biomechanics. 15 (1982), 717-717.

[5] S.J. Hall, Basic Biomechanics with Dynamic Human Cd and Powerweb/Olc Bind-in Passcard, McGraw-Hill Humanities/Social Sciences/Languages, 2002.

[6] C.M. Gdyczynski, A. Manbachi, S. Hashemi, B. Lashkari, R.S.C. Cobbold, On Estimating the Directionality Distribution in Pedicle Trabecular Bone from Micro-Ct Images, Physiological measurement. 35 (2014), 2415.

[7] D.B. Burr, C. Milgrom, D. Fyhrie, M. Forwood, M. Nyska, A. Finestone, S. Hoshaw, E. Saiag, A. Simkin, In Vivo Measurement of Human Tibial Strains During Vigorous Activity, Bone. 18 (1996), 405-410.

[8] L. Lanyon, W. Hampson, A. Goodship, J. Shah, Bone Deformation Recorded Invivo from Strain Gauges Attached to Human Tibial Shaft, J BONE JOINT SURG BR. (1974), 565-565.

[9] C.T. Rubin, L.E. Lanyon, Limb Mechanics as a Function of Speed and Gait: A Study of Functional Strains in the Radius and Tibia of Horse and Dog, Journal of experimental biology. 101 (1982), 187-211.

[10] U. Hansen, P. Zioupos, R. Simpson, J.D. Currey, D. Hynd, The Effect of Strain Rate on the Mechanical Properties of Human Cortical Bone, Journal of biomechanical engineering. 130 (2008), 011011.

[11] H. Yamada, F.G. Evans, Strength of Biological Materials, (1970).

[12] Y.-c. Fung, Biomechanics: Mechanical Properties of Living Tissues, Springer Science & Business Media2013.

[13] E. Bosboom, M. Hesselink, C. Oomens, C. Bouten, M. Drost, F. Baaijens, Passive Transverse Mechanical Properties of Skeletal Muscle under in Vivo Compression, Journal of biomechanics. 34 (2001), 1365-1368.

[14] J.G. Pinto, Y. Fung, Mechanical Properties of the Heart Muscle in the Passive State, Journal of biomechanics. 6 (1973), 597-616.

[15] D. Hawkins, M. Bey, Muscle and Tendon Force-Length Properties and Their Interactions in Vivo, Journal of Biomechanics. 30 (1997), 63-70.

[16] M. Van Loocke, C. Lyons, C. Simms, A Validated Model of Passive Muscle in Compression, Journal of biomechanics. 39 (2006), 2999-3009.

[17] M. Van Loocke, C.K. Simms, C.G. Lyons, Viscoelastic Properties of Passive Skeletal Muscle in Compression—Cyclic Behaviour, Journal of Biomechanics. 42 (2009), 1038-1048.

[18] M. Van Loocke, C. Lyons, C. Simms, Viscoelastic Properties of Passive Skeletal Muscle in Compression: Stress-Relaxation Behaviour and Constitutive Modelling, Journal of biomechanics. 41 (2008), 1555-1566.

[19] A.R. Gillies, R.L. Lieber, Structure and Function of the Skeletal Muscle Extracellular Matrix, Muscle & nerve. 44 (2011), 318-331.

[20] J. Trotter, P. Purslow, Functional Morphology of the Endomysium in Series Fibered Muscles, Journal of morphology. 212 (1992), 109-122.

[21] B. Song, W. Chen, Y. Ge, T. Weerasooriya, Dynamic and Quasi-Static Compressive Response of Porcine Muscle, Journal of biomechanics. 40 (2007), 2999-3005.

[22] X. Nie, J.-I. Cheng, W.W. Chen, T. Weerasooriya, Dynamic Tensile Response of Porcine Muscle, Journal of Applied Mechanics. 78 (2011), 021009.

[23] B. Myers, C. Woolley, T. Slotter, W. Garrett, T. Best, The Influence of Strain Rate on the Passive and Stimulated Engineering Stress–Large Strain Behavior of the Rabbit Tibialis Anterior Muscle, Journal of biomechanical engineering. 120 (1998), 126-132.

[24] M. Takaza, K.M. Moerman, J. Gindre, G. Lyons, C.K. Simms, The Anisotropic Mechanical Behaviour of Passive Skeletal Muscle Tissue Subjected to Large Tensile Strain, Journal of the mechanical behavior of biomedical materials. 17 (2013), 209-220.

[25] B.B. Wheatley, G.M. Odegard, K.R. Kaufman, T.L.H. Donahue, How Does Tissue Preparation Affect Skeletal Muscle Transverse Isotropy?, Journal of biomechanics. 49 (2016), 3056-3060.

[26] D.A. Morrow, T.L.H. Donahue, G.M. Odegard, K.R. Kaufman, Transversely Isotropic Tensile Material Properties of Skeletal Muscle Tissue, Journal of the mechanical behavior of biomedical materials. 3 (2010), 124-129.

[27] G.A. Meyer, R.L. Lieber, Elucidation of Extracellular Matrix Mechanics from Muscle Fibers and Fiber Bundles, Journal of biomechanics. 44 (2011), 771-773.

[28] A.R. Gillies, L.R. Smith, R.L. Lieber, S. Varghese, Method for Decellularizing Skeletal Muscle without Detergents or Proteolytic Enzymes, Tissue engineering part C: Methods. 17 (2010), 383-389.

[29] T.L. Norman, S.V. Nivargikar, D.B. Burr, Resistance to Crack Growth in Human Cortical Bone Is Greater in Shear Than in Tension, Journal of Biomechanics. 29 (1996), 1023-1031.

[30] J.C. Behiri, W. Bonfield, Fracture Mechanics of Bone—the Effects of Density, Specimen Thickness and Crack Velocity on Longitudinal Fracture, Journal of Biomechanics. 17 (1984), 25-34.

[31] R. Crowninshield, M. Pope, The Response of Compact Bone in Tension at Various Strain Rates, Annals of Biomedical Engineering. 2 (1974), 217-225.

[32] T. Wright, W. Hayes, Tensile Testing of Bone over a Wide Range of Strain Rates: Effects of Strain Rate, Microstructure and Density, Medical and biological engineering. 14 (1976), 671.

[33] P. Zioupos, U. Hansen, J.D. Currey, Microcracking Damage and the Fracture Process in Relation to Strain Rate in Human Cortical Bone Tensile Failure, Journal of Biomechanics. 41 (2008), 2932-2939.

[34] W. Bonfield, P. Datta, Fracture Toughness of Compact Bone, Journal of Biomechanics. 9 (1976), 131-134.

[35] D. Moyle, A. Gavens, Fracture Properties of Bovine Tibial Bone, Journal of biomechanics. 19 (1986), 919-927.

[36] T.L. Norman, D. Vashishth, D. Burr, Fracture Toughness of Human Bone under Tension, Journal of biomechanics. 28 (1995), 309-320.

[37] Y.N. Yeni, C.U. Brown, Z. Wang, T.L. Norman, The Influence of Bone Morphology on Fracture Toughness of the Human Femur and Tibia, Bone. 21 (1997), 453-459.

[38] G.C. Reilly, J.D. Currey, The Effects of Damage and Microcracking on the Impact Strength of Bone, Journal of biomechanics. 33 (2000), 337-343.

[39] D. Vashishth, K. Tanner, W. Bonfield, Contribution, Development and Morphology of Microcracking in Cortical Bone During Crack Propagation, Journal of biomechanics. 33 (2000), 1169-1174.

[40] P. Zioupos, J. Currey, Changes in the Stiffness, Strength, and Toughness of Human Cortical Bone with Age, Bone. 22 (1998), 57-66.

[41] E.A. Zimmermann, E. Schaible, H. Bale, H.D. Barth, S.Y. Tang, P. Reichert, B. Busse, T. Alliston, J.W. Ager, R.O. Ritchie, Age-Related Changes in the Plasticity and Toughness of Human Cortical Bone at Multiple Length Scales, Proceedings of the National Academy of Sciences. 108 (2011), 14416-14421.

[42] H. Peterlik, P. Roschger, K. Klaushofer, P. Fratzl, From Brittle to Ductile Fracture of Bone, Nature materials. 5 (2006), 52.

[43] X. Wang, R.A. Bank, J.M. TeKoppele, C.M. Agrawal, The Role of Collagen in Determining Bone Mechanical Properties, Journal of orthopaedic research. 19 (2001), 1021-1026.

[44] J. Phelps, G. Hubbard, X. Wang, C. Agrawal, Microstructural Heterogeneity and the Fracture Toughness of Bone, Journal of biomedical materials research. 51 (2000), 735-741.

[45] Y.N. Yeni, T.L. Norman, Calculation of Porosity and Osteonal Cement Line Effects on the Effective Fracture Toughness of Cortical Bone in Longitudinal Crack Growth, Journal of Biomedical Materials Research: An Official Journal of The Society for Biomaterials, The Japanese Society for Biomaterials, and The Australian Society for Biomaterials and the Korean Society for Biomaterials. 51 (2000), 504-509.

[46] A. Odgaard, F. Linde, The Underestimation of Young's Modulus in Compressive Testing of Cancellous Bone Specimens, Journal of biomechanics. 24 (1991), 691-698.

[47] L. Røhl, E. Larsen, F. Linde, A. Odgaard, J. Jørgensen, Tensile and Compressive Properties of Cancellous Bone, Journal of biomechanics. 24 (1991), 1143-1149.

[48] D.R. Carter, W.C. Hayes, The Compressive Behavior of Bone as a Two-Phase Porous Structure, The Journal of bone and joint surgery. American volume. 59 (1977), 954-962.

[49] A. Ural, P. Zioupos, D. Buchanan, D. Vashishth, The Effect of Strain Rate on Fracture Toughness of Human Cortical Bone: A Finite Element Study, Journal of the mechanical behavior of biomedical materials. 4 (2011), 1021-1032.

[50] S. Charoenphan, A. Polchai, Finite Element Modeling for Strain Rate Dependency of Fracture Resistance in Compact Bone, Journal of biomechanical engineering. 129 (2007), 20-25.

[51] R.R. Adharapurapu, F. Jiang, K.S. Vecchio, Dynamic Fracture of Bovine Bone, Materials Science and Engineering: C. 26 (2006), 1325-1332.

[52] G.P. EVANS, J.C. BEHIRI, L.C. VAUGHAN, W. BONFIELD, The Response of Equine Cortical Bone to Loading at Strain Rates Experienced in Vivo by the Galloping Horse, Equine Veterinary Journal. 24 (1992), 125-128.

[53] A. Pilcher, X. Wang, Z. Kaltz, J. Garrison, G. Niebur, J. Mason, B. Song, M. Cheng, W. Chen, High Strain Rate Testing of Bovine Trabecular Bone, Journal of biomechanical engineering. 132 (2010), 081012.

[54] F. Linde, P. Nørgaard, I. Hvid, A. Odgaard, K. Søballe, Mechanical Properties of Trabecular Bone. Dependency on Strain Rate, Journal of Biomechanics. 24 (1991), 803-809.

[55] R. Guedes, J. Simoes, J. Morais, Viscoelastic Behaviour and Failure of Bovine Cancellous Bone under Constant Strain Rate, Journal of biomechanics. 39 (2006), 49-60.

[56] M. Prot, T.J. Cloete, D. Saletti, S. Laporte, The Behavior of Cancellous Bone from Quasi-Static to Dynamic Strain Rates with Emphasis on the Intermediate Regime, Journal of Biomechanics. 49 (2016), 1050-1057.

[57] V.P.W. Shim, L.M. Yang, J.F. Liu, V.S. Lee, Characterisation of the Dynamic Compressive Mechanical Properties of Cancellous Bone from the Human Cervical Spine, International Journal of Impact Engineering. 32 (2005), 525-540.

[58] R.M. Kulin, F. Jiang, K.S. Vecchio, Loading Rate Effects on the R-Curve Behavior of Cortical Bone, Acta Biomaterialia. 7 (2011), 724-732.

[59] H. Kirchner, Ductility and Brittleness of Bone, International journal of fracture. 139 (2006), 509-516.

[60] H.D. Barth, M.E. Launey, A.A. MacDowell, J.W. Ager III, R.O. Ritchie, On the Effect of X-Ray Irradiation on the Deformation and Fracture Behavior of Human Cortical Bone, Bone. 46 (2010), 1475-1485.

[61] O. Akkus, R.M. Belaney, Sterilization by Gamma Radiation Impairs the Tensile Fatigue Life of Cortical Bone by Two Orders of Magnitude, Journal of Orthopaedic Research. 23 (2005), 1054-1058.

[62] O. Akkus, C.M. Rimnac, Fracture Resistance of Gamma Radiation Sterilized Cortical Bone Allografts, Journal of Orthopaedic Research. 19 (2001), 927-934.

[63] Y. Zhang, D. Homsi, K. Gates, K. Oakes, V. Sutherland, J.L. Wolfinbarger, A Comprehensive Study of Physical Parameters, Biomechanical Properties, and Statistical Correlations of Iliac Crest Bone Wedges Used in Spinal Fusion Surgery. Iv. Effect of Gamma Irradiation on Mechanical and Material Properties, Spine. 19 (1994), 304-308.

[64] J. Cormier, S. Manoogian, J. Bisplinghoff, S. Rowson, A.C. Santago, C. McNally, S. Duma, J.H. Bolte, Biomechanical Response of the Human Face and Corresponding Biofidelity of the Focus Headform, SAE International Journal of Passenger Cars-Mechanical Systems. 3 (2010), 842-859.

[65] J. Cormier, S. Manoogian, J. Bisplinghoff, S. Rowson, A. Santago, C. McNally, S. Duma, J. Bolte Iv, The Tolerance of the Nasal Bone to Blunt Impact, Annals of advances in automotive medicine/Annual Scientific Conference, Association for the Advancement of Automotive Medicine, 2010, p. 3.

[66] J. Cormier, S. Manoogian, J. Bisplinghoff, S. Rowson, A. Santago, C. McNally, S. Duma, J. Bolte, The Tolerance of the Maxilla to Blunt Impact, Journal of biomechanical engineering. 133 (2011), 064501.

[67] M. Unnewehr, C. Homann, P. Schmidt, P. Sotony, G. Fischer, B. Brinkmann, T. Bajanowski, A. DuChesne, Fracture Properties of the Human Mandible, International journal of legal medicine. 117 (2003), 326-330.

[68] R.H. Hopper Jr, J.H. McElhaney, B.S. Myers, Mandibular and Basilar Skull Fracture Tolerance, SAE transactions. (1994), 1688-1696.

[69] J.H. McElhaney, J.L. Fogle, J.W. Melvin, R.R. Haynes, V.L. Roberts, N.M. Alem, Mechanical Properties of Cranial Bone, Journal of biomechanics. 3 (1970), 495-511.

[70] D. Robbins, J. Wood, Determination of Mechanical Properties of the Bones of the Skull, Experimental Mechanics. 9 (1969), 236-240.

[71] F.G. Evans, H.R. Lissner, Tensile and Compressive Strength of Human Parietal Bone, Journal of Applied Physiology. 10 (1957), 493-497.

[72] S. Boruah, K. Henderson, D. Subit, R.S. Salzar, B.S. Shender, G. Paskoff, Response of Human Skull Bone to Dynamic Compressive Loading, Proceedings of the IRCOBI Conference, 2013, p. 497.

[73] G.E. Fantner, T. Hassenkam, J.H. Kindt, J.C. Weaver, H. Birkedal, L. Pechenik, J.A. Cutroni, G.A.G. Cidade, G.D. Stucky, D.E. Morse, P.K. Hansma, Sacrificial Bonds and Hidden Length Dissipate Energy as Mineralized Fibrils separate During Bone Fracture, Nature Materials. 4 (2005), 612-616.

[74] E.A. Zimmermann, B. Gludovatz, E. Schaible, B. Busse, R.O. Ritchie, Fracture Resistance of Human Cortical Bone across Multiple Length-Scales at Physiological Strain Rates, Biomaterials. 35 (2014), 5472-5481.

[75] E.A. Zimmermann, H.D. Barth, R.O. Ritchie, The Multiscale Origins of Fracture Resistance in Human Bone and Its Biological Degradation, Jom. 64 (2012), 486-493.

[76] R.K. Nalla, J.H. Kinney, R.O. Ritchie, Mechanistic Fracture Criteria for the Failure of Human Cortical Bone, Nature materials. 2 (2003), 164.

[77] R.K. Nalla, J.J. Kruzic, J.H. Kinney, R.O. Ritchie, Mechanistic Aspects of Fracture and R-Curve Behavior in Human Cortical Bone, Biomaterials. 26 (2005), 217-231.

[78] P. Braidotti, E. Bemporad, T. D'Alessio, S.A. Sciuto, L. Stagni, Tensile Experiments and Sem Fractography on Bovine Subchondral Bone, Journal of Biomechanics. 33 (2000), 1153-1157.

[79] G.P. Parsamian, T.L. Norman, Diffuse Damage Accumulation in the Fracture Process Zone of Human Cortical Bone Specimens and Its Influence on Fracture Toughness, Journal of Materials Science: Materials in Medicine. 12 (2001), 779-783.

[80] X. Wang, X. Shen, X. Li, C. Mauli Agrawal, Age-Related Changes in the Collagen Network and Toughness of Bone, Bone. 31 (2002), 1-7.

[81] F.J. O'Brien, D. Taylor, T.C. Lee, Microcrack Accumulation at Different Intervals During Fatigue Testing of Compact Bone, Journal of biomechanics. 36 (2003), 973-980.

[82] D. Vashishth, K. Tanner, W. Bonfield, Experimental Validation of a Microcracking-Based Toughening Mechanism for Cortical Bone, Journal of Biomechanics. 36 (2003), 121-124.

[83] K.J. Koester, J.W. Ager Iii, R.O. Ritchie, The True Toughness of Human Cortical Bone Measured with Realistically Short Cracks, Nature Materials. 7 (2008), 672.

[84] D.P. Fyhrie, M.B. Schaffler, Failure Mechanisms in Human Vertebral Cancellous Bone, Bone. 15 (1994), 105-109.

[85] B. Song, C. Syn, C. Grupido, W. Chen, W.-Y. Lu, A Long Split Hopkinson Pressure Bar (Lshpb) for Intermediate-Rate Characterization of Soft Materials, Experimental mechanics. 48 (2008), 809.

[86] W.W. Chen, Experimental Methods for Characterizing Dynamic Response of Soft Materials, Journal of Dynamic Behavior of Materials. 2 (2016), 2-14.

[87] M.H. Farid, A. Eslaminejad, M. Ramzanpour, M. Ziejewski, G. Karami, The Strain Rates of the Brain and Skull under Dynamic Loading, ASME 2018 International Mechanical Engineering Congress and Exposition, American Society of Mechanical Engineers, 2018, pp. V003T004A067-V003T004A067.

[88] D. Hynd, C. Willis, A. ROBERTS, R. Lowne, R. Hopcroft, P. Manning, W. Wallace, The Development of an Injury Criteria for Axial Loading to the Thor-Lx Based on Pmhs Testing, (2003).

[89] R.M. Kulin, F. Jiang, K.S. Vecchio, Effects of Age and Loading Rate on Equine Cortical Bone Failure, Journal of the Mechanical Behavior of Biomedical Materials. 4 (2011), 57-75.

[90] J.L. Wood, Dynamic Response of Human Cranial Bone, Journal of biomechanics. 4 (1971), 1-12.

[91] B. Coats, S.S. Margulies, Material Properties of Human Infant Skull and Suture at High Rates, Journal of neurotrauma. 23 (2006), 1222-1232.

[92] J.-L. Gennisson, T. Deffieux, E. Macé, G. Montaldo, M. Fink, M. Tanter, Viscoelastic and Anisotropic Mechanical Properties of in Vivo Muscle Tissue Assessed by Supersonic Shear Imaging, Ultrasound in medicine & biology. 36 (2010), 789-801.

[93] T.K. Borg, J.B. Caulfield, Morphology of Connective Tissue in Skeletal Muscle, Tissue and Cell. 12 (1980), 197-207.

[94] R. Schleip, I.L. Naylor, D. Ursu, W. Melzer, A. Zorn, H.-J. Wilke, F. Lehmann-Horn, W. Klingler, Passive Muscle Stiffness May Be Influenced by Active Contractility of Intramuscular Connective Tissue, Medical hypotheses. 66 (2006), 66-71.

[95] C. Van Sligtenhorst, D.S. Cronin, G.W. Brodland, High Strain Rate Compressive Properties of Bovine Muscle Tissue Determined Using a Split Hopkinson Bar Apparatus, Journal of biomechanics. 39 (2006), 1852-1858.

[96] S.S. Sarva, S. Deschanel, M.C. Boyce, W. Chen, Stress–Strain Behavior of a Polyurea and a Polyurethane from Low to High Strain Rates, Polymer. 48 (2007), 2208-2213.

[97] S. Deschanel, B. Greviskes, K. Bertoldi, S. Sarva, W. Chen, S. Samuels, R. Cohen, M. Boyce, Rate Dependent Finite Deformation Stress–Strain Behavior of an Ethylene Methacrylic Acid Copolymer and an Ethylene Methacrylic Acid Butyl Acrylate Copolymer, Polymer. 50 (2009), 227-235.

[98] J. Shim, D. Mohr, Using Split Hopkinson Pressure Bars to Perform Large Strain Compression Tests on Polyurea at Low, Intermediate and High Strain Rates, International Journal of Impact Engineering. 36 (2009), 1116-1127.

[99] M. Ottenio, D. Tran, A.N. Annaidh, M.D. Gilchrist, K. Bruyère, Strain Rate and Anisotropy Effects on the Tensile Failure Characteristics of Human Skin, Journal of the mechanical behavior of biomedical materials. 41 (2015), 241-250.

[100] J.R. Löapez, P.D. Allen, L. Alamo, D. Jones, F.A. Sreter, Myoplasmic Free [Ca2+] During a Malignant Hyperthermia Episode in Swine, Muscle & Nerve: Official Journal of the American Association of Electrodiagnostic Medicine. 11 (1988), 82-88.

[101] W.W. Chen, B. Song, Split Hopkinson (Kolsky) Bar: Design, Testing and Applications, Springer Science & Business Media2010.

[102] J. Gindre, M. Takaza, K.M. Moerman, C.K. Simms, A Structural Model of Passive Skeletal Muscle Shows Two Reinforcement Processes in Resisting Deformation, Journal of the mechanical behavior of biomedical materials. 22 (2013), 84-94.

[103] R.W. Ogden, Large Deformation Isotropic Elasticity–on the Correlation of Theory and Experiment for Incompressible Rubberlike Solids, Proceedings of the Royal Society of London. A. Mathematical and Physical Sciences. 326 (1972), 565-584.

[104] M. Van Loocke, C. Simms, C. Lyons, Viscoelastic Properties of Passive Skeletal Muscle in Compression—Cyclic Behaviour, Journal of Biomechanics. 42 (2009), 1038-1048.

[105] G. Regazzoni, J. Johnson, P. Follansbee, Theoretical Study of the Dynamic Tensile Test, Journal of applied mechanics. 53 (1986), 519-528.

[106] W. Bleck, I. Schael, Determination of Crash-Relevant Material Parameters by Dynamic Tensile Tests, Steel research. 71 (2000), 173-178.

[107] B.L. Boyce, M.F. Dilmore, The Dynamic Tensile Behavior of Tough, Ultrahigh-Strength Steels at Strain-Rates from 0.0002 S− 1 to 200 S− 1, International Journal of Impact Engineering. 36 (2009), 263-271.

[108] X. Zhai, W. Chen, Compressive Mechanical Response of Porcine Muscle at Intermediate (10 0/S-10 2/S) Strain Rates, Experimental Mechanics. (2018), 1-7.

[109] G. Mutungi, P. Purslow, C. Warkup, Structural and Mechanical Changes in Raw and Cooked Single Porcine Muscle Fibres Extended to Fracture, Meat science. 40 (1995), 217-234.

[110] F.E. Zajac, Muscle and Tendon: Properties, Models, Scaling, and Application to Biomechanics and Motor Control, Critical reviews in biomedical engineering. 17 (1989), 359-411.

[111] C.J. Zuurbier, A.J. Everard, P. van der Wees, P.A. Huijing, Length-Force Characteristics of the Aponeurosis in the Passive and Active Muscle Condition and in the Isolated Condition, Journal of biomechanics. 27 (1994), 445-453.

[112] O. Maïsetti, F. Hug, K. Bouillard, A. Nordez, Characterization of Passive Elastic Properties of the Human Medial Gastrocnemius Muscle Belly Using Supersonic Shear Imaging, Journal of biomechanics. 45 (2012), 978-984.

[113] C. Van Ee, A. Chasse, B. Myers, Quantifying Skeletal Muscle Properties in Cadaveric Test Specimens: Effects of Mechanical Loading, Postmortem Time, and Freezer Storage, Journal of biomechanical engineering. 122 (2000), 9-14.

[114] D. Vashishth, K.E. Tanner, W. Bonfield, Contribution, Development and Morphology of Microcracking in Cortical Bone During Crack Propagation, Journal of Biomechanics. 33 (2000), 1169-1174.

[115] L. Shannahan, T. Weerasooriya, A. Gunnarsson, B. Sanborn, L. Lamberson, Rate-Dependent Fracture Modes in Human Femoral Cortical Bone, International Journal of Fracture. 194 (2015), 81-92.

[116] W.S. Enns-Bray, S.J. Ferguson, B. Helgason, Strain Rate Dependency of Bovine Trabecular Bone under Impact Loading at Sideways Fall Velocity, Journal of Biomechanics. 75 (2018), 46-52.

[117] N.D. Parab, Z. Guo, M. Hudspeth, B. Claus, B.H. Lim, T. Sun, X. Xiao, K. Fezzaa, W.W. Chen, In Situ Observation of Fracture Processes in High-Strength Concretes and Limestone Using High-Speed X-Ray Phase-Contrast Imaging, Philosophical Transactions of the Royal Society A: Mathematical, Physical and Engineering Sciences. 375 (2017), 20160178.

[118] H. Kolsky, An Investigation of the Mechanical Properties of Materials at Very High Rates of Loading, Proceedings of the physical society. Section B. 62 (1949), 676.

[119] M. Hudspeth, B. Claus, S. Dubelman, J. Black, A. Mondal, N. Parab, C. Funnell, F. Hai, M. Qi, K. Fezzaa, High Speed Synchrotron X-Ray Phase Contrast Imaging of Dynamic Material Response to Split Hopkinson Bar Loading, Review of Scientific Instruments. 84 (2013), 025102.

[120] W.W. Chen, M.C. Hudspeth, B. Claus, N.D. Parab, J.T. Black, K. Fezzaa, S. Luo, In Situ Damage Assessment Using Synchrotron X-Rays in Materials Loaded by a Hopkinson Bar, Philosophical Transactions of the Royal Society A: Mathematical, Physical and Engineering Sciences. 372 (2014), 20130191.

[121] N.D. Parab, B. Claus, M.C. Hudspeth, J.T. Black, A. Mondal, J. Sun, K. Fezzaa, X. Xiao, S. Luo, W. Chen, Experimental Assessment of Fracture of Individual Sand Particles at Different Loading Rates, International Journal of Impact Engineering. 68 (2014), 8-14.

[122] M. Hudspeth, B. Claus, N. Parab, B. Lim, W. Chen, T. Sun, K. Fezza, In Situ Visual Observation of Fracture Processes in Several High-Performance Fibers, Journal of Dynamic Behavior of Materials. 1 (2015), 55-64.

[123] M.B. Zbib, N.D. Parab, W.W. Chen, D.F. Bahr, New Pulverization Parameter Derived from Indentation and Dynamic Compression of Brittle Microspheres, Powder technology. 283 (2015), 57-65.

[124] A. International, Standard Test Method for Measurement of Fracture Toughness, ASTM International2011.

[125] A. Parish, W. Chen, T. Weerasooriya, High Strain-Rate Tensile Behavior of Pig Bones, DYMAT-International Conference on the Mechanical and Physical Behaviour of Materials under Dynamic Loading, EDP Sciences, 2009, pp. 917-922.

[126] G.C. Sih, Mechanics of Fracture Initiation and Propagation: Surface and Volume Energy Density Applied as Failure Criterion, Springer Science & Business Media2012.

[127] R.O. Ritchie, K.J. Koester, S. Ionova, W. Yao, N.E. Lane, J.W. Ager, Measurement of the Toughness of Bone: A Tutorial with Special Reference to Small Animal Studies, Bone. 43 (2008), 798-812.

[128] D. Vashishth, J.C. Behiri, W. Bonfield, Crack Growth Resistance in Cortical Bone: Concept of Microcrack Toughening, Journal of Biomechanics. 30 (1997), 763-769.

[129] D.M. Robertson, D. Robertson, C.R. Barrett, Fracture Toughness, Critical Crack Length and Plastic Zone Size in Bone, Journal of Biomechanics. 11 (1978), 359-364.

[130] R.B. Cook, P. Zioupos, The Fracture Toughness of Cancellous Bone, Journal of Biomechanics. 42 (2009), 2054-2060.

[131] M.J. Buehler, Molecular Nanomechanics of Nascent Bone: Fibrillar Toughening by Mineralization, Nanotechnology. 18 (2007), 295102.

[132] F.H. Silver, D.L. Christiansen, P.B. Snowhill, Y. Chen, Transition from Viscous to Elastic-Based Dependency of Mechanical Properties of Self-Assembled Type I Collagen Fibers, Journal of applied polymer science. 79 (2001), 134-142.

[133] H.S. Gupta, W. Wagermaier, G.A. Zickler, D. Raz-Ben Aroush, S.S. Funari, P. Roschger, H.D. Wagner, P. Fratzl, Nanoscale Deformation Mechanisms in Bone, Nano letters. 5 (2005), 2108-2111.

[134] H.H. Bayraktar, E.F. Morgan, G.L. Niebur, G.E. Morris, E.K. Wong, T.M. Keaveny, Comparison of the Elastic and Yield Properties of Human Femoral Trabecular and Cortical Bone Tissue, Journal of biomechanics. 37 (2004), 27-35.

[135] H. Ming-Yuan, J.W. Hutchinson, Crack Deflection at an Interface between Dissimilar Elastic Materials, International Journal of Solids and Structures. 25 (1989), 1053-1067.

[136] V. Imbeni, J. Kruzic, G. Marshall, S. Marshall, R. Ritchie, The Dentin–Enamel Junction and the Fracture of Human Teeth, Nature materials. 4 (2005), 229.

[137] K.S. Chan, D.P. Nicolella, Micromechanical Modeling of R-Curve Behaviors in Human Cortical Bone, Journal of the mechanical behavior of biomedical materials. 16 (2012), 136-152.

[138] D.B. Burr, M.B. Schaffler, R.G. Frederickson, Composition of the Cement Line and Its Possible Mechanical Role as a Local Interface in Human Compact Bone, Journal of biomechanics. 21 (1988), 939-945.

[139] X. Guo, L. Liang, S. Goldstein, Micromechanics of Osteonal Cortical Bone Fracture, Journal of Biomechanical Engineering. 120 (1998), 112-117.

[140] M. Brookes, W.J. Revell, Blood Supply of Bone: Scientific Aspects, Springer Science & Business Media2012.

[141] G.K. McPherson, T.J. Kriewall, The Elastic Modulus of Fetal Cranial Bone: A First Step Towards an Understanding of the Biomechanics of Fetal Head Molding, Journal of Biomechanics. 13 (1980), 9-16.

[142] J.A. Motherway, P. Verschueren, G. Van der Perre, J. Vander Sloten, M.D. Gilchrist, The Mechanical Properties of Cranial Bone: The Effect of Loading Rate and Cranial Sampling Position, Journal of biomechanics. 42 (2009), 2129-2135.

[143] R.P. Hubbard, Flexure of Layered Cranial Bone, Journal of Biomechanics. 4 (1971), 251-263.

[144] R. Delille, D. Lesueur, P. Potier, P. Drazetic, E. Markiewicz, Experimental Study of the Bone Behaviour of the Human Skull Bone for the Development of a Physical Head Model, International Journal of Crashworthiness. 12 (2007), 101-108.

[145] A. Auperrin, R. Delille, D. Lesueur, K. Bruyère, C. Masson, P. Drazétic, Geometrical and Material Parameters to Assess the Macroscopic Mechanical Behaviour of Fresh Cranial Bone Samples, Journal of biomechanics. 47 (2014), 1180-1185.

[146] J. Rahmoun, A. Auperrin, R. Delille, H. Naceur, P. Drazetic, Characterization and Micromechanical Modeling of the Human Cranial Bone Elastic Properties, Mechanics Research Communications. 60 (2014), 7-14.

[147] M.T. Davis, A.M. Loyd, H.-y.H. Shen, M.H. Mulroy, R.W. Nightingale, B.S. Myers, C.D. Bass, The Mechanical and Morphological Properties of 6 Year-Old Cranial Bone, Journal of biomechanics. 45 (2012), 2493-2498.

[148] J. Peterson, P.C. Dechow, Material Properties of the Inner and Outer Cortical Tables of the Human Parietal Bone, The Anatomical Record: An Official Publication of the American Association of Anatomists. 268 (2002), 7-15.

[149] J. Peterson, P.C. Dechow, Material Properties of the Human Cranial Vault and Zygoma, The Anatomical Record Part A: Discoveries in Molecular, Cellular, and Evolutionary Biology: An Official Publication of the American Association of Anatomists. 274 (2003), 785-797.

[150] S. Boruah, D.L. Subit, G.R. Paskoff, B.S. Shender, J.R. Crandall, R.S. Salzar, Influence of Bone Microstructure on the Mechanical Properties of Skull Cortical Bone–a Combined Experimental and Computational Approach, Journal of the mechanical behavior of biomedical materials. 65 (2017), 688-704.

[151] J.C. Lotz, T.N. Gerhart, W.C. Hayes, Mechanical Properties of Trabecular Bone from the Proximal Femur: A Quantitative Ct Study, Journal of computer assisted tomography. 14 (1990), 107-114.

[152] S.M. Snyder, E. Schneider, Estimation of Mechanical Properties of Cortical Bone by Computed Tomography, Journal of Orthopaedic Research. 9 (1991), 422-431.

[153] T.S. Keller, Predicting the Compressive Mechanical Behavior of Bone, Journal of biomechanics. 27 (1994), 1159-1168.

[154] T.S. Kaneko, J.S. Bell, M.R. Pejcic, J. Tehranzadeh, J.H. Keyak, Mechanical Properties, Density and Quantitative Ct Scan Data of Trabecular Bone with and without Metastases, Journal of biomechanics. 37 (2004), 523-530.

[155] N. Lynnerup, J.G. Astrup, B. Sejrsen, Thickness of the Human Cranial Diploe in Relation to Age, Sex and General Body Build, Head & face medicine. 1 (2005), 13.

[156] V. Sabanciogullari, I. Salk, M. Cimen, V. Sabanciogullari, I. Salk, M. Cimen, The Relationship between Total Calvarial Thickness and Diploe in the Elderly, Int J Morphol. 31 (2013), 38-44.

[157] S.L. Alexander, K. Rafaels, C.A. Gunnarsson, T. Weerasooriya, Structural Analysis of the Frontal and Parietal Bones of the Human Skull, Journal of the mechanical behavior of biomedical materials. 90 (2019), 689-701.

[158] C.A. Schneider, W.S. Rasband, K.W. Eliceiri, Nih Image to Imagej: 25 Years of Image Analysis, Nature methods. 9 (2012), 671.

[159] X. Nie, W.W. Chen, X. Sun, D.W. Templeton, Dynamic Failure of Borosilicate Glass under Compression/Shear Loading Experiments, Journal of the American Ceramic Society. 90 (2007), 2556-2562.

[160] V.C. Mow, R. Huiskes, Basic Orthopaedic Biomechanics & Mechano-Biology, Lippincott Williams & Wilkins2005.

[161] L. Mosekilde, L. Mosekilde, C. Danielsen, Biomechanical Competence of Vertebral Trabecular Bone in Relation to Ash Density and Age in Normal Individuals, Bone. 8 (1987), 79-85.

[162] R.W. Goulet, S.A. Goldstein, M.J. Ciarelli, J.L. Kuhn, M. Brown, L. Feldkamp, The Relationship between the Structural and Orthogonal Compressive Properties of Trabecular Bone, Journal of biomechanics. 27 (1994), 375-389.

[163] R.O. Ritchie, M.J. Buehler, P. Hansma, Plasticity and Toughness in Bone, Phys. Today. 62 (2009), 41-47.

[164] J.B. Thompson, J.H. Kindt, B. Drake, H.G. Hansma, D.E. Morse, P.K. Hansma, Bone Indentation Recovery Time Correlates with Bond Reforming Time, Nature. 414 (2001), 773.

[165] M.E. Launey, M.J. Buehler, R.O. Ritchie, On the Mechanistic Origins of Toughness in Bone, Annual review of materials research. 40 (2010), 25-53.

[166] P. Zioupos, J. Currey, The Extent of Microcracking and the Morphology of Microcracks in Damaged Bone, Journal of Materials Science. 29 (1994), 978-986.

[167] M.E. Launey, P.-Y. Chen, J. McKittrick, R. Ritchie, Mechanistic Aspects of the Fracture Toughness of Elk Antler Bone, Acta biomaterialia. 6 (2010), 1505-1514.

[168] R.K. Nalla, J.J. Kruzic, R.O. Ritchie, On the Origin of the Toughness of Mineralized Tissue: Microcracking or Crack Bridging?, Bone. 34 (2004), 790-798.

[169] H. Peterlik, Crack Bridging Stresses in Alumina During Crack Extension, Journal of materials science letters. 20 (2001), 1703-1705.

[170] R.K. Nalla, J.J. Kruzic, J.H. Kinney, R.O. Ritchie, Effect of Aging on the Toughness of Human Cortical Bone: Evaluation by R-Curves, Bone. 35 (2004), 1240-1246.

[171] D. Liu, S. Weiner, H.D. Wagner, Anisotropic Mechanical Properties of Lamellar Bone Using Miniature Cantilever Bending Specimens, Journal of Biomechanics. 32 (1999), 647-654.

[172] E.A. Zimmermann, R.O. Ritchie, Bone as a Structural Material, Advanced healthcare materials. 4 (2015), 1287-1304.

[173] X. Zhai, Z. Guo, J. Gao, N. Kedir, Y. Nie, B. Claus, T. Sun, X. Xiao, K. Fezzaa, W.W. Chen, High-Speed X-Ray Visualization of Dynamic Crack Initiation and Propagation in Bone, Acta biomaterialia. 90 (2019), 278-286.

[174] X. Zhai, J. Gao, Y. Nie, Z. Guo, N. Kedir, B. Claus, T. Sun, K. Fezzaa, X. Xiao, W.W. Chen, Real-Time Visualization of Dynamic Fractures in Porcine Bones and the Loading-Rate Effect on Their Fracture Toughness, Journal of the Mechanics and Physics of Solids. 131 (2019), 358-371.

[175] E.A. Zimmermann, M.E. Launey, H.D. Barth, R.O. Ritchie, Mixed-Mode Fracture of Human Cortical Bone, Biomaterials. 30 (2009), 5877-5884.

PUBLICATIONS

1. **X. Zhai**, W.W. Chen, Compressive mechanical response of porcine muscle at intermediate (10^0/s─10^2/s) Strain rates, Experimental Mechanics. Doi: 10.1007/s11340-018-00456-1 (2018)
2. **X. Zhai**, E.A. Nauman, Y. Nie, H. Liao, R.J. Lycke, W.W. Chen, Mechanical response of human muscle at intermediate strain rates, Journal of Biomechanical Engineering. 141 (4) (2019), 044506.
3. **X. Zhai**, J. Gao, H. Liao, C.D. Kirk, Y.A. Balogun, W.W. Chen, Mechanical behaviors of auxetic Polyurethane foam at quasi-static, intermediate and high strain rates, International Journal of Impact Engineering. 129 (2019), 112-118
4. **X. Zhai**, Z. Guo, J. Gao, N. Kedir, Y. Nie, B. Claus, T. Sun, X. Xiao, K. Fezzaa, W.W. Chen, High-speed X-ray visualization of dynamic crack initiation and propagation in bone, Acta Biomaterialia. 90 (2019), 278-286.
5. **X. Zhai**, J. Gao, Y. Nie, Z. Guo. N. Kedir, B. Claus, T. Sun, K. Fezzaa, X. Xiao, W.W. Chen, Real-time visualization of dynamic fractures in porcine bones and the loading-rate effect on their fracture toughness, Journal of the Mechanics and Physics of Solids. 131 (2019), 358-371.
6. **X. Zhai**, E.A. Nauman, D. Moryl, R.J. Lycke, W.W. Chen, The effects of loading-direction and strain-rate on the mechanical behaviors of human frontal skull bone, in submission (Journal of the Mechanical Behaviors of Biomedical Materials, 2019, under review).
7. **X. Zhai**, Y. Nie, J. Gao, N. Kedir, B. Claus, T. Sun, K. Fezzaa, W.W. Chen, The effect of loading direction on the fracture behaviors of cortical bone at a dynamic loading rate, in submission (Journal of the Mechanics and Physics of Solids, 2019, under review).
8. Y. Nie, B. Claus, J. Gao, **X. Zhai**, N. Kedir, J. Chu, T. Sun, K. Fezzaa, W.W. Chen, In situ observation of adiabatic shear band formation in aluminum alloys. Experimental Mechanics (2019), accepted, in production.
9. J. Gao, Y. Nie, B.H. Lim, **X. Zhai**, N. Kedir, In-situ observation of cutting-induced failure processes of single high-performance fibers inside an SEM, in submission (Composites Part A, 2019, under review).

10. **X. Zhai**, N. Kedir, Y. Nie, J. Gao, Z. Guo, B. Claus, T. Sun, K. Fezzaa, W.W. Chen, The effects of loading rate and loading directions on the fracture behaviors of bones, in preparation (Extreme Mechanics Letters, 2020).
11. **X. Zhai**, E.A. Nauman, Y. Nie, R.J. Lycke, W.W. Chen, Mechanical behaviors of human skin over a wide range of strain rate: quasi-static, intermediate and high strain rate, in preparation (Journal of Mechanical Behaviors of Biomedical Materials, 2020).
12. **X. Zhai**, H. Liao, W.W. Chen, How loading-rate and material properties affect the mechanical behaviors of Polyurethane foam, in preparation (Polymer, 2020).
13. **X. Zhai**, E.A. Nauman, Y. Nie, R.J. Lycke, W.W. Chen, Mechanical response of human muscle from a young adult, in preparation (Journal of Biomechanics, 2020).
14. **X. Zhai**, E.A. Nauman, Y. Nie, R.J. Lycke, W.W. Chen, Effect of loading rate on the mechanical behaviors of human tendon, ligament and heel pad, in preparation (Journal of Mechanical Behaviors of Biomedical Materials, 2021)
15. **X. Zhai**, W.W. Chen, The mechanical behaviors of porcine skull bones at quasi-static, intermediate and high strain rates, in preparation (Journal of Mechanical Behaviors of Biomedical Materials, 2021).